# Pattern formation in Complex Dynamical Networks

A thesis

submitted by

# Chandrakala Meena

in partial fulfillment of

the requirements for the degree of

**Doctor of Philosophy**



**Indian Institute of Science Education and Research (IISER) Mohali**

**April, 2018**

# Certificate of Examination

This is to certify that the dissertation titled *Pattern formation in Complex Dynamical Networks* submitted by **Ms. Chandrakala Meena** (Reg. No. PH14032) for the partial fulfillment of Doctor of Philosophy programme of the Institute, has been examined by the thesis committee duly appointed by the Institute. The committee finds the work done by the candidate satisfactory and recommends that the report be accepted.

Dr. Rajeev Kapri        Dr. Sanjeev Kumar        Professor Sudeshna Sinha

(Supervisor)

# Declaration

The work presented in this dissertation has been carried out by me under the guidance of Prof. Sudeshna Sinha at the Indian Institute of Science Education and Research Mohali.

This work has not been submitted in part or in full for a degree, a diploma, or a fellowship to any other university or institute. Whenever contributions of others are involved, every effort is made to indicate this clearly, with due acknowledgment of collaborative research and discussions. This thesis is a bona-fide record of original work done by me and all sources listed within have been detailed in the bibliography.

Chandrakala Meena

(Candidate)

In my capacity as the supervisor of the candidate's doctoral thesis, I certify that the above statements by the candidate are true to the best of my knowledge.

Professor Sudeshna Sinha

(Supervisor)

## *Acknowledgements*

*It is a great pleasure to convey my deep gratitude to my thesis supervisor, Prof. Sudeshna Sinha, for her guidance during my PhD research at IISER Mohali. She has been my guiding light for all academic and non-academic discussions, up and downs during my stay at IISER Mohali. Her patience, warm encouragement, flexibility and careful guidance along with genuine caring and concern has been motivating and enlightening. She has been always emphasized on the development of an intuitive understanding of a problem and even very supportive of crazy ideas. Her constant energy and enthusiasm in life has motivated me and will continue to do so for the rest of my life. For this, I will be forever grateful for her.*

*I am thankful to my doctoral committee members, Dr. Rajeev Kapri and Dr. Sanjeev Kumar for their encouragement and insightful comments during my work. My sincere thanks to Prof. Elena Surovyatkina and Prof. Jürgen Kurths for offering me the opportunity to work with their group at PIK, Potsdam which provided me the chance to interact with various people working on a diverse set of problems. I would like to thank Dr. Chiranjit Mitra and Dr. Bedartha for valuable discussions and for making my stay comfortable at Potsdam Institute for Climate Impact Research (PIK). I am grateful to Dr. Harvinder K. Jassal, Prof. Jasjeet Bagla, Dr. Abhishek Chaudhuri, Dr. Ramandeep S. Johal, Prof. Arvind, Dr. Goutam Sheet, Dr. Dipanjan Chakraborty, Dr. Amit Kulshrestha, Prof. Kapil H. Paranjape, Prof. N. Sathyamurthy, Dr. Samrat Ghosh, Dr. Lolitika Mandal, Dr. Sudip Madal, Dr. Paramdeep for their encouragement and support. I convey my gratitude to Dr. Manish D. Shirmali and Dr. K. Murali for many scientific discussions, inputs, and encouragement.*

*I am thankful to IISER Mohali for providing high-performance computing facility, library and other resources useful for research. I thank Department of Science and Technology (DST), INDIA for Innovation in Science Pursuit for Inspired Research (INSPIRE) fellowship, Science & Engineering Research Board (SERB), INDIA for the international travel grant to attend an international conference Perspectives in Nonlinear Dynamics (PNLD) 2016, held in Germany and Potsdam Institute for Climate Impact Research (PIK) for financial support during my stay at PIK, Germany.*

*During a PhD programme, a good support system is essential for surviving and staying lucid. Over the years it has been my good fortune to encounter many people who have given me more of their time, companionship and personal help. I am very much thankful to Karishma and Hema for their valuable time, understanding, support, motivation and*

# Preface

The work presented in this thesis falls in the domain of interdisciplinary science, spanning Nonlinear Dynamics and Complex Networks. Complex systems generically involve two basic components. The first is complex dynamics at a local level, modeled by nonlinear differential equations or nonlinear iterated maps. Such systems are capable of yielding a rich variety of temporal patterns, and exhibit many counter-intuitive phenomena, such as chaos. The second aspect involves the transmission of information among these local dynamical elements. Such interactions are often modelled by interesting coupling topologies and coupling forms, and influences spatiotemporal pattern formation at the global level. So, on the one hand, chaotic phenomena of individual nonlinear systems continue to challenge our everyday intuition, for instance El Niño phenomena, chaotic electronic circuits, metapopulation growth and activity of neurons. On the other hand, complex networks consisting of interacting nonlinear dynamical systems provide us with a framework to model many interactive physical, environmental, social, biological, chemical and engineered systems. For instance, the correlations between climate change in different regions, traffic congestion in large urban centers, cascading failures in power grids, population dynamics in coupled ecosystems. These natural and artificial systems, allow us to get deeper insights into wide ranging complex phenomena arising from the interplay of local dynamics and coupling connections.

My thesis is centered around the exploration and characterization of emergent behaviour, especially synchronization and chimera states, in mathematical models of complex systems and networks. My research work also focuses on the mechanisms that can effectively control complex networks of chaotic systems to steady states and robustness of the steady states. For instance, Random Scale-Free Networks of chaotic populations are successfully controlled to steady states by threshold activated migrations. My thesis work includes mathematical modeling, numerical analysis, network theory, theory of chaos and complex networks for quantifying the rich dynamics exhibit by the complex systems.

In the first research problem, we study the dynamics of two coupled nonlinear delay differential system modeling the El Niño Southern Oscillation (ENSO) phenomenon. We investigate the range of temporal patterns emerging from this system under variation of the time delay in the oceanic waves, the self-delay interaction strength of oceanic waves, and the coupling strength between the two regions. We explore the collective behaviour of the coupled systems in the space of these three parameters for homogeneous and heteroge-

neous cases. Different parameters yield a rich variety of dynamical patterns in our model, ranging from steady states and homogeneous oscillations to irregular oscillations and co-existence of oscillatory attractors, without explicit inclusion of noise. The emergence or suppression of oscillations in our models is a dynamical feature of utmost relevance, as it signals the presence or absence of ENSO-like oscillations. Our central result for both cases suggests larger delay and self-delay coupling strengths lead to oscillations, while strong inter-region coupling kills oscillations.

Further, we study the existence, and basins of attraction of the solutions arising in the model system, for different representative parameter sets. We explicitly obtain the basins of attraction for the different steady states and oscillatory states in the model and these can help in understanding patterns in the sea surface temperatures anomalies in monitored coupled sub-regions. Our principal result suggests that instead of the single value criterion (e.g. 0.5°C, suggested by several agencies such as the National Oceanic and Atmospheric Administration), an interval should be used as a criterion to determine if the El-Niño or La-Niña is in progress. Our results might be helpful for forecasting of El Niño (or La Niña) progress, as it indicates the combination of initial SST anomalies in the sub-regions that can result in a El Niño/La Niña episodes. We also explore the robustness of the different dynamical states under noisy evolution, in order to gauge which set of attractors are typically expected to arise when the system evolves under the influence of external perturbations. Often when noise is very weak, the system is attracted to states close to the noise-free case. We found that when noise is stronger, the system switches randomly between the attractors. Using this method of gauging the robustness of the different attractors in our multi-stable system, we find that lower strength of self-delay coupling yields a larger number of robust states, than stronger self-delay coupling. Further, larger noise strengths are required to switch between these states, when the strength of self-delay coupling is low.

In the second research problem, we study Star networks of diffusively, conjugately and mean-field coupled nonlinear oscillators, with all end nodes connected only to the central hub node. We find that the end-nodes which are equivalent in terms of the coupling environment and dynamical equations, yielded chimera states, i.e. the symmetry of the end-nodes is broken and coexisting groups with different synchronization features and attractor geometries emerged. We also verify the robustness of these chimera states in analog circuit experiments. Further, we analyze the global stability of the chimera states through the measure of basin stability. This allow us to obtain the range of coupling strengths where chimera states has high prevalence. Surprisingly, such chimera states

are very wide-spread in this network topology, and large parameter regimes of moderate coupling strengths evolve to chimera states from generic random initial conditions. Thus it is evident that star networks provide a promising class of coupled systems, in natural or human-engineered contexts, where chimeras are prevalent.

In the third research problem, we study Random Scale-Free networks of $N$ sub-systems of population patches or "a population of populations". populations, modeled by a non-linear map (the Ricker map), typically chaotic, connected by transport that is triggered when population density in a patch is in excess of a critical threshold level. The broad scenario of threshold -activated transport is that each population patch has a critical population density it can support, and when the population in the patch, due to its inherent growth dynamics (which may be chaotic) exceeds this threshold, the excess migrates to neighbouring patches. The neighbouring patch on receiving the migrant population may become over-critical too, triggering further migrations. So this form of coupling is pulsatile and inter-patch transport occurs only when there is excessive build-up of population density in a patch, which may initiate a *cascade of transport events*. First, we study the effect of threshold-activated dispersal on the dynamical patterns emerging in the network. Next our question is, can threshold-activated coupling serve to stabilize the intrinsically chaotic populations in the network to regular behaviour, such as steady states or regular cycles? Our main result suggests threshold-activated dispersal leads to stable fixed populations, for a wide range of threshold levels, denoted by $x_c$. For instance, a *large window of threshold values* $(0 \leq x_c < 1)$ yield fixed point steady states in the network and for threshold levels $1 < x_c < 2$ the populations evolve in regular cycles, where low population densities alternate with a high population densities. Further, we find that suppression of chaos is facilitated when the threshold-activated migration is more rapid than the intrinsic population dynamics of a patch and networks with large number of nodes open to the environment, readily yield stable steady states.

Further, we explore the case of networks with very few (typically 1 or 2) open nodes, and study the effect of the degree and betweenness centrality of these open nodes on the control to steady states. We observed that the degree of the open node does not have significant influence on chaos suppression. However, betweenness centrality of the open node is important, with the region of control being large when the open node has the high betweenness centrality, and vice versa. Moreover, to estimate the efficiency and robustness of the suppression of chaos in the network, we study a couple of qualitative and quantitative measures, for instance, average redistribution time $\langle T \rangle$ and average range of threshold values yielding steady states $\langle R \rangle$. We find that $\langle T \rangle$ and $\langle R \rangle$ depend on the

network size and fraction of open nodes. If very few nodes are open to the environment, then these quantities depend most sensitively on the betweenness centrality of the open node, and to a lesser extent its degree and closeness centrality.

Lastly, we investigate the collective dynamics of multi-stable chaotic systems connected in different network topologies, ranging from rings to scale-free networks and stars. We estimate the dynamical robustness of such networks by introducing a variant of the concept of multi-node basin stability, which allows us to gauge the global stability of the dynamics of the network in response to local perturbations affecting a certain class of nodes of a system. We show that perturbing nodes with high closeness and betweeness centrality significantly reduces the capacity of the system to return to the desired state. This effect is very pronounced for a star network which has one hub node with significantly different closeness/betweeness centrality than all the peripheral nodes. In such a network, perturbation of the single hub node has the capacity to destroy the collective state. On the other hand, even when a majority of the peripheral nodes are strongly perturbed, the hub manages to restore the system to its original state, demonstrating the drastic effect of the centrality of the perturbed node on the dynamics of the network. Further, we explore Random Scale-Free Networks of multi-stable chaotic dynamical elements. These results are important in deciding which nodes to safeguard in order to maintain the collective state of this network against targetted localized attacks.

In summary, in this thesis I have explored pattern formation in networks with different kinds of connection topologies, from the point of view of local and global stability. My results shed light on the effects of the interplay of local chaos and the nature of links. In particular I have demonstrated its crucial influence on spatiotemporal features ranging from stable spatiotemporal fixed points, to chimera states, attractor hopping in multi-stable chaotic systems and spatiotemporal chaos.

# List of Publications

1. Chimera States in Star Network
   **Chandrakala Meena**, K. Murali and Sudeshna Sinha
   *Int. J. Bifurcation Chaos*, 26:1630023, 2016.

2. Threshold-activated transport stabilizes chaotic populations to steady states
   **Chandrakala Meena**, Pranay Deep Rungta, and Sudeshna Sinha
   *PLoS ONE*, 12(8):e0183251, 2017.

3. Are network properties consistent indicators of synchronization?
   Pranay Deep Rungta, Anshul Choudhary, **Chandrakala Meena** and Sudeshna Sinha
   *Europhysics Letters*, 117:20003, 2017.

4. Effect of Heterogeneity in Models of El Niño Southern Oscillations
   **Chandrakala Meena**, Shweta Kumari, Akansha Sharma and Sudeshna Sinha
   *Chaos, Solitons and Fractals*, 104:668-679, 2017.

5. Coexistence of attractors in a coupled nonlinear delayed system modelling El Niño Southern Oscillations
   **Chandrakala Meena**, Elena Surovyatkina and Sudeshna Sinha
   *Proceedings of the Conference on Perspectives in Nonlinear Dynamics - 2016*, Indian Academy of Sciences Conference Series (from *Pramana - Journal of Physics*), **1** (2017) pp. 171-186

6. Identifying nodal properties that are crucial for the dynamical robustness of multi-stable networks
   Pranay Deep Rungta, **Chandrakala Meena** and Sudeshna Sinha
   *arXiv preprint arXiv* : 1801.02409 (2018).

7. Robustness of networks of multi-stable chaotic systems to targetted attacks
   **Chandrakala Meena**, Pranay Deep Rungta and Sudeshna Sinha
   (Manuscript is under preparation).

# Contents

# Chapter 1

# Introduction

Systems that evolve with time are known as dynamical systems. Such dynamical systems are typically modelled by differential equations and difference equations (also known as iterated maps). In continuous time the evolution of the systems is given by differential equations

$$\dot{X} = F(X) \tag{1.1}$$

where $X(t) = \{x_1(t), x_2(t).....x_N(t)\}$ is an $N$-dimensional vector of state variables, $t$ is time and $F(X) = \{f_1(X), f_2(X).....f_N(X)\}$ are the functions that describe the dynamics of the system [1]. The evolution of systems in discrete time is given by difference equations

$$X_{n+1} = F(X_n) \tag{1.2}$$

where $X$ is state vector and $F$ is the function whose iterations determine the flow of the phase point. If $F$ is a nonlinear function, then these coupled differential (or iterated maps) equations allude to *nonlinear dynamical systems*.

Such nonlinear dynamical systems are difficult to solve analytically because they cannot be reduced to well-understood linear systems. Further, they may sensitively depend on initial conditions, which renders the dynamics effectively unpredictable in the long term. Chaos theory and numerical techniques have been helped us to understand the dynamical behaviour of such systems that were earlier considered intractable.

Systems consisting of a large number of interacting nonlinear dynamical systems are known as a complex dynamical systems, for instance, an ecosystem, the human brain, climate, social and economic organization like (cities, banks), power gird. The collective

behaviour of complex systems is difficult to understand due to dependencies and inter-action within components of the systems, as well as between the components and its environment. Such complex systems often display some characteristic features, for ex-ample the emergence of spatiotemporal patterns and self-organization [2, 3]. Emergence refers to the occurrence of a behaviour which could not be anticipated from the single system. Self-organization refers to the spontaneous occurrence of the emergent patterns in the system.

The power of computer simulations has been helped us understand the collective be-haviour of such complex system. In a simulation, the complex system is described by local dynamics which may be nonlinear, and the nature of interaction between the local units. The nature of interaction is modelled by (i) network topology, where nodes repre-sent to the dynamical units and the connections among dynamical units is represented by (directed or undirected) edges of the graph, (ii) coupling forms, ranging from diffusive to pulsatile. For instance, the cell is a complex network of chemicals connected by chemical reactions, the internet is a complex network of routers and computers linked by various physical or wireless links, social networks are where nodes are human being and edges represent various relationships, ecological networks such as the food web, have nodes that are species with edges representing predator-pray relationship between them, power-grid networks, where the nodes are generators, transformers, and sub-stations and the edges are high voltage transmission lines [4].

In this thesis our main focus will be on collective spatiotemporal patterns emerging in complex dynamical networks which are determined by the interplay of the dynamics of the nodes and the nature of the interactions among the nodes. In order to understand the emergent collective spatiotemporal behaviour or patterns in complex systems we have to consider these three relevant quantities: (a) time (b) space and (c) state variables. States variable depend on physical entities of interest, for instance temperature, pressure, populations in ecosystems, velocity in fluids etc. Therefore, in order to capture the dynamical behaviour of complex systems, one needs to follow a set of relevant state variables over space and time.

In the following sections we will discuss the specific nonlinear dynamical systems and networks which we have studied in this thesis.

## 1.1 Nonlinear Dynamical Systems

*Discrete-time dynamical systems*

The Ricker map is widely used in ecological literature for modeling population growth of species with non-overlapping generations [5]. It is discrete-time dynamical system given by the following form:

$$x_{n+1} = f(x_n) = x_n \exp(r(1 - x_n)) \tag{1.3}$$

where $r$ is interpreted as an intrinsic growth rate and (dimensionless) $x_n$ is the population scaled by the carrying capacity at generation $n$. This belongs to the class of
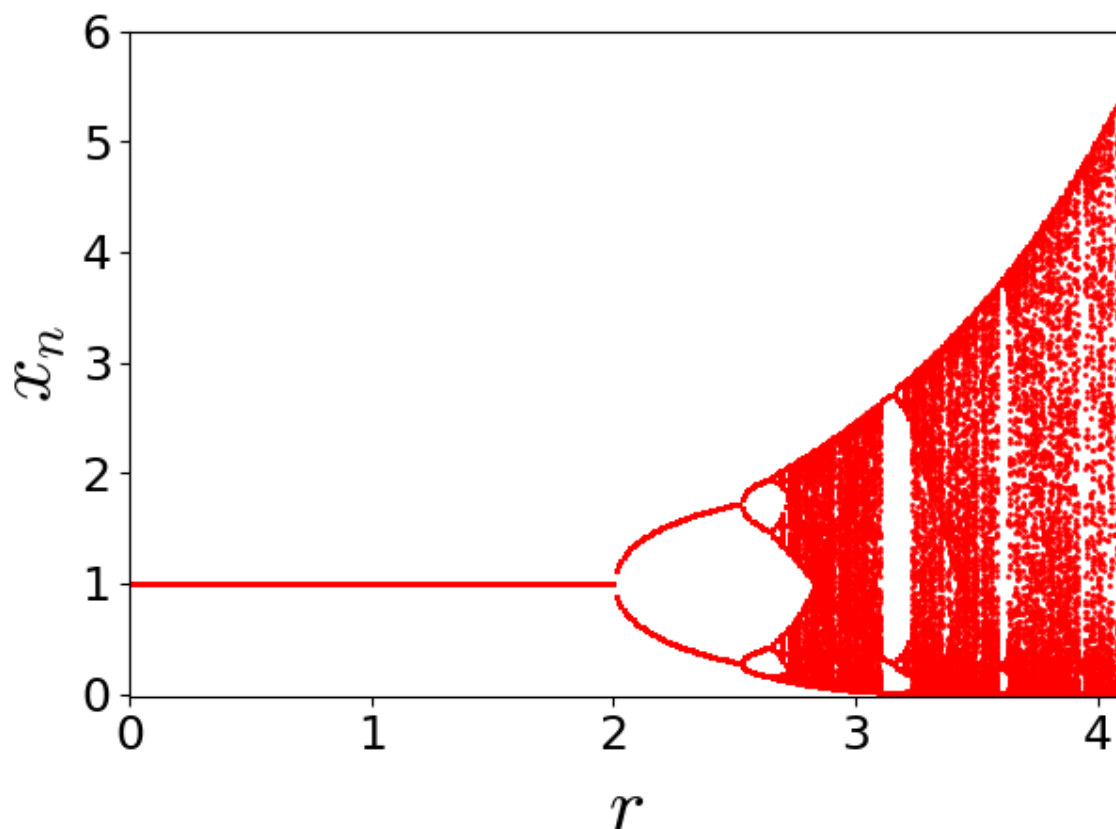


Figure 1.1: Figure shows the bifurcation diagram of the Ricker map as defined by Eqn. 1.3 as a function of growth rate parameter, $r$.

maps defined over the semi-infinite interval $[0, \infty)$ unlike logistic map which is defined in a finite, bounded interval $[0, 1]$. Ricker map displays rich dynamics ranging from fixed point to periodic cycles and chaos (cf. Fig. 1.1). Further, since this map is well defined over a large range of $x$ values, it allows us to explore a larger range of coupling strengths between the nodes than the logistic map, which is well-behaved only in a restricted interval.

*Continuous-time dynamical systems*

Following are continues-time dynamical systems modelled as nonlinear ordinary differential equations, which we have used in this thesis:

## 1.1.1 Duffing Oscillator

The Duffing oscillator is governed by the nonlinear second order differential equation given by Eqn. 1.4. It is used to model certain damped and driven oscillators, for instance a spring pendulum [6] whose spring stiffness does not exactly obey Hook's law.

$$\ddot{x} + \delta\dot{x} + \alpha x + \beta x^3 \quad = \quad a\,sin(\omega t) \tag{1.4}$$

Associating $\dot{x} = y$ gives:

$$\begin{aligned} \dot{x} &= y \\ \dot{y} &= -(\delta y + \alpha x + \beta x^3) + a\,sin(\omega t) \end{aligned} \tag{1.5}$$

Where $\delta$ controls the amount of damping, $\alpha$ control the linear stiffness, $\beta$ controls the amount of nonlinearity in the resorting force, $a$ is the amplitude and $\omega$ is the angular frequency of the periodic driving force.
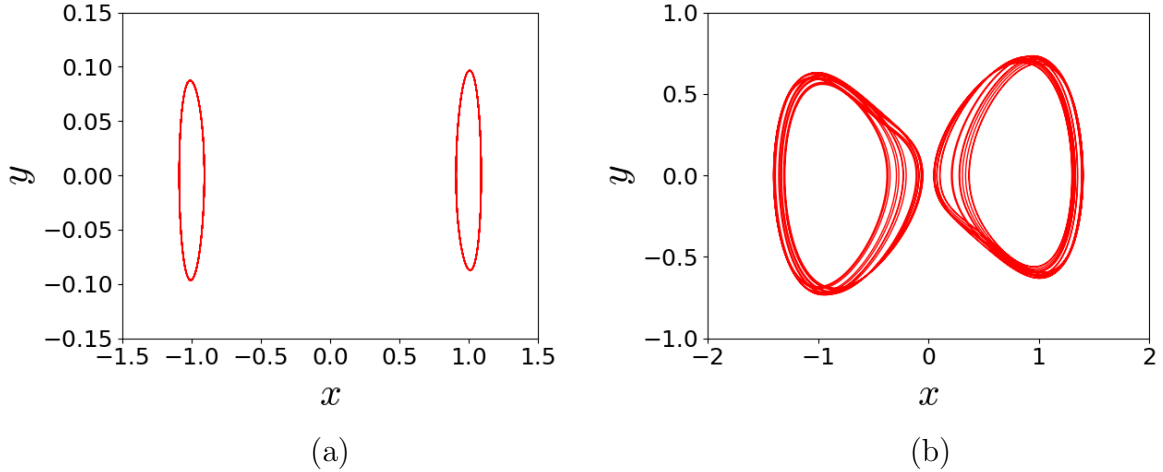
Figure 1.2: Multi-stable dynamics in the Duffing oscillator (with $\alpha = 1$, $\delta = 0.5$, $\beta = -1$, $\omega = 1$), for (a) $a = 0.1$ displaying co-existing limit cycles, and (b) $a = 0.36$ displaying co-existing chaotic attractors.

This system displays rich dynamics ranging from fixed point to limit cycles and chaos. It is evident from Fig. 1.2 that this system shows co-existence of limit cycles and chaotic attractors.

### 1.1.2 Rössler Oscillator

The Rössler attractor is a solution to a set of continuous-time coupled ordinary differential equations given by a German biochemist, *Otto Rössler*[7, 8] who was motivated by the search for *chemical chaos*, corresponding to chaotic behaviour in far-from-equilibrium chemical kinetics. The following equations, known as Rössler system were proposed by him :

$$\dot{x} = -y - z$$
$$\dot{y} = x + ay$$
$$\dot{z} = b + z(x - c) \tag{1.6}$$

Here, $(x, y, z) \in \mathbb{R}^3$ are dynamical variables defining the phase space and $(a, b, c) \in \mathbb{R}^3$ are parameters. The Rössler system is one of the minimal continuous-time systems that yield chaos because (i) its phase space has dimension three, which is the minimum number of variables needed to obtain chaos in a continuous-time model, and (ii) its nonlinearity is also minimal because there is only a single quadratic term in the evolution equation of

the $z$ variable. Further, it generates a chaotic attractor with a single lobe (cf. Fig. 3.3), unlike the double-scroll Lorenz attractor (cf. Fig. 1.4).



Figure 1.3: Chaotic trajectory of the Rössler system given by Eqn. 1.6. The values of the parameters are $\sigma = 0.15, \beta = 0.4, r = 8.5$ in Eqn. 1.6.

### 1.1.3   Lorenz System

The Lorenz system is comprised of three ordinary differential equations known as Lorenz equations, proposed by Edward Lorenz. He developed these equations to study a model of thermal convection in the earth's atmosphere [9]. The Lorenz equations are given by:

$$\begin{aligned}
\dot{x} &= \sigma(y - x) \\
\dot{y} &= x(r - z) - y \\
\dot{z} &= xy - \beta z
\end{aligned} \tag{1.7}$$

Here, (x,y,z) $\in \mathbb{R}^3$ are dynamical variables defining the phase space and $(\sigma, \beta, r) \in \mathbb{R}^3$ are parameters. This system is one of the celebrated examples of deterministic chaos. The most commonly used parameters in simulations where the system exhibits chaos (cf. Fig. 1.4) are $\sigma = 10$, $\beta = 8/3$ and $r = 28$. For these parameters the system displays extreme sensitivity to initial conditions.
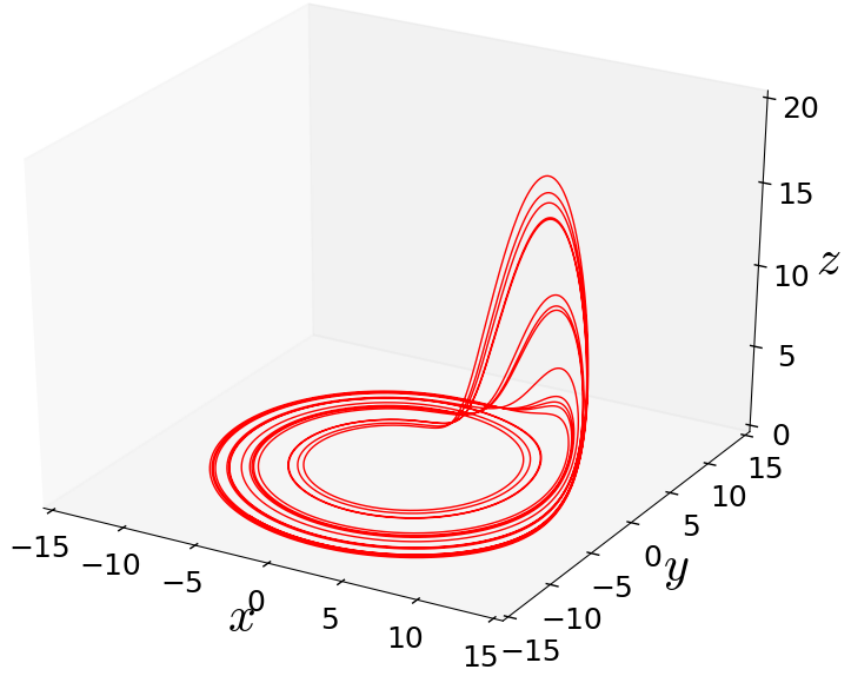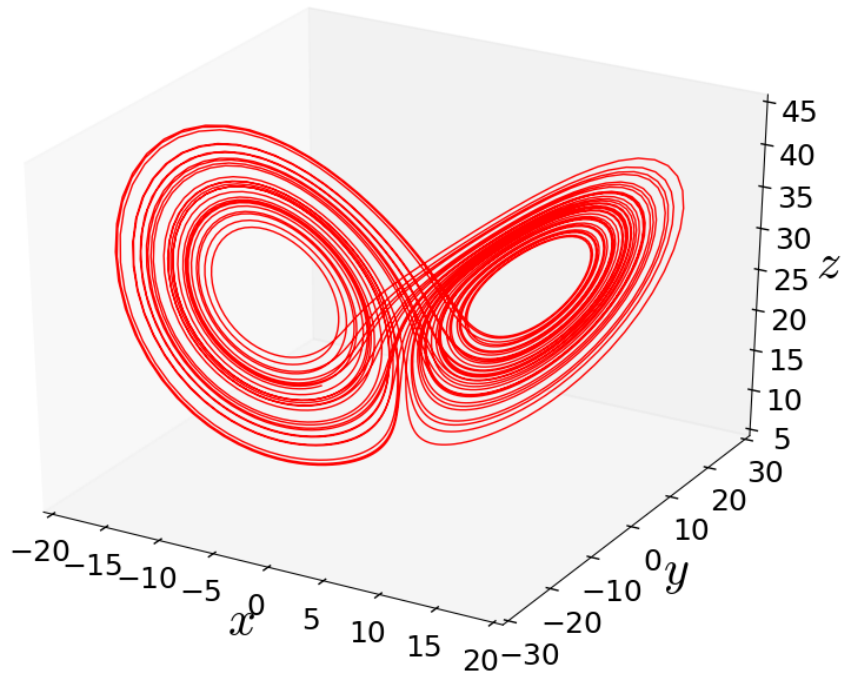
Figure 1.4: Chaotic trajectory of the Lorenz system given by Eqn. 1.7. The values of parameters are $\sigma = 0.15$, $\beta = 0.4$, $r = 8.5$ in Eqn. 1.7.

## 1.2 Networks

Network theory is a powerful tool for describing large interactive systems. A network gives us a very intuitive way of representing the complexity of couplings and linkages between systems. It can offer a overview and visualization of the interconnections within a complex system. Through the framework of networks we can get a quick sense of the significant nodes in the system, and other critical information that help us understand the system as a whole.

Networks are of two principal types. First, we have homogeneous networks in which all nodes have the same connection features, for instance Ring networks where all nodes have the same degree. Secondly, we have heterogeneous networks where the nodes comprising the network have different connection properties. For instance in Star networks and Scale-Free networks, the degree of connectivity of the nodes are different.

## 1.2.1   Ring

Ring network is a homogeneous network where all nodes have the same number of neighbours. Each node has degree $K$ ($K$ even) and is connected to $K/2$ nearest neighbors on either side (see fig. 1.5).
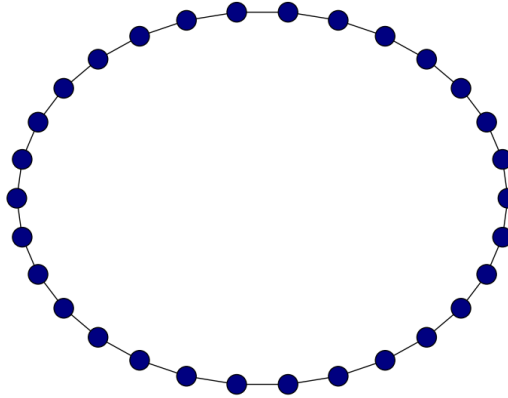


Figure 1.5: Ring network of size $N = 30$ and $K = 2$.

## 1.2.2   Star Network

In the star network there is one central node, often called hub. This is connected to all peripheral nodes, and all peripheral nodes are connected only to the central hub node. Thus indirectly hub node binds to all peripheral nodes together. Star networks are often found in computer networks, for instance a network where the peripheral nodes are clients and the central node is the server. This topology makes it simple to add additional nodes and search for faults. In this topology failure of one work-station does not affect the work of entire network but the failure of central hub will result in the failure of the whole network.
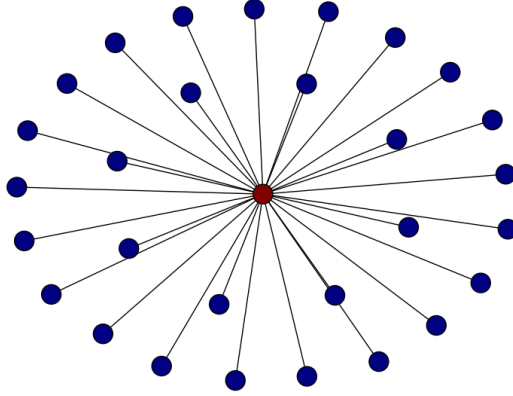
Figure 1.6: Star network of size $N = 30$.

## 1.2.3 Random Scale-Free (RSF) Network

The RSF topology is effective in capturing many real-world biological, social and technological systems. According to the Barabasi-Albert model [10] RSF network emerges in the presence of two fundamental processes: (i) Network growth, i.e. the scenario where networks are not static, but grow with time, (ii) Preferential attachment, i.e. the case where newly added nodes are more likely to link to already highly connected nodes, and this leads to the formation of hubs. As a result of these two process RSF networks follow a power-law degree distribution. An important parameter in RSF is the number of links each new node has, denoted by parameter $m$.



(a)                                    (b)
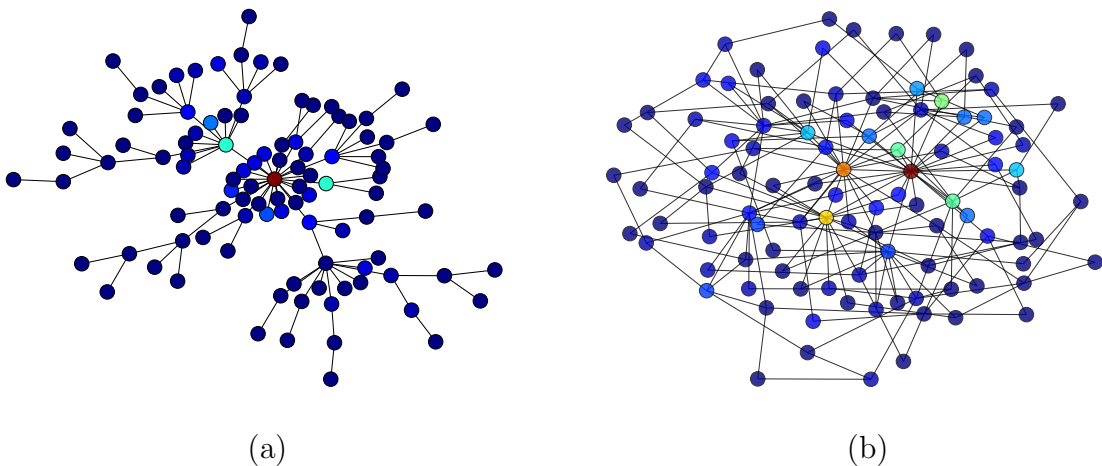
Figure 1.7: Random Scale-Free Networks constructed according to Barabasi-Albert model Ref. [10]) of size $N = 100$ with $m = 1$ (a) and $m = 2$ (b).

9

## 1.3  Outline of the Thesis

The outline of the thesis chapters are as follows:

In Chapter 2 we present the first research problem, where we study the dynamics of two coupled nonlinear delay differential system modeling the El Niño/ Southern Oscillation (ENSO) phenomenon. We investigate the range of temporal patterns emerging from this system under variation of the time delay in the oceanic waves, the self-delay interaction strength of oceanic waves, and the coupling strength between the two regions. We explore the collective behaviour of the coupled systems in the space of these three parameters for homogeneous and heterogeneous cases. Further, we study the existence, and basins of attraction of the solutions arising in the model system, for different representative parameter sets. We explicitly obtain the basins of attraction for the different steady states and oscillatory states in the model and these can help in understanding patterns in the sea surface temperatures anomalies in monitored coupled sub-regions. We also explore the robustness of the different dynamical states under noisy evolution, in order to gauge which set of attractors are typically expected to arise when the system evolves under the influence of external perturbations.

In Chapter 3 we present the second research problem, where we study Star networks of diffusively, conjugately and mean-field coupled nonlinear oscillators, with all end nodes connected only to the central hub node. We find that the end-nodes which are equivalent in terms of the coupling environment and dynamical equations, yielded chimera states, i.e. the symmetry of the end-nodes is broken and coexisting groups with different synchronization features and attractor geometries emerged. Further, we analyse the global stability of the chimera states through the measure of basin stability. This allow us to obtain the range of coupling strengths where chimera states has high prevalence.

In Chapter 4, we present the third research problem, where we study Random Scale-Free networks of $N$ sub-systems of population patches or "a population of populations". populations, modeled by a nonlinear map (the Ricker map), typically chaotic, connected by transport that is triggered when population density in a patch is in excess of a critical threshold level. The broad scenario of threshold-activated transport is that each population patch has a critical population density it can support, and when the population in the patch, due to its inherent growth dynamics (which may be chaotic) exceeds this threshold, the excess migrates to neighbouring patches. The neighbouring patch on

receiving the migrant population may become over-critical too, triggering further migrations. So this form of coupling is pulsatile and inter-patch transport occurs only when there is excessive build-up of population density in a patch, which may initiate a *cascade of transport events*. First, we study the effect of threshold-activated dispersal on the dynamical patterns emerging in the network. Next our question is, can threshold-activated coupling serve to stabilize the intrinsically chaotic populations in the network to regular behaviour, such as steady states or regular cycles? Further, we explore the case of networks with very few (typically 1 or 2) open nodes, and study the effect of the degree and betweenness centrality of these open nodes on the control to steady states. Additionally, to estimate the efficiency and robustness of the suppression of chaos in the network, we study a couple of qualitative and quantitative measures, for instance, average redistribution time $\langle T \rangle$ and average range of threshold values yielding steady states $\langle R \rangle$.

In Chapter 5 we investigate the collective dynamics of multistable chaotic systems connected in different network topologies, ranging from rings and small-world networks, to scale-free networks and stars. We estimate the dynamical robustness of such networks by introducing a variant of the concept of multi-node basin stability, which allows us to gauge the global stability of the dynamics of the network in response to local perturbations affecting a certain class of nodes of a system. This approach is important in deciding which nodes to safeguard in order to maintain the collective state of this network against targetted localized attacks.

We conclude with Chapter 6, where we present a summary of the salient results obtained in this thesis, and also give a broad outline for open future directions.

# Chapter 2

# Coupled nonlinear delayed system modelling El Niño Southern Oscillations

## 2.1 Introduction

El Niño Southern Oscillations (ENSO) is naturally occurring phenomenon in which Equatorial Pacific fluctuates between warmer-than-average (El Niño) and colder-than-average (La Niña) conditions. The changes in Sea Surface Temperatures affect the distribution of tropical rainfall and atmospheric circulation features. The term El Niño typically signifies a very large scale warm event, and this dramatic change in Sea Surface Temperature (SST) is one phase of the ENSO, that is an irregular cycle of coupled ocean temperature and atmospheric pressure oscillations across the equatorial Pacific region [11, 12, 13, 14](cf. Fig. 2.1). El Niño is an ocean-atmospheric phenomenon, occurring at intervals of two to seven years. El Niño event especially has great influences on climate which may further cause extensive natural disasters like flood and drought across the globe, declines in fisheries, famine, plagues etc. It has attracted much popular interest as it has global impact that ranges from environment to economics.
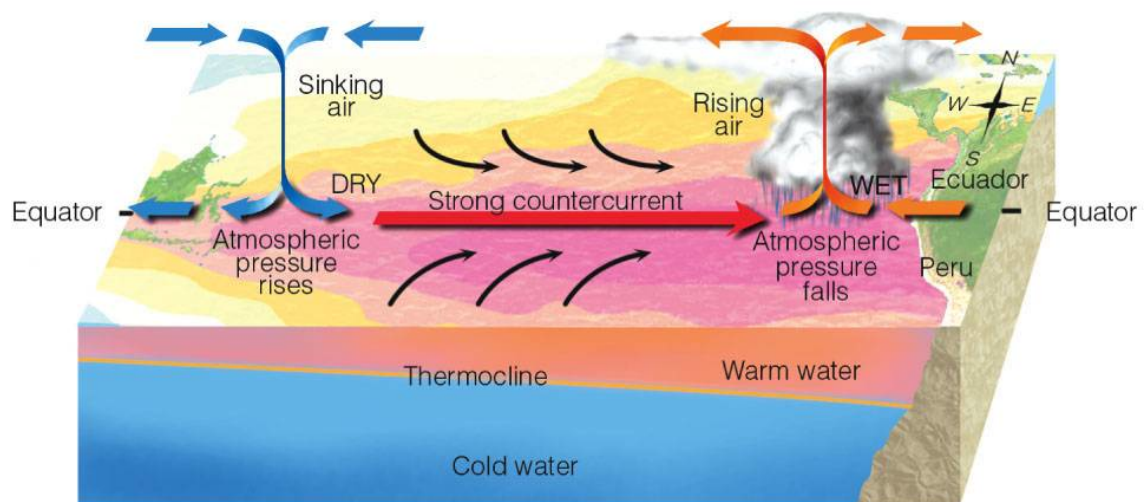


Figure 2.1: Figure represents a schematic El Niño phenomenon. Figure retrieved from http://www.riversideca.gov/elnino/.

In normal years, SST of the western Pacific Ocean is high and pressure is low compared to the eastern Pacific Ocean. Due to high SST in the western region, evaporation increases and high rainfall occurs there. Less rainfall occurs in the east due to cold SST and high pressure levels. A pressure gradient in the east and west pacific ocean induces circulations of trade winds. These circulating trade winds in turn affect the depth of the thermocline gradient. In normal conditions, the thermocline is deeper in the western Pacific region

and shallower in the eastern region. However when the El Niño becomes very strong, the circulation of trade winds changes its direction. As a result the thermocline depth becomes almost the same in both east and west Pacific Ocean. In contrast to El Niño, La Niña is the cold phase of ENSO, with the cycle of hot and cold phases having an average periodicity of approximately 3.7 years.

The first modern mechanism underlying ENSO was proposed by Bjerknes. He hypothesized that positive feedback between the atmosphere and the equatorial eastern Pacific ocean leads to the El Niño effect [15]. Now positive ocean-atmosphere feedback is responsible for the growth of internal instabilities, that can produce very large SST anomalies in the eastern tropical Pacific region. To keep the instability in the SST anomalies bounded, negative feedback is necessary. Therefore to gain understanding of the positive-negative feedback mechanisms underlying the emergence of ENSO, several low order models (LOM) have been introduced in the past decades. For instance, one of the earliest efforts to obtain ENSO-like oscillations was proposed by Zebiak and Cane [16], and the effect of the ocean and atmosphere on each other was central to their model. Based on the coupled model of Zebiak and Cane, the recharge oscillator model was proposed by Jin, based on the recharge and discharge process of warm water over tropical Pacific ocean [17, 18]. Subsequently, consistent with the observations of ENSO, the western Pacific oscillator model [19, 20] was proposed, where the role of the western Pacific in ENSO was emphasized. Other attempts include that by Picaut, who introduced an advective-reflective oscillator, which includes a positive feedback of zonal currents that advect from the western Pacific warm pool toward the east during El Niño [21]. The main motivation of such simple models is to gain understanding of the underlying mechanisms of ENSO, through basic models involving a small number of variables, that are capable of provide qualitative description of the complex phenomenon of ENSO [22, 23, 24].

One important class of models attempting to understand the behaviour of ENSO is the deterministic low order *delayed action oscillator model* [25, 26]. This model will be the focus of this chapter. Delayed negative feedback models provide a very good, yet simple, representation of the basic mechanism of ENSO-like oscillations. An important feature of this class of models is the inclusion of a delayed feedback which incorporates oceanic wave transit effects, namely the effect of trapped ocean waves propagating in a basin with closed boundaries. Specifically, the delayed action oscillator model has three terms, and is a first order nonlinear delay differential equation for the temperature anomaly $T$, i.e. the deviation from a suitably long term average temperature, given by:

$$\frac{dT}{dt} = kT - bT^3 - AT(t - \Delta) \tag{2.1}$$

Here the coupling constants are $k$, $b$ and $A$, with $\Delta$ being the delay. The first term represents a positive feedback in the ocean-atmosphere system, working through advective processes giving rise to temperature perturbations that result in atmospheric heating. The heating in turn leads to surface winds driving the ocean currents which then enhance the anomalous values of $T$. The second term is a damping term, due to advective and moist processes, that limits the temperatures from growing without bound. The delay term arises from considerations of equatorially trapped ocean waves propagating across the Pacific and interacting back after a time delay, determined by the width of the Pacific basin and wave velocities. The strength of this interaction, relative to the nondelayed feedback is given by $A$.

We will consider the dimensionless form of this equation [27]:

$$\frac{dT}{dt} = T - T^3 - \alpha T(t - \delta) \tag{2.2}$$

where time in Eqn. 2.2 has been scaled by $k$, temperature by $\sqrt{b/k}$. The dimensionless constants $\alpha = A/k$ and $\delta = k\Delta$ [27]. This model allows multiple steady states and when these fixed points become unstable, self-sustained oscillations emerge. Thus this class of models provide a simple explanation of ENSO, and provides insights on the key features that allow the emergence of oscillatory behavior.

The delayed-oscillator model given by Eqns. 2.1-2.2 above considers a single representative region in the Pacific Ocean. Now it is clear that the geographical stretch where El Niño is relevant is too vast to be well-modelled by a single system. Further, several agencies such as the National Oceanic and Atmospheric Administration (NOAA) in the United States, monitor the sea surface temperatures in various locations, and there are five regional blocks in the Equatorial area extending from 80 West to 160 East meridian. So in order to make potential connections with data from different locations, as well as to gain some broad understanding of the effect of coupling of sub-regions, it is useful to study extensions of the delayed oscillator model that incorporate more than one region.

So in this chapter we will consider a coupled delayed oscillator model, mimicking two coupled Equatorial sub-regions, and explore its dynamical behaviour. We will investigate emerging patterns in the model with varying self-delay coupling strengths in the sub-regions along the Equator, as well as varying (possibly strong) delay times. Our principal

motivation will be to explore the effect of coupling and sub-region heterogeneity on the ENSO-like oscillations arsing in the model, an aspect not explored in earlier studies.

## 2.2    Coupled Delayed Oscillator Model

Now we consider the model, extending Eqns. 2.12.2 to incorporate two sub-regions of the Pacific. Consider two coupled sub-regions, given by following dimensionless delay differential equations, as introduced in [27]:

$$\frac{dT_1}{dt} = T_1 - T_1^3 - \alpha_1 T_1(t - \delta_1) + \gamma T_2 \tag{2.3}$$
$$\frac{dT_2}{dt} = T_2 - T_2^3 - \alpha_2 T_2(t - \delta_2) + \gamma T_1$$

Here $T_i$, $\delta_i$ and $\alpha_i$ with $i = 1, 2$ are the scaled temperature anomaly, self-delay, strength of the self-delay of each sub-region, and $\gamma$ is the inter-region coupling strength between the two regions. The form of the coupling term models the situation where if one region is cooler than the other, then the flow of energy across their common boundary will result in heating one sub-region and cooling the other.

In this chapter we consider two cases. The first case considers coupled identical sub-regions where values of all the parameters are same, implying that the two regions are geographically close-by, and the distance from the western boundary is approximately same. Secondly we consider coupled non-identical sub-regions, where there is heterogeneity in the parameters. This implies that the two regions are geographically far or different, and the distance from the western boundary is also different. We give the salient dynamical features arising in these systems in the following sections.

## 2.3    Dynamics of coupled identical sub-regions

First we consider the case of identical sub-regions, i.e. $\alpha_1 = \alpha_2$ and $\delta_1 = \delta_2$. This arises when the two regions are geographically close-by, and the distance from the western boundary is approximately same, with the same losses and reflection properties for both regions and similar transient time taken by the oceanic waves. Four distinct types of behaviour emerge in this case:

(i) Amplitude Death (AD) : here both regions go to a single steady state. See left panel of Fig. 2.2 for a representative example.

(ii) Oscillation Death (OD): here the sub-regions go to different steady states. See right panel of Fig. 2.2 for a representative example.

(iii) Homogeneous oscillations : here the regions oscillate synchronously and there is no phase or amplitude difference between the oscillations. See Fig. 2.3a for a representative example.

(iv) Heterogeneous oscillations : here the oscillatory patterns are complex, and the oscillations in the two sub-regions differ in either phase or amplitude, or both. Further, the oscillations may be irregular for certain parameters. See Fig. 2.3b for representative example. Anti-phase synchronization occurs only when initial conditions are $T_1 = 0.5$ and $T_2 = -0.5$.



(a)                                             (b)
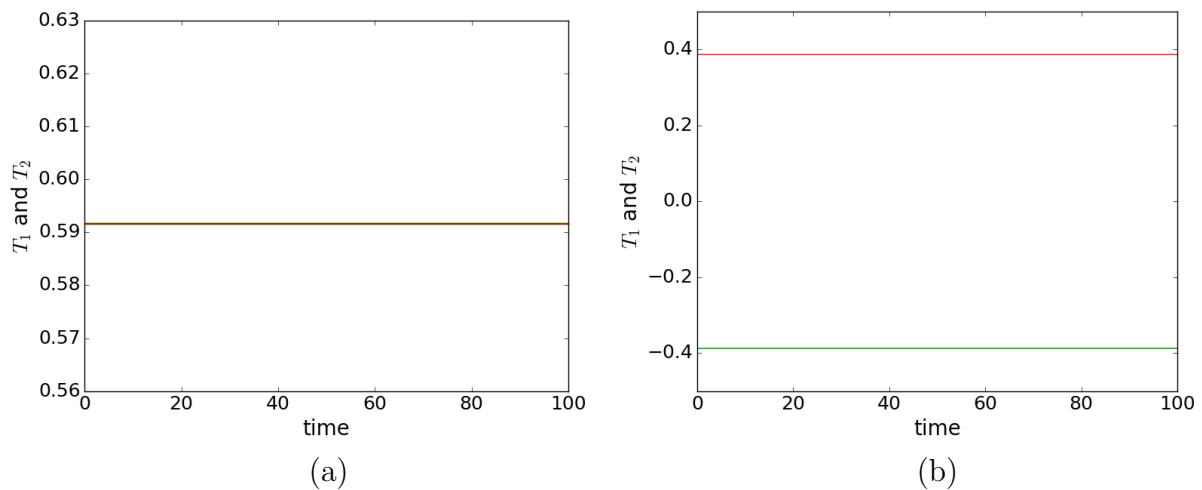
Figure 2.2: Temporal evolution of the temperature anomalies of the two sub-regions $T_1$ (in red) and $T_2$ (in green) with $\alpha_1 = \alpha_2 = 0.75$, $\delta_1 = \delta_2 = 1$, and inter-region coupling $\gamma = 0.1$ (a) initial condition $T_1 = 0.5$, $T_2 = 0.5$ and (b) initial condition $T_1 = 0.5$, $T_2 = -0.5$, showing amplitude death and oscillator death behavior respectively.
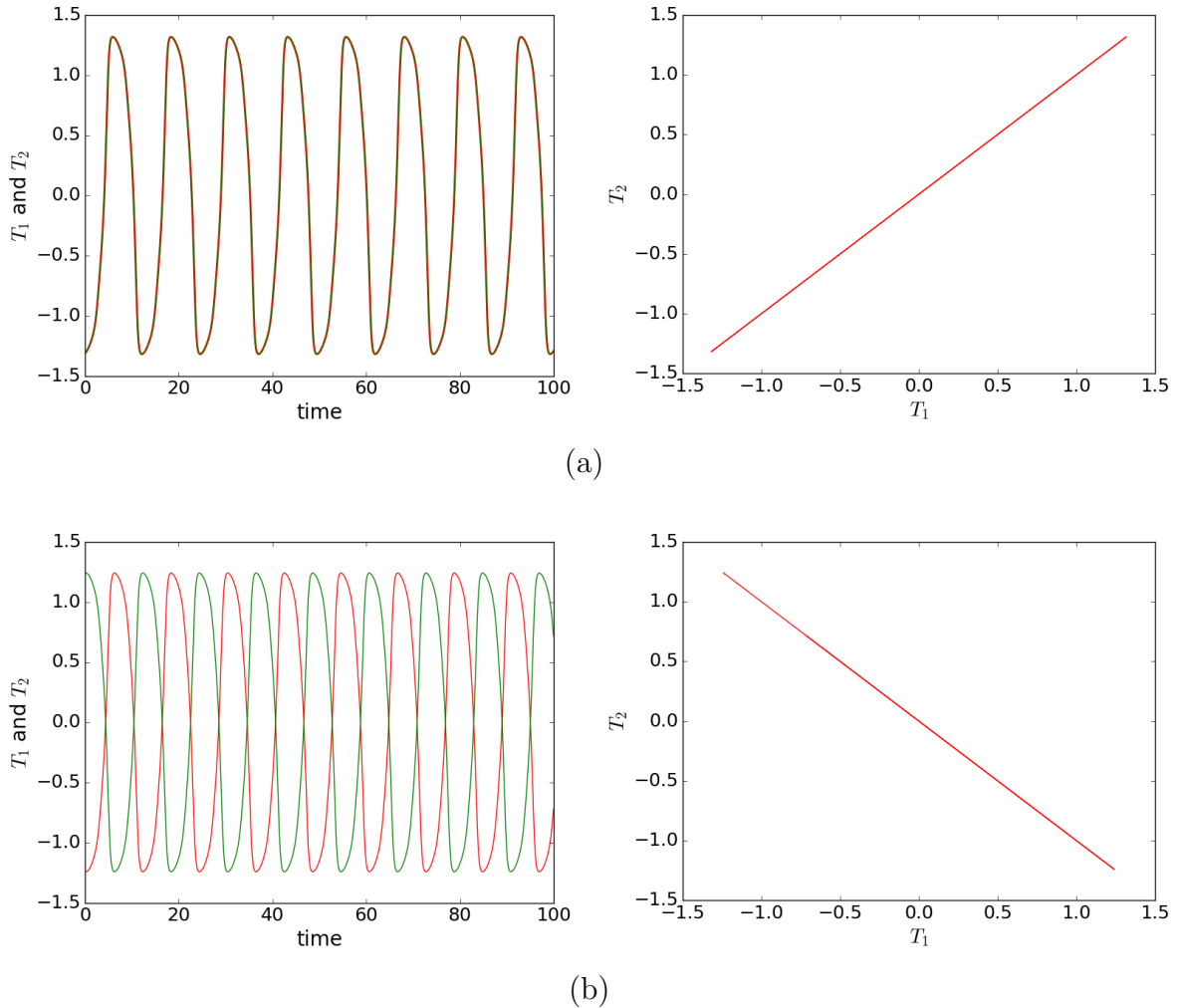
Figure 2.3: Temporal evolution of the temperature anomalies of the two sub-regions $T_1$ (in red) and $T_2$ (in green) in the left panel, and the corresponding phase portrait in the $T_1 - T_2$ plane in the right panel, for $\alpha_1 = \alpha_2 = 0.75$, $\delta_1 = \delta_2 = 4$ and $\gamma = 0.1$ in Eqn. 2.3. Initial conditions for (a) $T_1 = 0.5$, $T_2 = 0.5$ and for (b) $T_1 = 0.5$, $T_2 = -0.5$.

In numerical simulations we distinguish between the different dynamical behaviours as follows: after a long transient period, we calculate the minima and maxima, as well as the difference in amplitude of $T_1/T_2$ of the two sub-regions. If $|T_1 - T_2|$ is less than a prescribed small accuracy threshold, and the difference between the maxima and minima is also less than the threshold, then the state is identified as amplitude death. If $|T_1 - T_2|$ is less than the threshold, and the difference between the maxima and minima is greater than the threshold, then the state is identified as homogeneous oscillations. If $|T_1 - T_2|$ is greater than the threshold, and the difference between the maxima and minima is less than the threshold, then the state is identified as oscillator death. If $|T_1 - T_2|$ is greater than the threshold, and the difference between the maxima and minima is also greater than

the threshold, then the state is identified as heterogeneous oscillations. Specifically, here we consider the accuracy threshold value to be $10^{-3}$. Note that the emergent dynamical patterns are not very sensitive to this threshold value. The qualitative dynamical patterns that may be expected to arise from a generic initial state is evident from the phase diagrams shown in Figs. 2.4 and 2.5. It is evident from these that oscillations emerge as the delay $\delta$ and strength of self-delay coupling $\alpha$ increases, and as inter-region coupling strength $\gamma$ decreases. Importantly, as compared to a single region model, oscillations arise for larger values of delay in the two coupled sub-regions model. This implies that coupling of sub-regions yields smaller parameter regions giving rise to ENSO-like oscillations.



Figure 2.4: Phase diagram showing the dynamics of the temperature anomaly in mean sea surface temperature of a sub-region $(T_1/T_2)$, with respect to inter-region coupling $\gamma$ and delay $\delta_1 = \delta_2 = \delta$. Here the strength of delayed coupling in the two regions is $\alpha_1 = \alpha_2 = 0.75$, in Eqn. 2.3. The black color represents amplitude death, red represents oscillator death, yellow represents homogeneous oscillations and green represents heterogeneous oscillations.

We explore the dynamics arising from a large sample of random initial conditions in the range $-1$ to $1$, and we observe that the number of attractors and their basin stability depend upon the values of the parameters.

Generically, there is a complex co-existence of attractors. For instance, in Figs. 2.4-

2.5, the parameter regions with inter-mixed colors implies co-existing dynamical states, such as co-existing amplitude death (AD) and oscillator death (OD) states where there are red dots interspersed in the black region. As the strength of the inter-region coupling $\gamma$ increases, co-existence of AD and OD decreases.
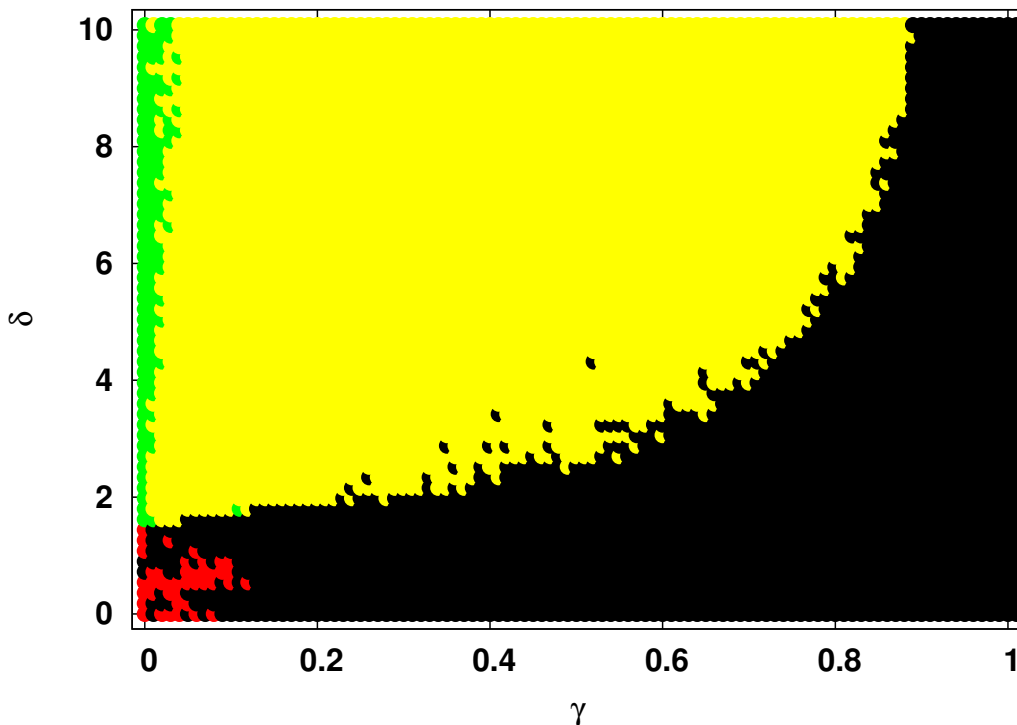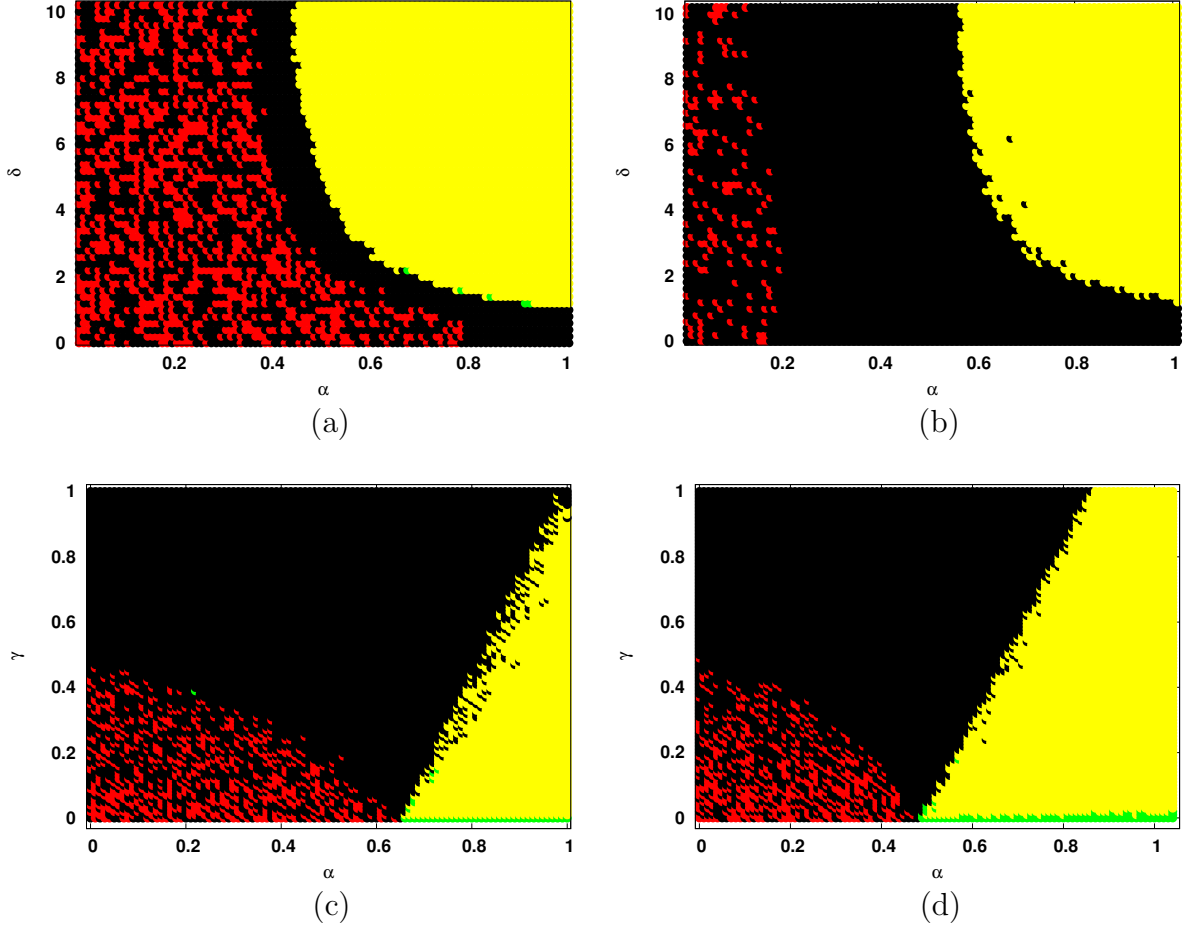


Figure 2.5: (a,b) Phase diagram showing the dynamics of the temperature anomaly in mean sea surface temperature of a sub-region $(T_1/T_2)$ with respect to delay $\delta_1 = \delta_2 = \delta$ and strengths of self-delay coupling $\alpha_1 = \alpha_2 = \alpha$. Here the inter-region coupling is $\gamma = 0.1$ (a) and $\gamma = 0.4$ (b), in Eqn. 2.3. (c,d) Phase diagram of the same system, with respect to inter region coupling strength $\gamma$ and strengths of self-delay coupling $\alpha_1 = \alpha_2 = \alpha$. Here the delay in the two regions is $\delta_1 = \delta_2 = \delta$ equal to (c) 2 and (d) 4, in Eqn. 2.3. The black color represents amplitude death, red represents oscillator death, yellow represents homogeneous oscillations and green represents heterogeneous oscillations.

Further, the region of amplitude death increases (cf. Fig. 2.5a), implying that the ENSO-like oscillations are less likely when two sub-regions are strongly coupled. We also observe that as delay $\delta$ increases, co-existence of AD and OD decreases, and the parameter region supporting oscillatory behaviour increases (cf. Fig. 2.5b). For instance,

when $\delta = 2$ oscillations emerge for self-delay coupling strength $\alpha \geq 0.65$, while for $\delta = 4$ oscillations emerge in the systems with $\alpha \geq 0.48$. So longer delays, namely longer oceanic wave transit times, favour El Niño oscillations.

## 2.4   Analysis

On the assumption that delay $\delta$ is small ($\delta < 1$), we can consider that the delayed temperature anomaly $T(t - \delta)$ to be approximated by $T(t) - \delta \frac{dT_t}{dt}$. Hence we need to solve the following dynamical equations:

$$
\begin{aligned}
(1 - \alpha\delta)\frac{dT_1}{dt} &= T_1 - T_1^3 - \alpha T_1 + \gamma T_2 \qquad\qquad (2.4) \\
(1 - \alpha\delta)\frac{dT_2}{dt} &= T_2 - T_2^3 - \alpha T_2 + \gamma T_1
\end{aligned}
$$

The Jacobian of the system above is given by:

$$
J = \frac{1}{1 - \alpha\delta}\begin{pmatrix} 1 - 3T_1^2 - \alpha & \gamma \\ \gamma & 1 - 3T_2^2 - \alpha \end{pmatrix}.
$$

The linear stability of the different fixed points that arise in this system, under varying parameters, are determined by the eigen values of $J$. Fig. 2.6 shows the number of steady states for representative parameters $\alpha$ and $\gamma$. A noticeable trend is that as the inter-region coupling $\gamma$ increases, one obtains fewer fixed points at the same value of self-delayed coupling strength $\alpha$. For instance, for small $\alpha$, nine fixed points exist for $\gamma = 0.1$, while only five fixed points are there for $\gamma = 0.6$. The other feature is that the number of fixed point solutions decreases with $\alpha$, e.g. for $\gamma = 0.1$, there are nine fixed points for small $\alpha$ and only one for large $\alpha$.

For $\gamma = 0.1$, the stability of the fixed points for different $\alpha$ is as follows: (a) for $0 \leq \alpha < 0.8$ there are 4 stable nodes, 4 saddle points and 1 unstable node, (b) for $0.8 \leq \alpha < 0.9$, there are 2 stable nodes, 2 saddle points and 1 unstable node, (c) for $0.9 \leq \alpha < 1.1$ there are 2 stable nodes and 1 saddle point, and lastly (d) for $\alpha \geq 1.1$ we obtain only one fixed point which is a stable node. For $\gamma = 0.6$ one obtains a similar stability pattern, shifted down the $\alpha$ axis, starting with 5 fixed point solutions. So this indicates that smaller inter-region coupling $\gamma$ and smaller self-delay coupling $\alpha$ yield larger number of stable fixed point solutions. One may then expect to find predominance of oscillator death, where the system goes to different steady states, in parameter regions

where these quantities are small. This observation is in concurrence with the phase diagrams shown in the sections above.
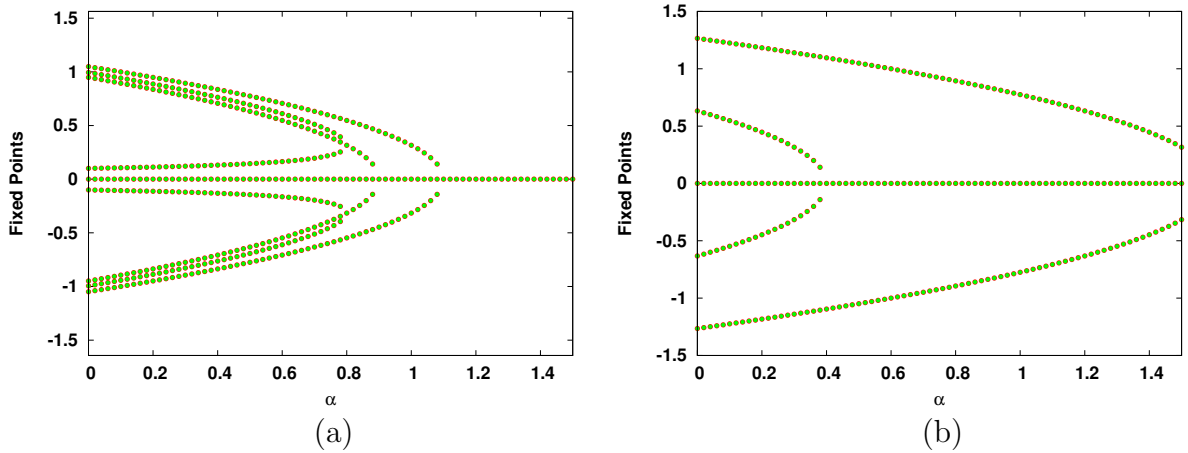


Figure 2.6: Fixed point solutions arising from Eqn. 2.4 versus strength of the self-delay coupling $\alpha$ for inter-region coupling $\gamma$ equal to 0.1 (a) and 0.6 (b).

## 2.5 Dynamics of coupled non-identical sub-regions

Now we will consider the case of non-identical sub-regions, i.e. $\alpha_1 \neq \alpha_2$ and $\delta_1 \neq \delta_2$, relevant to the case where the distance from the western boundary is different for the sub-regions and therefore the transient times taken by the oceanic waves are different in the sub-regions.

Now we consider the effects of different strength for the self-delay coupling term in the two sub-regions (i.e. $\alpha_1 \neq \alpha_2$) with the uniform delays $\delta_1 = \delta_2 = \delta$ and inter-region coupling strengths $\gamma$. Figs. 2.7-2.8 show the typical dynamics emerging under varying differences in the two sub-regions $\Delta\alpha = \alpha_1 - \alpha_2$. When the difference in the strengths of the self-delay coupling is small ($\Delta\alpha < \alpha_{1,2}$), we observe that both sub-regions display similar behaviour for strong inter-region coupling (cf. Fig. 2.7b). However for weaker inter-region coupling, different dynamical behaviour emerges in the two sub-regions. Typically, the region with stronger self-delay coupling shows regular behaviour, while the region with weaker self-delay coupling shows complex behaviour (cf. Fig. 2.7a ). This type of complex oscillation is qualitatively very similar to ENSO observational data [28, 29].
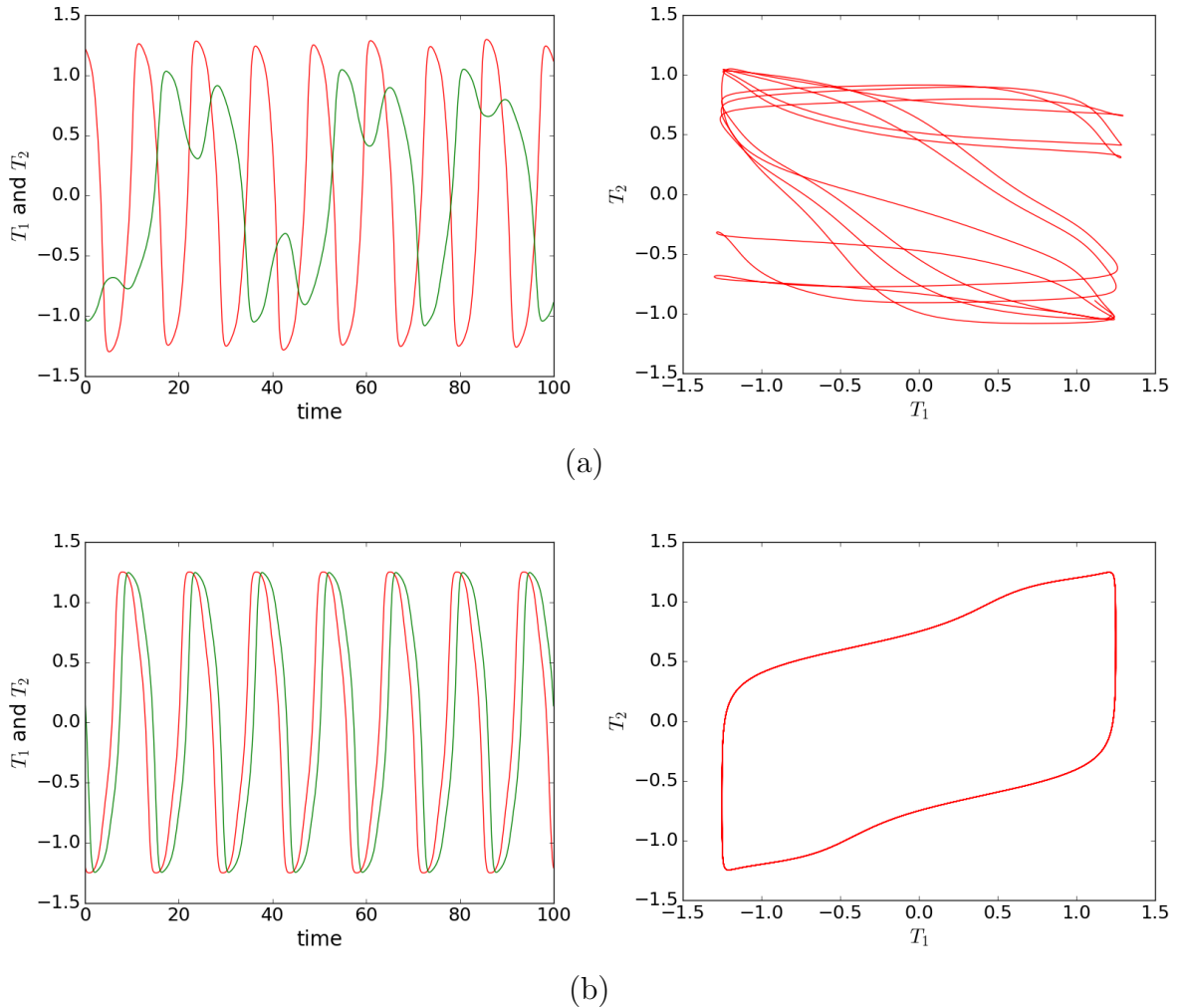
23

Figure 2.7: Temporal evolution of the temperature anomalies of the two sub-regions $T_1$ (in red) and $T_2$ (in green), in the left panels, and the corresponding phase portraits in the $T_1 - T_2$ plane in the right panels, for a system with $\alpha_1 = 0.75, \alpha_2 = 0.5$, coupling delay $\delta = 4$ and inter-region coupling strength $\gamma$ equal to (a) 0.1 and (b) 0.2, in Eqn.2.3.

When the difference in $\alpha$ is large ($\Delta\alpha > \alpha_{1,2}$), then the nature of oscillations in the two sub-regions can be very different. For instance in Fig. 2.8 one observes that one sub-region displays large amplitude oscillations in the temperature anomaly, while the other sub-region displays very small amplitude oscillations. So we see that non-uniformity in the self-coupling strengths in the systems can significantly affect the temperature anomaly of mean sea surface temperature in neighbouring sub-regions. The dependence of the emergence of oscillations on heterogeneity is displayed in more detail in a series of phase diagrams in figures 2.9 showing the parameter regimes that yield fixed points and those that gives rise to oscillations in the two sub-regions. As intuitively expected, one now no longer obtains amplitude death and homogeneous oscillations. Only oscillator death

and heterogeneous oscillations emerge when the sub-regions are characterized by different delays and self-delay coupling strength.

Further clearly, *the parameter region supporting oscillations is larger for weaker inter-region coupling strengths and small difference in self-delay coupling strengths of the two sub-regions.*



(a)



(b)
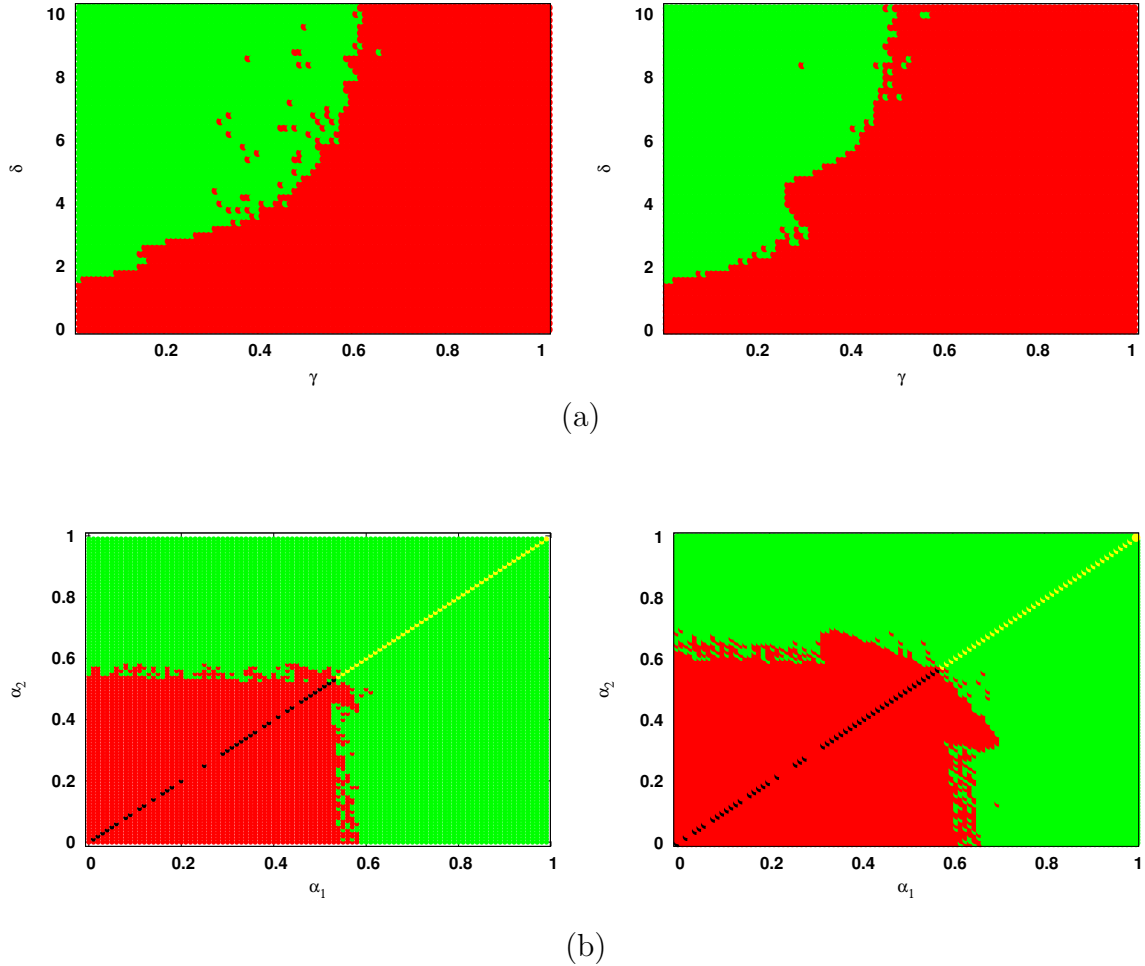
Figure 2.9: (a)Phase diagram showing the dynamics of the temperature anomaly in mean sea surface temperature $(T_1/T_2)$, with respect to inter-region coupling $\gamma$ $(\gamma > 0)$ and delay $\delta_1 = \delta_2 = \delta$. Here the strength of delayed coupling in Eqn. 2.3 is different in the two regions, with $\alpha_1 = 0.75, \alpha_2 = 0.5$ (left) and $\alpha_1 = 0.75, \alpha_2 = 0.25$ (right). (b)Phase diagram of the same system with respect to self-delay coupling strength $\alpha_1$ of first region and self-delay coupling strength $\alpha_2$ of second region. The inter region coupling strength $\gamma = 0.1$ (left) and $\gamma = 0.2$ (right) and delay in the two regions is $\delta_1 = \delta_2 = \delta = 4$ in Eqn. 2.3. The black color represents amplitude death, red represents oscillator death, yellow represents homogeneous oscillations and green represents heterogeneous oscillations. Clearly, oscillator death and heterogeneous oscillations are predominant.

Figure 2.8: Temporal evolution of the temperature anomalies of the two sub-regions $T_1$ (in red) and $T_2$ (in green), in the left panels, and the corresponding phase portraits in the $T_1 - T_2$ plane in the right panels, for a system with $\alpha_1 = 0.75, \alpha_2 = 0.25$, delay $\delta = 4$ and inter-region coupling strength $\gamma$ equal to (a) 0.1 and (b) 0.2 with initial condition $T_1 = T_2 = 0.5$,(c) 0.2 with initial condition $T_1 = 0.5$ and $T_2 = -0.5$, in Eqn.2.3.
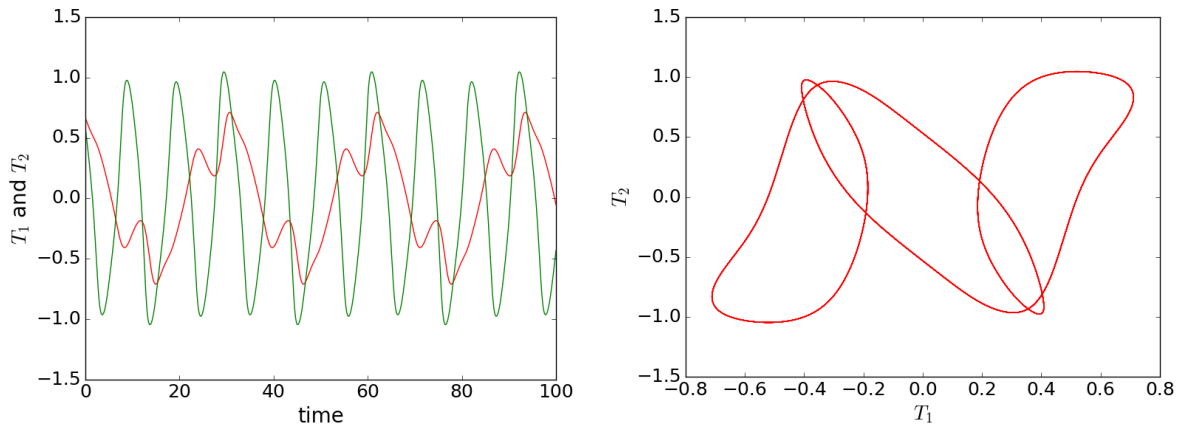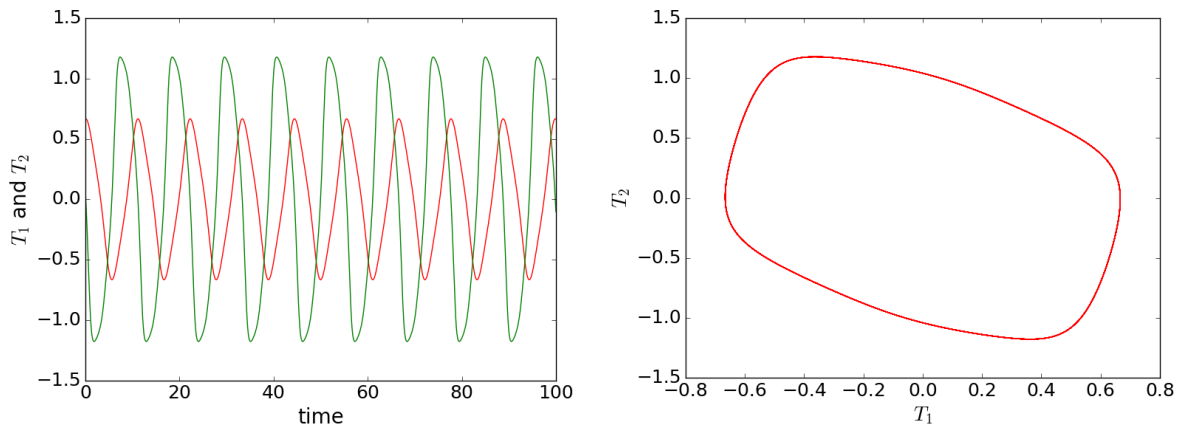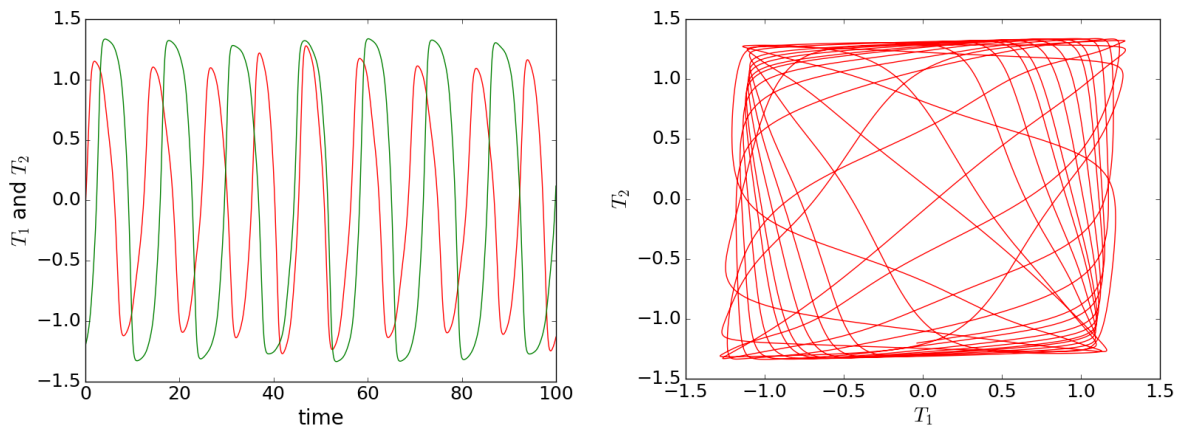
Figure 2.10: Time evolution of the temperature anomalies of the two sub-regions, with $\alpha_1 = \alpha_2 = 0.75$ (a) $\delta_1 = 1$, $\delta_2 = 2$ and $\gamma = 0.1$; (b) $\delta_1 = 1$, $\delta_2 = 3$ and $\gamma = 0.1$; (c) $\delta_1 = 3$, $\delta_2 = 5$ and $\gamma = 0.1$. The temperature anomaly of region 1, $T_1$, is shown in red and for region 2, $T_2$ is shown in green. The corresponding phase portrait is displayed on the right panel.

27

Interestingly, if we take the self-delay coupling strengths of the two sub-regions to be such that the temperature of one region goes to a fixed point regime when uncoupled, while the other system is in the oscillatory regime, then on coupling both systems show oscillations (see Fig. 2.11). This implies that oscillations may arise in certain sub-regions through coupling to neighbouring regions. Namely, a sub-region with very low delay ($\delta < 2$), which would naturally go to a steady state when uncoupled, yields oscillations when coupled to another sub-region with high enough delay ($\delta > 2$).
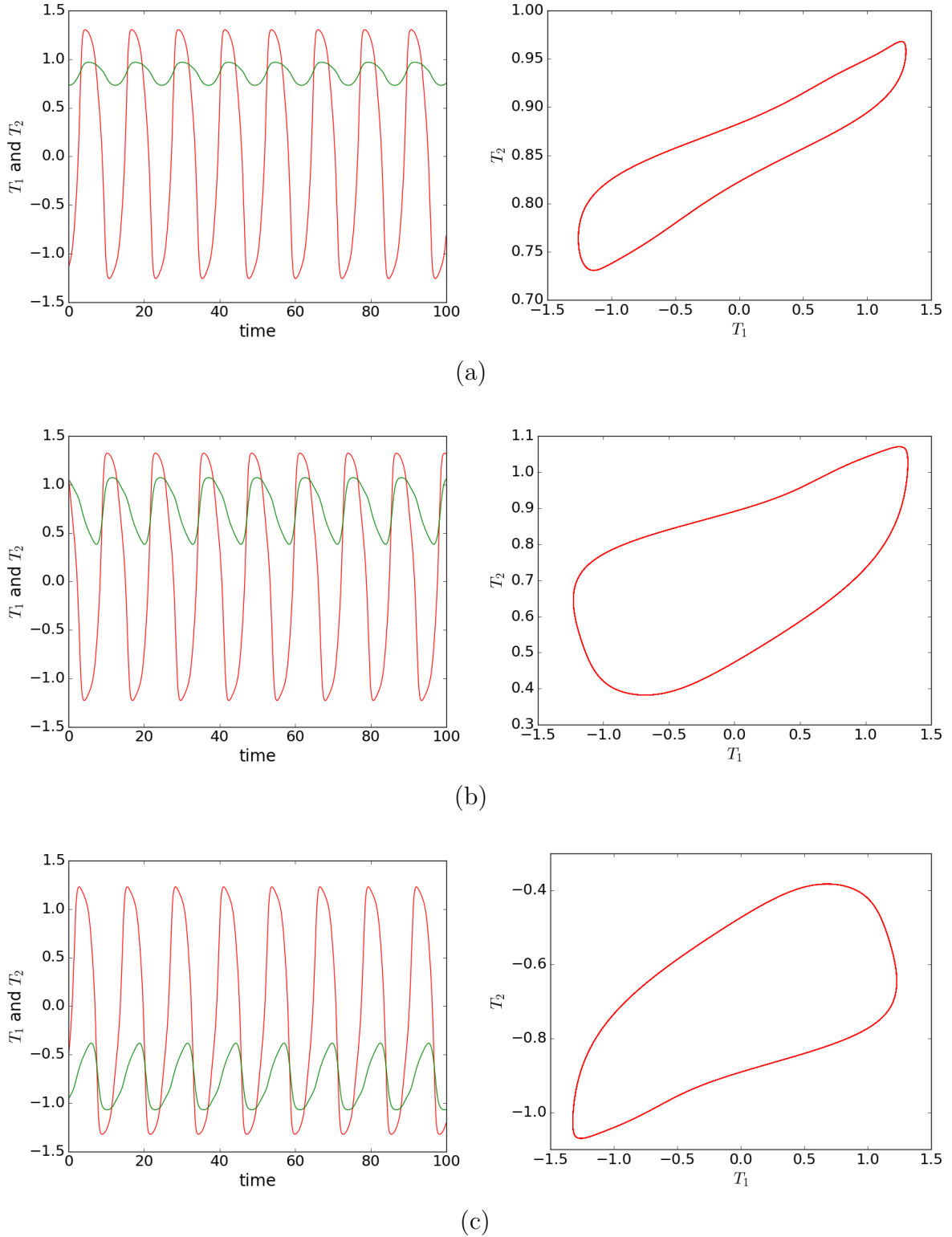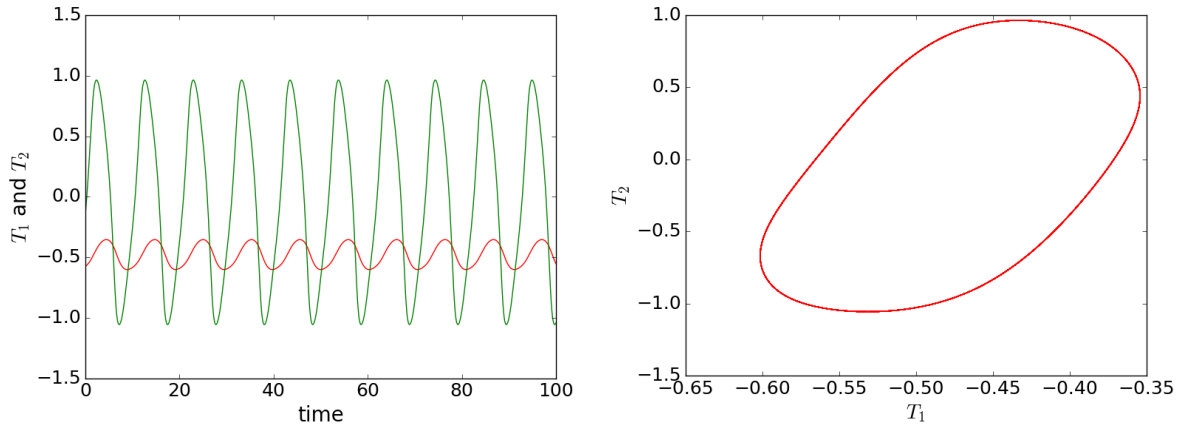


Figure 2.11: Time evolution of the temperature anomalies of the two sub-regions, with self-delay $\delta_1 = 0$ in region 1 and $\delta_2 = 2$ in region 2. The inter-region coupling strength is $\gamma = 0.1$ and self-delay coupling strength is $\alpha = 0.75$. The temperature anomaly of region 1, $T_1$, is shown in red and for region 2, $T_2$ is shown in green.

When the self-delays are different, with $\delta_1 \neq \delta_2$, complex oscillatory patterns arise. These complex patterns are also qualitatively similar to the actual observations of the ENSO phenomenon. Representative examples of these are shown in Fig. 2.10.
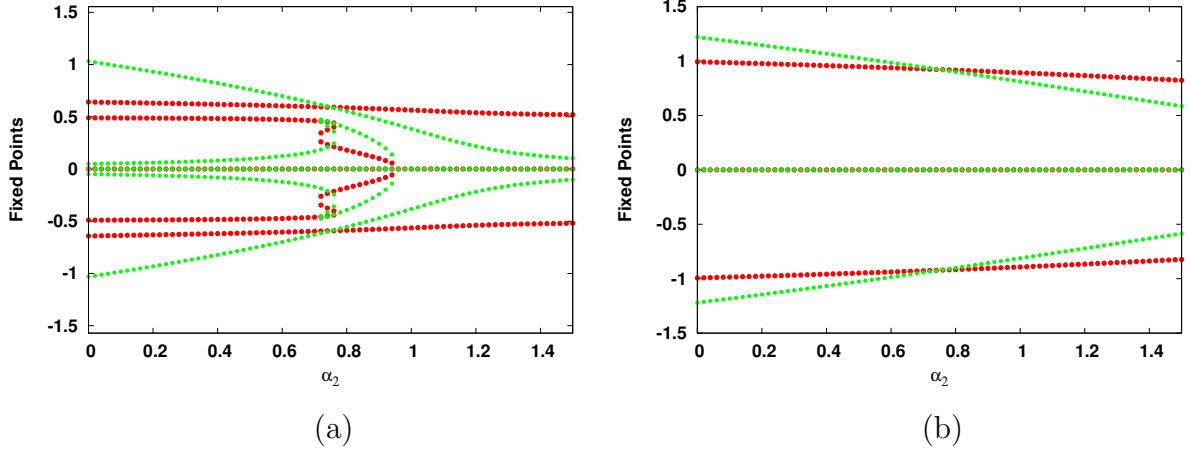
Figure 2.12: Fixed point solutions of $T_1$ and $T_2$ arising from Eqn. 2.4 (red for region 1 and green for region 2) versus strength of the self-delay coupling $\alpha_2$ of region 2, with $\alpha_1 = 0.75$, and inter-region coupling $\gamma$ equal to 0.1 (a) and 0.6 (b).

*Analysis:* We find a richer pattern of fixed point solutions for the heterogeneous case (cf. Fig. 2.12), as compared to the homogeneous case (cf. Fig. 2.6), as the solutions $T_1$ and $T_2$ may now be different. For weak inter-region coupling, such as $\gamma = 0.1$, $T_1$ has 5 fixed points for $0 \leq \alpha_2 \leq 0.7$, of which 2 are stable nodes, 2 are saddle points and 1 is an unstable node. For $0.7 < \alpha_2 < 0.78$ we obtain 9 fixed points, of which 4 are stable nodes, 4 are saddle points and 1 is an unstable nodes. For $T_2$ again we get 5 fixed points for $0.78 \leq \alpha_2 \leq 0.94$, of which 2 are stable nodes, 2 are saddle points and 1 is an unstable node, and for $0.94 < \alpha \leq 1.5$ we get 3 fixed points in which 2 are stable node and 1 is saddle node. The fixed points have different values in the two regions, except for the unstable node. For strong inter-region coupling, such as $\gamma = 0.6$, we get 3 fixed points for $T_1$ and $T_2$, of which 2 are stable nodes and 1 is a saddle. In this case too the stable nodes have different values in the two regions, while the saddle points occur at the same value.

We estimate the basin stability for the fixed point state, by finding the fraction of initial conditions that evolve to fixed points. If this fraction is one, the fixed point state is the global attractor of the dynamics. When this fraction is zero, none of the sampled initial conditions evolve to fixed points, and the system goes to an oscillatory state instead. When the fraction is larger than zero and less than one, we have co-existence of attractors (namely certain initial conditions evolve to fixed points, while others yield oscillations). The basin stability, as a function of $\alpha_2$, keeping $\alpha_1$ fixed, is displayed in Fig. 2.13, for different values of inter-region coupling strengths. It is clearly seen that the region of co-existence of fixed points and oscillations is narrower for lower inter-region coupling,

29

and wider for higher inter-region coupling strengths. Thus it is a evident that strong inter-region coupling $\gamma$ favours larger parameter regions of oscillation suppression, and also yields a larger parameter range where fixed points states co-exist with oscillatory states.
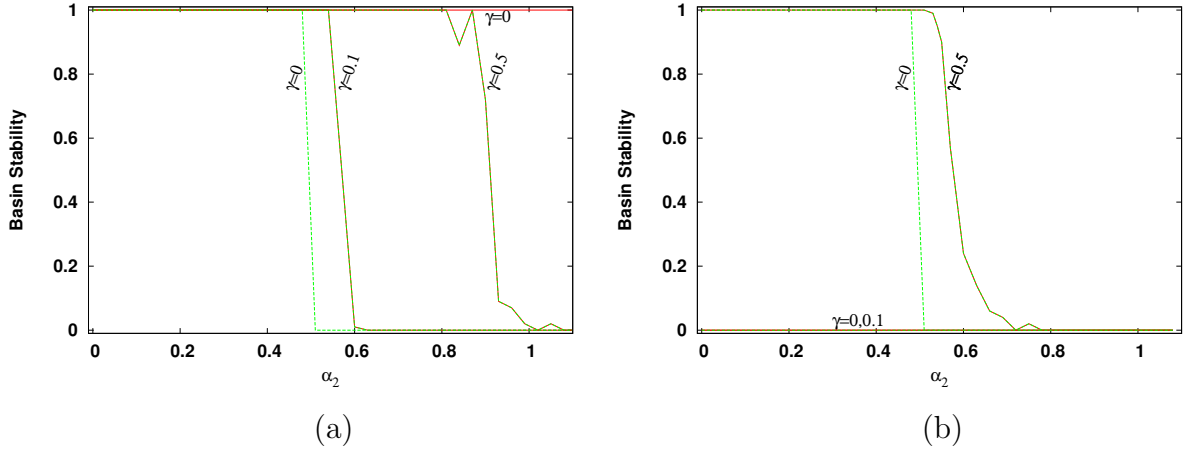


Figure 2.13: Basin Stability of the fixed point state (estimated by the fraction of initial states that evolve to a steady state), as a function of $\alpha_2$. The red color represents region 1 and green color represents region 2. Here delay $\delta = 4$, and inter-coupling strength $\gamma = 0$, 0.1 and 0.5 in Eqn. 2.3, for (a) $\alpha_1 = 0$ and (b) $\alpha_1 = 0.75$.

## 2.6    Basins of attraction of the different emergent dynamical states

The basin of attraction of a dynamical state is the set of points in the space of the system variables, such that if the initial conditions are chosen in this set, the system will evolve to that particular state. In our model we have observed many different dynamical attractors, ranging from fixed points to low-amplitude and high amplitude oscillations. The number of co-existing attractors and their basins of attraction depend crucially upon the self delay, delay and inter-region coupling strengths. So the estimation of the basins of attraction of the different states is important here, as it indicates the prevalence of the state in general and the probability of observing the state given a window of initial conditions. We present below representative cases of the different emergent states and their basins of attraction, for the case of coupled identical sub-regions, as well as coupled non-identical sub-regions.

We first examine the case of coupled identical sub-regions. Specifically we present the case of delays $\delta_1 = \delta_2 = 1$, for different inter-region coupling strengths $\gamma$. When the
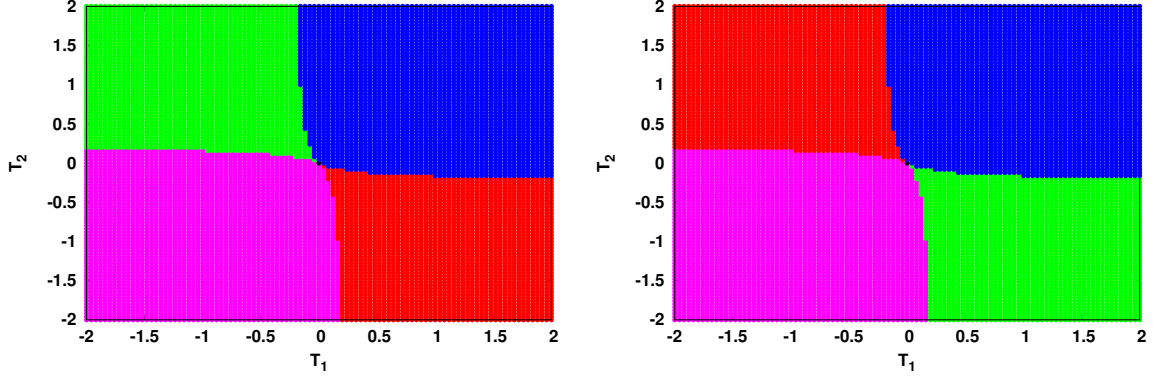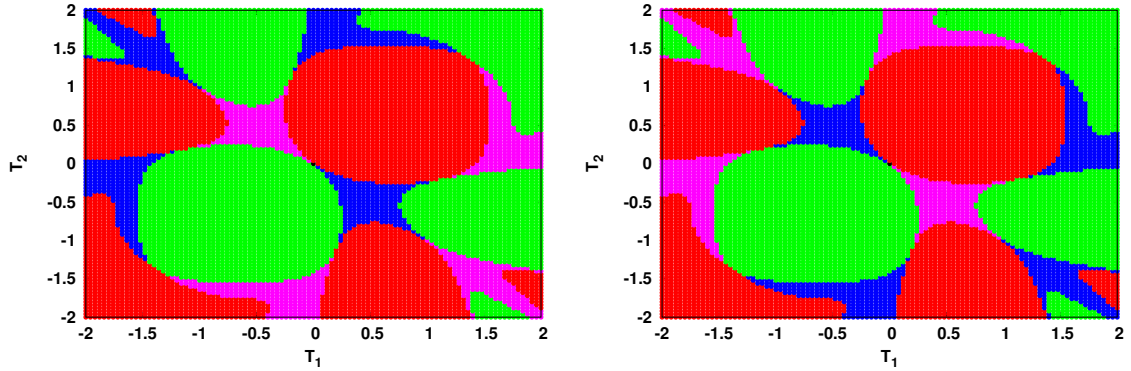
Figure 2.14: Basins of attraction of the different dynamical attractors, in the space of scaled temperature anomalies $T_1$ and $T_2$. Here the green, red, magenta and blue colors represent the basins of attraction of fixed point attractors. The system parameters are $\delta_1 = \delta_2 = \delta = 1, \gamma = 0.1$ and (a) $\alpha_1 = \alpha_2 = 0.5$ and (b) $\alpha_1 = \alpha_2 = \alpha = 0.75$. The left panel is for sub-region 1 and the right panel shows sub-region 2.

inter-region coupling is weak, for instance the case of $\gamma = 0.1$ displayed in Fig. 2.14, both sub-regions have four distinct steady states. For the case of $\alpha_1 = \alpha_2 = 0.5$ (Fig. 2.14a), when the initial values of the sub-regions are both positive or both negative, then both sub-regions approach the same steady state. However, when the initial states are different, namely one region is positive and the other negative, then they approach different steady states, i.e. one positive and one negative steady state. So two dynamical attractors have the same basins of attraction in the sub-regions, while the other two attractors have different basins of attraction, with the basins of the two states being switched. Similarly for the case of $\alpha_1 = \alpha_2 = 0.75$ (Fig. 2.14b), we find that two of the fixed-point attractors have same basin of attraction in $T_1 - T_2$ space in the two sub-systems, while the basins of attraction of the other two fixed-point attractors is switched in the two sub-systems.

31

(a)



(b)



(c)

Figure 2.15: Basins of attraction of the different dynamical attractors, in the space of scaled temperature anomalies $T_1$ and $T_2$. Here the yellow, light blue, magenta, blue and black and orange colors represent the basins of attraction of a fixed point attractor. The system parameters are $\alpha_1 = \alpha_2 = \alpha = 0.75, \delta_1 = \delta_2 = \delta = 1$, and (a) $\gamma = 0.2$, (b) $\gamma = 0.3$ and (c) $\gamma = 0.7$. The left panel is for sub-region 1 and the right panel shows sub-region 2.

Interestingly, now the fixed-point attractors which have same basin of attraction in both sub-regions, have larger basin volume as compared to the two attractors that have different basins of attraction in the sub-systems.



Figure 2.16: Basins of attraction of the different dynamical attractors, in the space of scaled temperature anomalies $T_1$ and $T_2$. Here the green and red colors represent the basins of attraction of fixed point attractors. The system parameters are: $\alpha_1 = \alpha_2 = \alpha = 0.5, \delta_1 = \delta_2 = \delta = 4, \gamma = 0.1$. The left panel is for sub-region 1 and the right panel shows sub-region 2.



Figure 2.17: Basins of attraction of the different dynamical attractors, in the space of scaled temperature anomalies $T_1$ and $T_2$. Here the green, red, magenta and blue colors represent the basins of attraction of fixed point attractors. The system parameters are: $\alpha_1 = 0.75, \alpha_2 = 0.5, \delta_1 = \delta_2 = \delta = 1, \gamma = 0.1$. The left panel is for sub-region 1 and the right panel shows sub-region 2.

When $\gamma \geq 0.2$ (cf. Fig. 2.15) we obtain two steady states, one of which is a positive fixed point and the other a negative fixed point. The positive fixed point state is bounded entirely in a window of positive values (as represented by the light blue, blue and black colors) and negative fixed point state is bounded entirely in a window of negative values (as represented by the yellow, magenta and orange colors). The specific values of the fixed

points depend on the values of the inter-region coupling strength $\gamma$. For a particular value of $\gamma$, the basin of attraction for each attractor is same in both sub-systems and we observe an inversion symmetry of the attractors along the diagonal.

Further, for large delays, for instance the case of $\delta_1 = \delta_2 = 4$ displayed in Fig. 2.16, it is clear that the sub-regions yield two attractors of the same type, with the same basins of attraction in the sub-regions. However, *as the delay increases, the basin boundaries become very complex.*
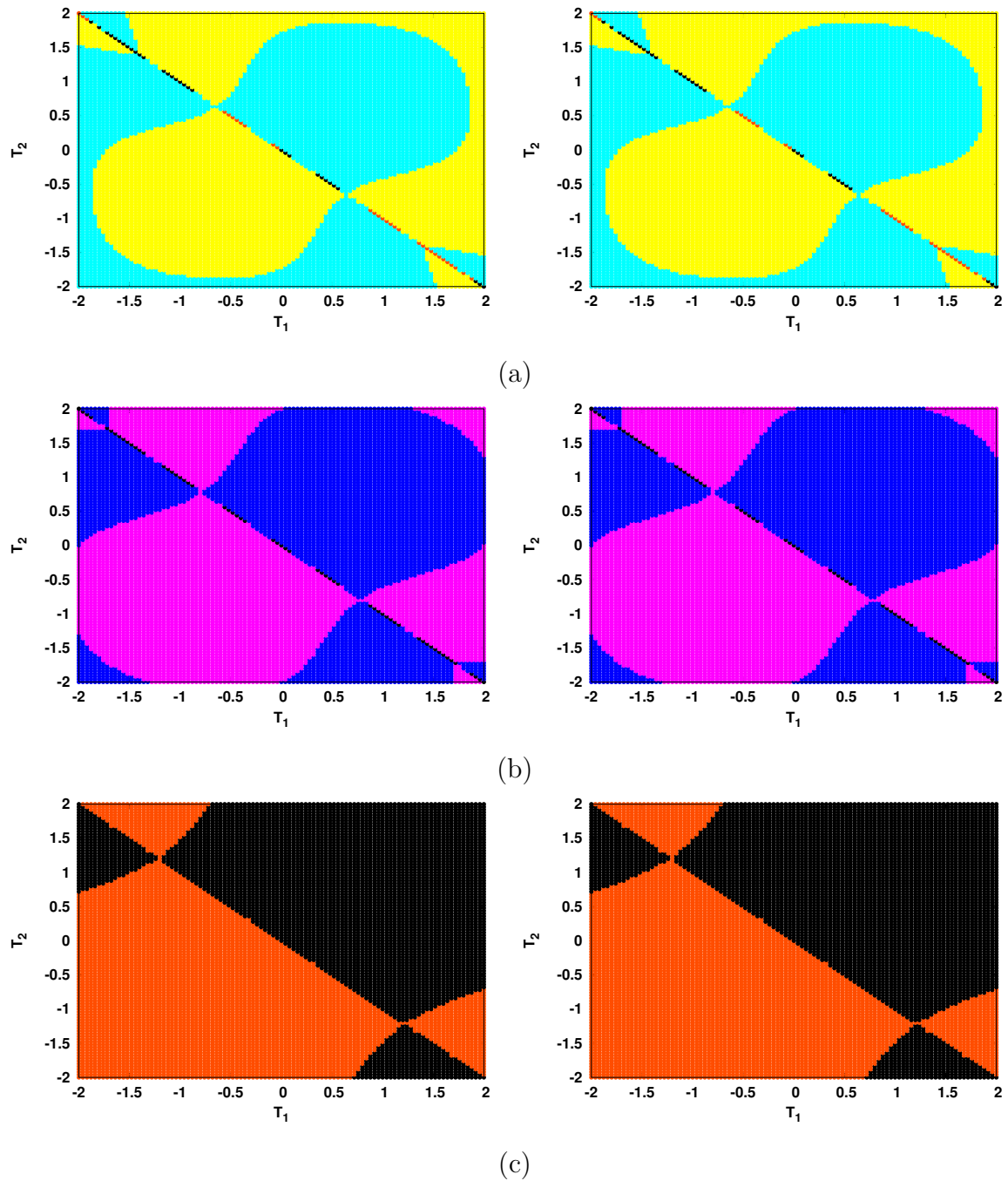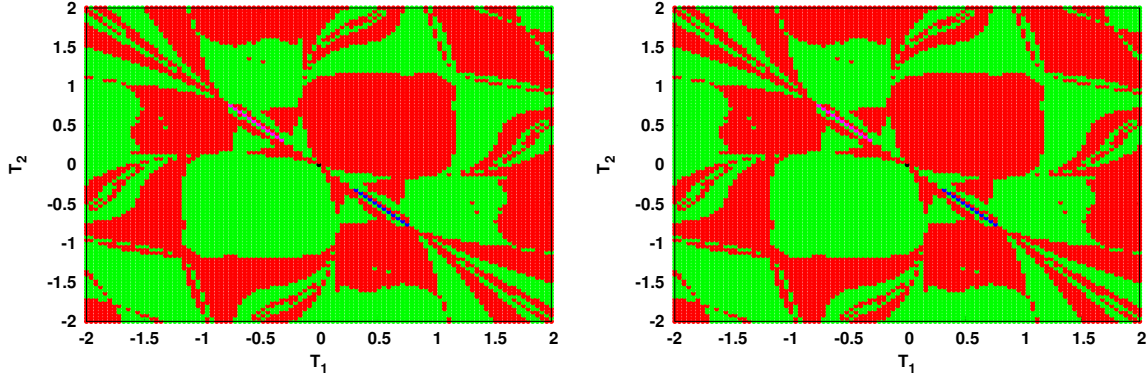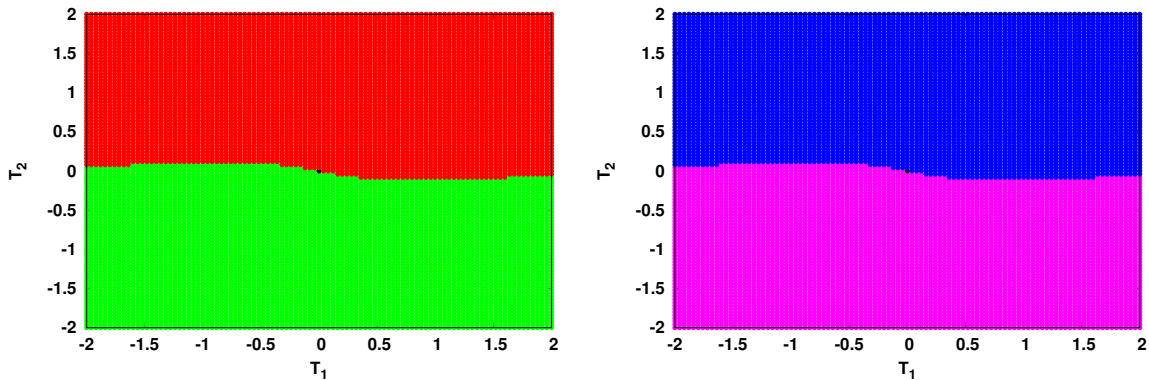


(a)



(b)
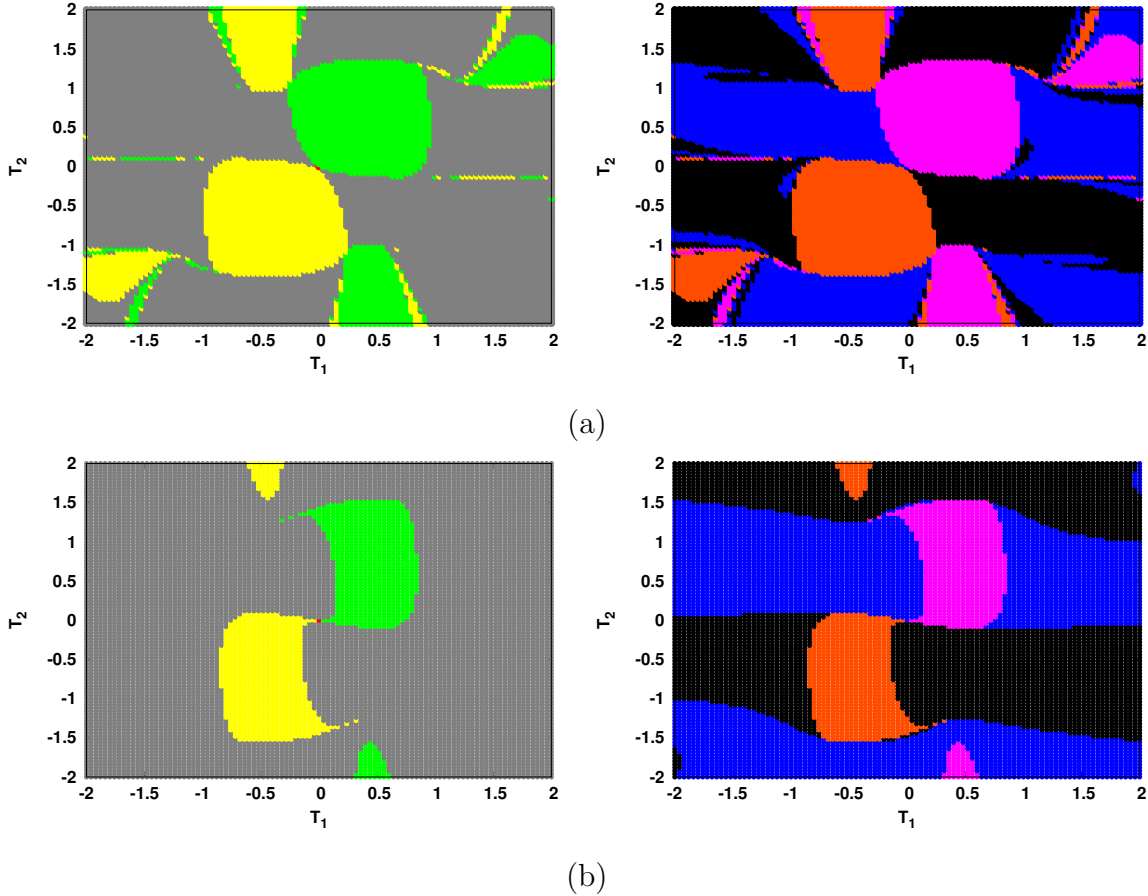
Figure 2.18: Basins of attraction of the different dynamical attractors, in the space of scaled temperature anomalies $T_1$ and $T_2$. Here the green, yellow, magenta and orange colors represent the basins of attraction of fixed point attractors. The black and blue colors represent the basins of attraction of low amplitude oscillations. For the blue color, the minimum and maximum values of the oscillations are positive and for the black color the minimum and maximum values of the oscillations are negative. The gray color represents large amplitude oscillations, with positive value of maxima and negative value of minima. The system parameters are: (a) $\alpha_1 = 0.65, \alpha_2 = 0.5, \delta_1 = \delta_2 = \delta = 2.5, \gamma = 0.1$; (b) $\alpha_1 = 0.75, \alpha_2 = 0.5, \delta_1 = \delta_2 = \delta = 2, \gamma = 0.1$. The left panel is for sub-region 1 and the right panel shows sub-region 2.

Next we consider the case of coupled non-identical systems. For instance, we display

an illustrative example of a system with parameters $\alpha_1 = 0.75$, $\alpha_2 = 0.5$, $\gamma = 0.1$ and $\delta = 1$ in Fig. 2.17. Here we observe two types of attractors, and these attractors are different in the two sub-regions due to the difference in the value of the self-delay coupling strengths. Specifically, for small delays the dynamical attractors are fixed points, and the values of these fixed points are dependent on the values of the parameters. As the delay increases we observe coexistence of fixed points and oscillatory attractors (cf. Fig. 2.18a-b).

From the case of $\alpha_1 = 0.75, \alpha_2 = 0.5, \delta = 2, \gamma = 0.1$, displayed in Fig. 2.18b, we observe that there are three types of attractors for the system when the strength of self delay is high. Two of these attractors are fixed points (represented by green and yellow colors) and one is an oscillatory attractor with high amplitude (represented by the gray color). Systems with weak self-delay strength have four types of attractors, two of which are fixed points (represented by magenta and orange color) and two are low-amplitude oscillatory attractors, that are entirely positive-valued or negative-valued. We also observe that for large delay as strength of self-delay increases, the volume of the basin of attraction of the fixed point attractors decreases.

## 2.7 Robustness of the dynamical attractors under noise

If the system is attracted to a dynamical state, even under the influence of noise, then the state can be considered robust under noise. In order to examine this, we examine the system described by Eqn. 2.3, under Gaussian noise:

$$\frac{dT_1}{dt} = T_1 - T_1^3 - \alpha_1 T_1(t - \delta_1) + \gamma T_2 + D\eta(t) \tag{2.5}$$
$$\frac{dT_2}{dt} = T_2 - T_2^3 - \alpha_2 T_2(t - \delta_2) + \gamma T_1 + D\eta(t)$$

where $\eta$ is a delta-correlated Gaussian noise and $D$ is the strength of the noise. Here both sub-systems experience the same noise.

Figure 2.19: Temporal evolution of $T_1$ and $T_2$, for system parameters $\alpha_1 = \alpha_2 = \alpha = 0.75, \delta_1 = \delta_2 = \delta = 1, \gamma = 0.1$ and initial condition $T_1 = T_2 = 0.5$. Here the noise strength is (a) $D = 0$ (namely without noise), (b) $D = 0.01$, (c) $D = 0.05$ and (d) $D = 0.1$.

First, consider a system with identical strengths of self-delay $\alpha_1 = \alpha_2 = 0.75$, delay $\delta_1 = \delta_2 = \delta = 1$ and inter-region coupling $\gamma = 0.1$, where there are four fixed point solutions for the noise-free system: $0.591608, -0.591608, 0.38729$ and $-0.38729$. Now to check the robustness of the different fixed points, we add noise to the system, and follow the evolution of the noisy system from different initial values of $T_1$ and $T_2$. Specifically, in Fig. 2.19, the initial values of $T_1$ and $T_2$ is 0.5. Without noise both sub-systems go to the fixed point at 0.591608 (cf. Fig. 2.19a). Under weak perturbations this fixed point is still attractive, with the noisy system confined around the fixed point at 0.591608 for low noise strengths (cf. Fig. 2.19b-c). However, interestingly, when the noise strength is high, the system *switches between the two states* around 0.591608 and $-0.591608$ (cf. Fig. 2.19d). The system does not wander to the other two fixed points at 0.38729 and $-0.38729$ at all, but only jumps randomly between two bands around 0.591608 and $-0.591608$.

36

Similarly, for the same system evolving from initial condition $T_1 = 0.5, T_2 = -0.5$, it is evident from Fig. 2.20 that each sub-system goes to different states 0.38729 and $-0.38729$ when there is no noise (cf. Fig.2.20a). However, when noise strength is low (e.g. $D = 0.01, 0.05$), the noisy system goes to either a state around 0.591608 or around $-0.591608$, with both sub-systems now approaching the same state (cf. Fig.2.20b-c). So even under weak noise the system evolves away from the fixed points 0.38729 and $-0.38729$, and is attracted to states around the fixed points at 0.591608 and $-0.591608$. When noise strength is high, again there is *switching* between these states (cf. Fig.2.20d). Thus Figs. 2.19-2.20 suggest that the fixed points 0.591608 and $-0.591608$ are more robust to noise than the other two fixed points.
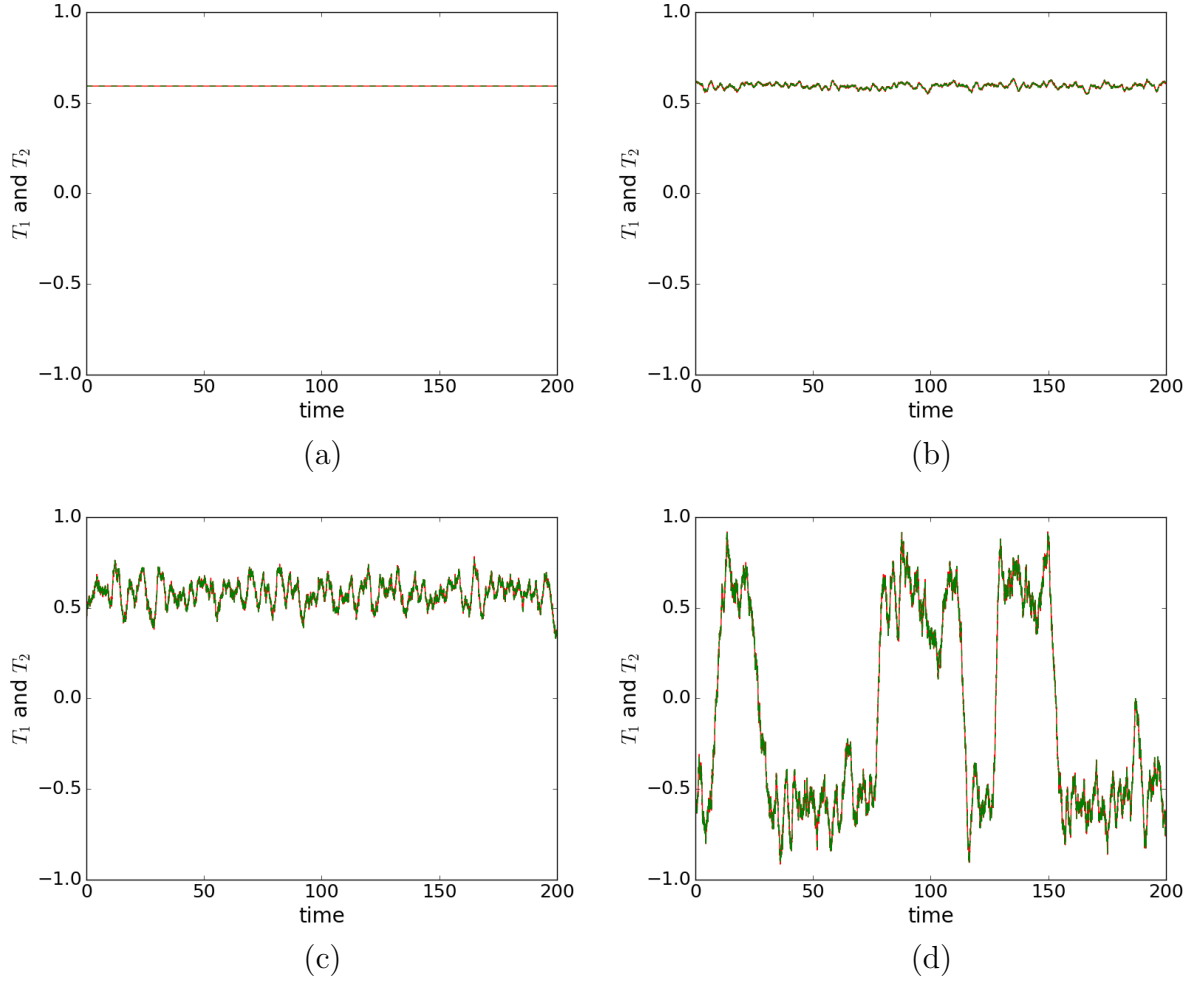


Figure 2.20: Temporal evolution of $T_1$ and $T_2$, for system parameters $\alpha_1 = \alpha_2 = \alpha = 0.75, \delta_1 = \delta_2 = \delta = 1, \gamma = 0.1$ and initial condition $T_1 = 0.5, T_2 = -0.5$. Here the noise strength is (a) $D = 0$ (namely without noise), (b) $D = 0.01$, (c) $D = 0.05$ and (d) $D = 0.1$.

We now go on to consider another parameter set, $\alpha_1 = \alpha_2 = \alpha = 0.5, \delta_1 = \delta_2 = \delta = 1, \gamma = 0.1$, which yields four steady states: $0.774597, -0.774597, 0.632456$ and $-0.632456$. From initial conditions $T_1 = T_2 = 0.5$, both sub-systems go to the fixed point at $0.774597$ in the noise-free case (cf. Fig. 2.21a). Under influence of weak and high noise (e.g. $D = 0.01, 0.1$), the sub-systems are still attracted to the same state, as evident from Fig. 2.21b-c. When noise strength is very high (e.g. $D = 0.2$), there is *switching* between $0.774597$ and $-0.774597$ states (cf. Fig. 2.21d). Thus we can infer that these states are more stable compared to the other two states.



Figure 2.21: Temporal evolution of $T_1$ and $T_2$, for system parameters $\alpha_1 = \alpha_2 = \alpha = 0.5, \delta_1 = \delta_2 = \delta = 1, \gamma = 0.1$ and initial condition $T_1 = T_2 = 0.5$. Here the noise strength is (a) $D = 0$ (namely without noise), (b) $D = 0.01$, (c) $D = 0.1$ and (d) $D = 0.2$.

On examining the initial condition $T_1 = 1.5$ and $T_2 = -1.5$, we observe from Fig. 2.22(a-b) that when there is no noise or when noise strengths are very weak (e.g. $D = 0.01$), each sub-region goes to a different state, namely the sub-regions are attracted to either

0.632456 or −0.632456. For stronger noise (e.g. $D = 0.1$) the system evolves to same state, namely both sub-regions evolve to states close to either 0.632456 or −0.632456 (cf. Fig. 2.22c). When noise strength is very high (e.g. $D = 0.2$), there is *switching* between 0.632456 and −0.632456 states (cf. Fig. 2.22d). Therefore we conclude from Figs. 2.21-2.22 that there are four attracting states when the system is under the influence of noise. Here we observe four robust states for $\alpha_1 = \alpha_2 = \alpha = 0.5$, and only two robust states for $\alpha_1 = \alpha_2 = \alpha = 0.75$. We also observe that for lower values of $\alpha_{1,2}$, larger noise strengths are required to switch between these states.
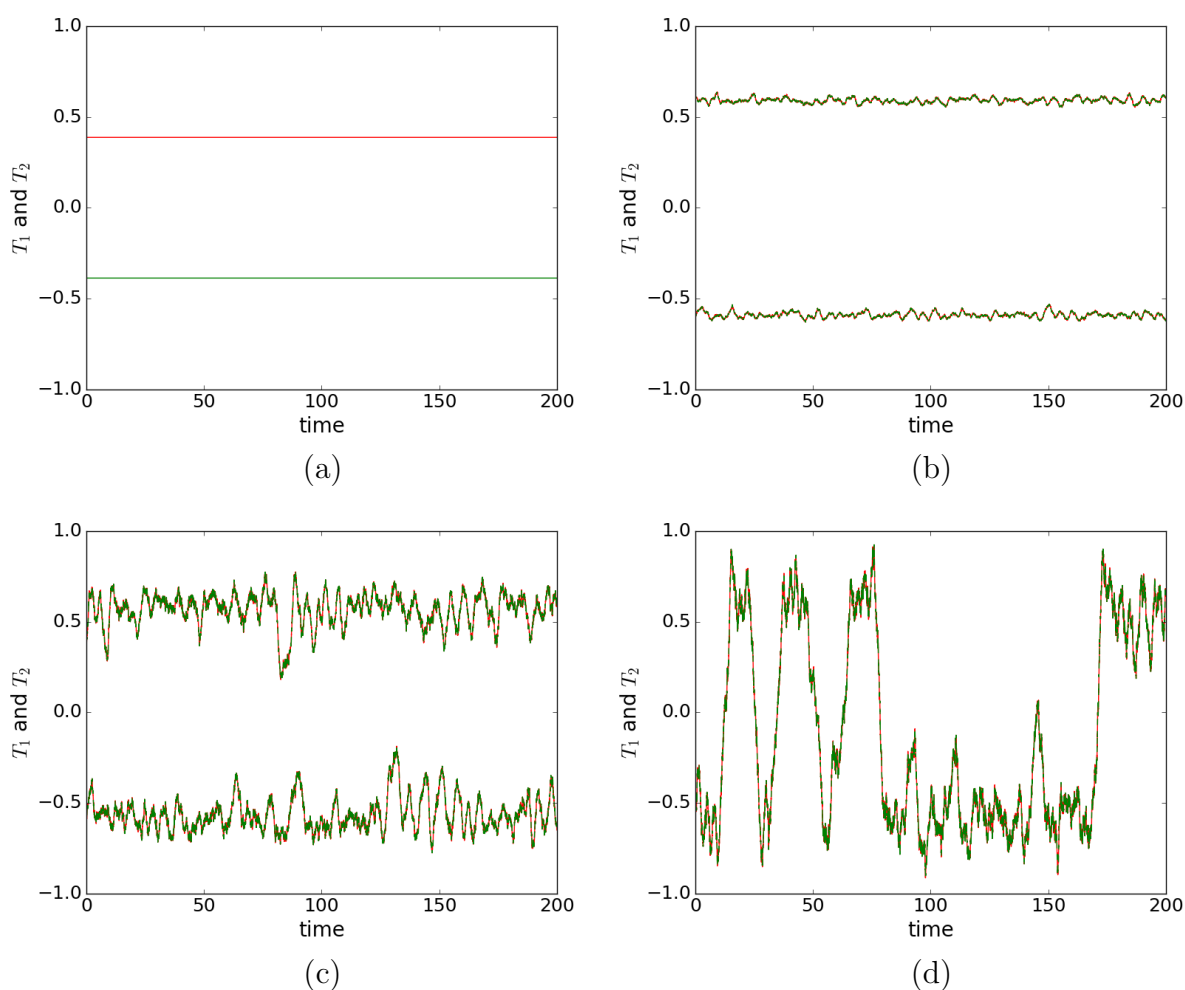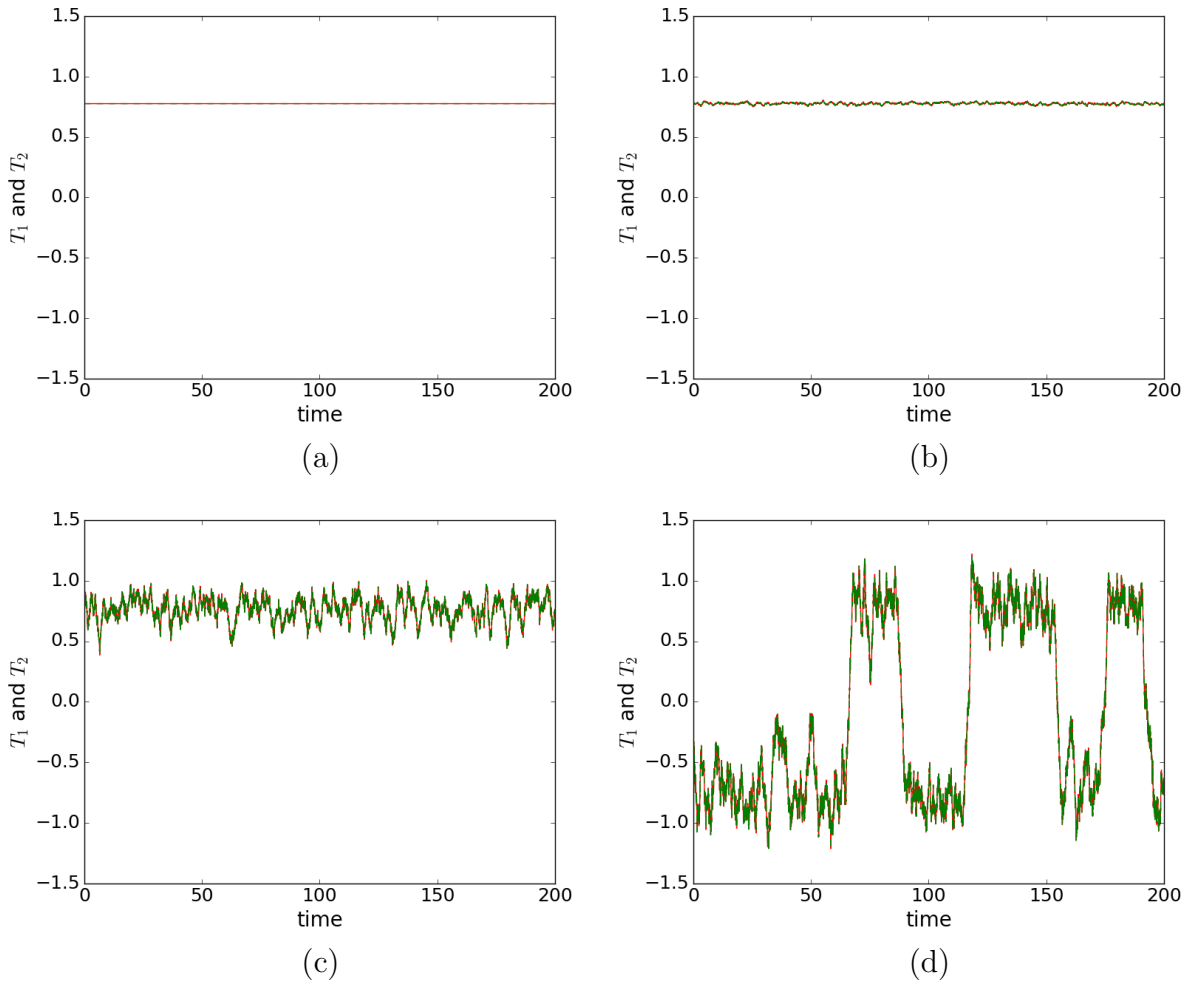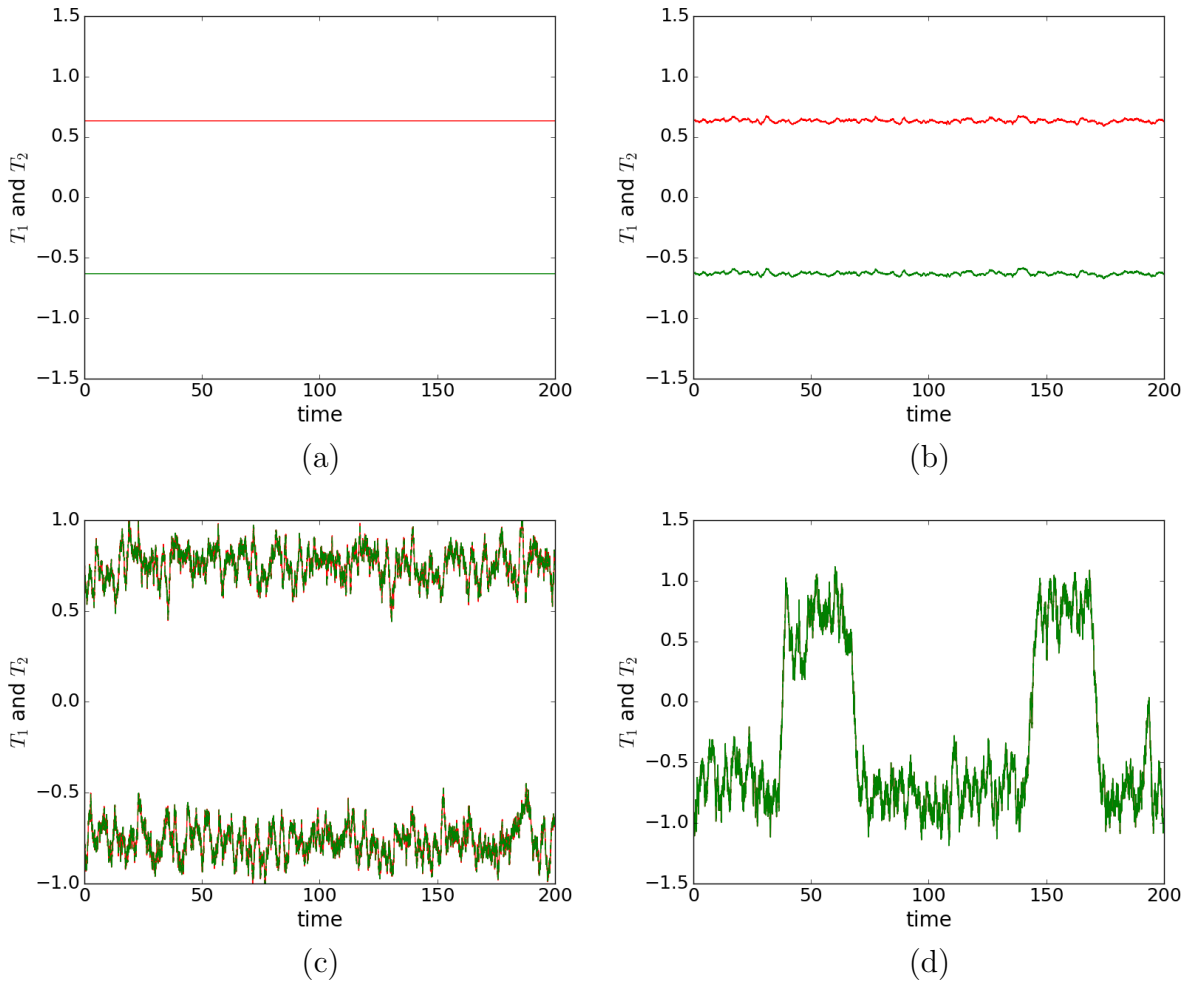


Figure 2.22: Temporal evolution of $T_1$ and $T_2$, for system parameters $\alpha_1 = \alpha_2 = \alpha = 0.5, \delta_1 = \delta_2 = \delta = 1, \gamma = 0.1$ and initial condition $T_1 = 1.5, T_2 = -1.5$. Here the noise strength is (a) $D = 0$ (namely without noise), (b) $D = 0.01$, (c) $D = 0.1$ and (d) $D = 0.2$.

## 2.8   Discussions

We have considered a system of coupled delayed action oscillators modelling the El Niño effect, and studied the dynamics of the sea surface temperature (SST) anomaly. The existence and stability of the solutions arising in this model depend on three parameters: self delay, delay and inter-region coupling strengths. In our work we explore the dynamics in the space of these parameters. The emergence or suppression of oscillations in our models is a dynamical feature of utmost relevance, as it signals the presence or absence of ENSO-like oscillations. Note that in contrast to the well-known low order model of ENSO, the recharge oscillator [30] and its important stochastic extensions [31], where the influence of the neighbouring regions on the region of interest is modelled as external noise, we consider neighbouring regions as a coupled deterministic dynamical systems. Different parameters yield a rich variety of dynamical patterns in our model, ranging from steady states and homogeneous oscillations to irregular oscillations, without explicit inclusion of noise.

For identical sub-regions one typically observes a co-existence of amplitude and oscillator death behavior for low delays, and heterogeneous oscillations for high delays, when inter-region coupling is weak. For moderate inter-region coupling strengths one obtains homogeneous oscillations for sufficiently large delays and amplitude death for small delays. When the inter-region coupling strength is large, oscillations are suppressed altogether, implying that strongly coupled sub-regions do not yield ENSO-like oscillations. Further we observe that larger strengths of self-delay coupling favours oscillations, while oscillations die out when the delayed coupling is weak. This indicates again that delayed feedback, incorporating oceanic wave transit effects, is the principal cause of oscillatory behaviour. So the effect of trapped ocean waves propagating in a basin with closed boundaries is crucial for the emergence of ENSO-like oscillations. The non-uniformity in delays, and difference in the strengths of the self-delay coupling of the sub-regions, is also investigated. As in the uniform case, larger delays and self-delay coupling strengths lead to oscillations, while strong inter-region coupling kills oscillatory behaviour. The difference between the uniform case and the non-uniform system, is that amplitude death and homogeneous oscillations are predominant in the former, while oscillator death and heterogeneous oscillations are commonly found in the latter. Interestingly, we also find that when one sub-region has low delay and another has high delay, under weak coupling the oscillatory sub-region induced oscillations in sub-region that would have gone to a steady state if uncoupled.

Moreover, we have also explored the robustness of the different dynamical states under noisy evolution, in order to gauge which set of attractors are typically expected to arise when the system evolves under the influence of external perturbations. Typically we find that the noisy system evolves to a sub-set of the attractors found in the deterministic system, and those attractors can be considered robust under noise. Often when noise is very weak, the system is attracted to states close to the noise-free case. However when noise is stronger, the system switches randomly between the attractors. Using this method of gauging the robustness of the different attractors in our multi-stable system, we find that lower strength of self-delay coupling yields a larger number of robust states, than stronger self-delay coupling. Further, larger noise strengths are required to switch between these states, when the strength of self-delay coupling is low.

We then investigate the basins of attraction of the different dynamical attractors arising in our model. Typically, the number of distinct attractors and their basins of attraction depend upon the values of parameters. For instance, when $\alpha_1 = \alpha_2 = 0.75, \delta = 1$, we find four steady states for $\gamma = 0.1$ and two steady states for $\gamma \geq 0.2$. The value of the fixed points depend on the values of the inter-region coupling strength $\gamma$. For the typical case of $\alpha_1 \neq \alpha_2$, each sub-region has two fixed points and two oscillator states, with the attractors being different in the two regions. Further, generically, in such cases there is a complex co-existence of attractors.

Now, several agencies such as the National Oceanic and Atmospheric Administration (NOAA) in the United States, monitor the sea surface temperatures in various regions, five degrees of latitude on either side of the equator, with Niño 1-2 region located in the band 80W–90W, Niño 3 region in 90W–150W, and Niño 4 region in 160E–150W. The Niño 3.4 region (120W–170W) is often the primary focus for monitoring and predicting El Niño. When the three-month SST average for the area is more than 0.5°C above (or below) normal for that period, then an El Niño (or La Niña) is considered to be in progress.

How our model can explain the 0.5°C criterion used for the forecasting, we show by rescaling our result and comparing it with observations. We consider two regions along the equator, where the first region extends from 90° West to 150° West (Niño 3 region) with the mid-point being 120° West and the second region extends from 150° West to 160° East (Niño 4 region) with the mid-point being 175° West. The western Pacific boundary is at 120° East. This gives angular separation of 120° and 65° of longitude for the waves to travel, for the two regions respectively, and corresponds to a distance $120(2\pi/360) \times r_{Earth} = 13.35 \times 10^6 m$ and $65(2\pi/360) \times r_{Earth} = 7.23 \times 10^6 m$ for the two

regions, where $r_{Earth} = 6.37 \times 10^6 m$. Speed of the Kelvin wave is $1.4 \text{ms}^{-1}$ and $0.47 \text{ms}^{-1}$ for Rossby wave [27]. These values of speed gives $13.35 \times 10^6 m / 0.47 ms^{-1} = 329$ days for the Rossby propagation to the western boundary, and a further $13.35 \times 10^6 m / 1.4 ms^{-1} = 110$ days for the return of the Kelvin waves, thus total delay of transient time $\Delta = 439$ days for the first region. For the second region it gives $7.23 \times 10^6 m / 0.47 ms^{-1} = 178$ days for the Rossby propagation to the western boundary, and a further $7.23 \times 10^6 m / 1.4 ms^{-1} = 59$ days for the return of the Kelvin waves, thus total delay of transient time $\Delta = 237$ days.

For the first region (Niño 3 region) maximum anomaly temperature ($T_1$) is on average $2.11°C$ and for the second region (Niño 4 region) maximum anomaly temperature ($T_2$) is on average $1.15°C$ (these values we have received from the data produced by NOAA [32, 33]). Parameter set $\alpha_1 = 0.75$, $\alpha_2 = 0.5$, $\gamma = 0.1$ and $\delta = 2$, allow us to calculate $k_1 = 1.64$/years, $k_2 = 3.03$/years, $b_1 = 0.43°C^{-2}$/years and $b_2 = 1.66°C^{-2}$/years. So, now if we consider the $0.5°C$ criterion used for the forecasting as $T_1 = 0.5°C$ and $T_2 = 0.5°C$, then after rescaling, equivalents to the dimensionless temperatures in two regions in the model are $T_1' = 0.256$ and $T_2' = 0.37$. Thus, we can find the the criterion location on the diagram of basins of attraction in Fig. 2.18(b)(left). It belongs to the green basin which corresponds to the El Niño state, in the vicinity of the boundary with the gray basin associated with oscillation between El Niño and La Niña states. Hence, the model can reproduce the $0.5°C$ criterion revealed from observations.

Additionally, our modelling result suggests that instead of the single value criterion (as $0.5°C$), an interval should be used as criterion to estimate the El Niño or La Niña progress. According to the model result, if temperature anomaly of $T_1$ is in the range $0.5°C < T_1 < 1.6°C$ (corresponding $0.32 < T_1' < 0.84$) and $T_2$ is in the range $-0.06°C < T_2 < 2°C$ (corresponding $-0.04 < T_2' < 1.52$),then El Niño is considered to be in progress. If temperature anomaly $T_1$ is in the range $-1.6°C < T_1 < -0.5°C$ (corresponding $-0.84 < T_1' < -0.32$) and $T_2$ is in the range $-2°C < T_2 < 0.06°C$ (corresponding $-1.52 < T_2' < 0.04$), then La Niña is considered to be in progress. In other range of temperature anomalies, ENSO(successive El Niño and La Niña) episodes are considered to be in progress.

Hence, the basins of attraction for the different steady states and oscillatory states in our model may help in understanding patterns in the sea surface temperatures anomalies in monitored coupled sub-regions. Further, our mapping of the basins of attraction might be helpful for forecasting of El Niño (or La Niña) progress, as it indicates the combination of initial SST anomalies in the sub-regions that can result in a El Niño/La Niña episodes.

In summary then, we have explored a simple model based on coupled delayed action oscillators modelling the ENSO-like oscillations, and studied the dynamical patterns of the SST anomaly. Specifically we have presented the existence, stability and basins of attraction of the solutions arising in the model system, for different representative parameter sets. Thus our dynamical model may help provide a potential framework in which to understand patterns in the SST anomalies in different coupled sub-regions, which is an important feature that has not yet been sufficiently explored.

# Chapter 3

# Chimera States in Star Networks

## 3.1 Introduction

Chimera states have been extensively studied over the last decade in natural and artificial networks of coupled identical complex systems, in fields ranging from physics and chemistry to biology and engineering. At the outset, it was noticed that in a system of non-locally coupled identical phase oscillators, the system spontaneously broke the underlying symmetry and split into synchronized and desynchronized oscillator groups [34, 35]. Namely, there emerged a state where coherent and incoherent sets of oscillators coexisted. This state was dubbed a chimera state, as it was reminiscent of the greek mythological creature composed of incongruous parts [36]. In recent years chimera states have also been observed experimentally in optical analogs of coupled map lattices [37], BelousovZhabotinsky chemical oscillator systems [38], two populations of mechanical metronomes [39] and modified time-delayed electronic circuit systems [40].

In this chapter, we will show how chimera states also emerge in oscillator networks with a star topology. The star configuration is one where the network has a central hub position and all other nodes are linked to this node. This configuration arises extensively in human-engineered computer networks, where every node connects to a central computer, and the central computer acts as a server and the peripheral devices act as clients. Further, a star-like structure is a primary motif in scale-free networks, which have been reported to arise in large interactive systems ranging from the web-graph of the World Wide Web, to naturally occurring phenomena, such as protein-protein interaction networks [10].

In this chapter we will show the extensive existence of chimeras in the end-nodes of the star network, which are identical in terms of the coupling environment and dynamical equations. We will demonstrate how the symmetry of the end-nodes is broken and coexisting groups with different dynamical behaviors emerge. Further we will provide an estimate of the basin of attraction of the chimera state. Interestingly, we find that such chimera states are very wide-spread in this network topology, and large parameter regimes of coupling strengths typically yield a chimera state.

## 3.2 Model

We study the dynamics of a star network of $N$ identical nonlinear oscillator systems. In such networks there is one central hub node (labelled by site index $i = 0$) and $N - 1$ environmentally identical peripheral end-nodes connected to the central node (labelled

by node index $i = 1, \ldots N - 1$). One can also interpret this system as a set of uncoupled oscillators connected to a common drive. The focus of this study is the dynamical patterns arising in the $N - 1$ identical end-nodes of this network.

Here we consider general dynamical model to study $N$ coupled identical oscillators, which is given by these following nonlinear differential equations:

$$
\begin{aligned}
\dot{x}_i &= f_x(x_i, y_i, z_i) + \sum_{j=0}^{N-1} K_{ij} H(x_i, x_j, y_i, y_j) & (3.1) \\
\dot{y}_i &= f_y(x_i, y_i, z_i) \\
\dot{z}_i &= f_z(x_i, y_i, z_i)
\end{aligned}
$$

Here coupling matrix element for central node $i = 0$ is $K_{0j} = k/2$ when $j \neq 0$, and for the end-nodes $i = 1, \ldots N - 1$, $K_{i0} = k/2$ and zero otherwise. The coupling strength is given by $k$.

In order to establish the generality of our results, we consider three different coupling forms:

- **Conjugate Coupling**
  Conjugates coupling means the coupling function have dissimilar variable as their arguments. This form of coupling is relevant in physical systems such as coupled semiconductor lasers and electronic circuits [41]. This type of coupling also present in natural system for instance cross-predation between population, where each predator can consume the other pray [42].

- **Diffusive Coupling**
  Diffusive coupling namely that the coupling function have similar variable as their arguments. This is the most common important coupling present in many systems for example neurons model, ecosystems etc.

- **Mean-field coupling**
  Mean-field coupling is equivalent to each site evolving diffusively under the influence of a "local mean field" generated by the coupling neighbourhood of each site.

We give below the general dynamical equations for the different coupling forms.

$$H(x_i, x_j, y_i, y_j) = \begin{cases} (x_j - x_i), & \text{Diffusive coupling} \\ (y_j - x_i), & \text{Conjugate coupling} \\ (x_m - x_0), & \text{Mean-field diffusive for hub} \\ (x_0 - x_i), & \text{Mean-field diffusive for end-nodes} \end{cases} \tag{3.2}$$

where $x_m = \frac{1}{N-1} \sum_{j=1,\dots N-1} x_j$ is the mean field of the end-nodes.

We study Rössler and Lorenz chaotic systems, coupled in star network configuration, through the different coupling forms given above. A wide range of coupling strengths, in networks of size ranging from 3 to 100 oscillators is investigated. The principal observations of the patterns arising in these networks, from generic random initial states, are described in following sections. Note that all the synchronization mentioned in this chapter refers to *complete synchronization*, where both amplitude and phase are in synchrony.

### 3.2.1 Dynamical Patterns for Coupled Rössler Oscillators

For the local dynamics at the nodes, we take two prototypical chaotic systems that have widespread relevance in modelling phenomena ranging from lasers to circuits. First we consider the Rössler type oscillator at node $i$, given by the form:

$$\begin{aligned} f_x(x_i, y_i, z_i) &= -[\omega_i + \epsilon(x_i{}^2 + y_i{}^2)]y_i - z_i \\ f_y(x_i, y_i, z_i) &= [\omega_i + \epsilon(x_i{}^2 + y_i{}^2)]x_i + ay_i \\ f_z(x_i, y_i, z_i) &= b + z_i(x_i - c) \end{aligned} \tag{3.3}$$

in Eqn. 3.1. For each node, $\omega_i + \epsilon(x_i{}^2 + y_i{}^2)$ is close to the angular velocity of the $i^{th}$ oscillator, perturbed by amplitude $x_i{}^2 + y_i{}^2$ when $\epsilon \neq 0$. Here we take the parameter values to be: $a = 0.15$, $b = 0.4$, $c = 8.5$, $\omega_1 = \omega_2 = \omega_3 = 0.41$ and $\epsilon = 0.0026$ [41], yielding a chaotic attractor.

Figure 3.1: Space-time plot displaying the evolution of the state $x_i$ of the end-nodes of a star network of conjugately coupled Rössler systems for system size $n = 50$. Here coupling strength $k = 0.01$ (a), $k = 0.25$ (b), $k = 0.35$ (c).

We find that as coupling strength increases, the end-nodes go from a de-synchronized state to a completely synchronized state, via a large coupling parameter regime yielding chimera states. The chimera states are characterized by the co-existence of synchronized and de-synchronized sets of end-nodes, and are distinct from the fully synchronized state, the fully de-synchronized state and the synchronized cluster state.

First we explore the spatiotemporal plots for conjugate, diffusive and mean-field type of coupling for coupled Rössler oscillators in star network with $N = 50$. From Figs. 3.1, 3.2 and 3.3 we can see the collective behaviour of the dynamical systems for typical initial conditions with varying coupling strength. We can see clearly that at low coupling strength: $k = 0.01$ all end-nodes are in de-synchronized state for the conjugate coupling (cf. Fig. 3.1)(a), diffusive coupling (cf. Fig. 3.2(a)) and for mean-field coupling (cf. Fig.
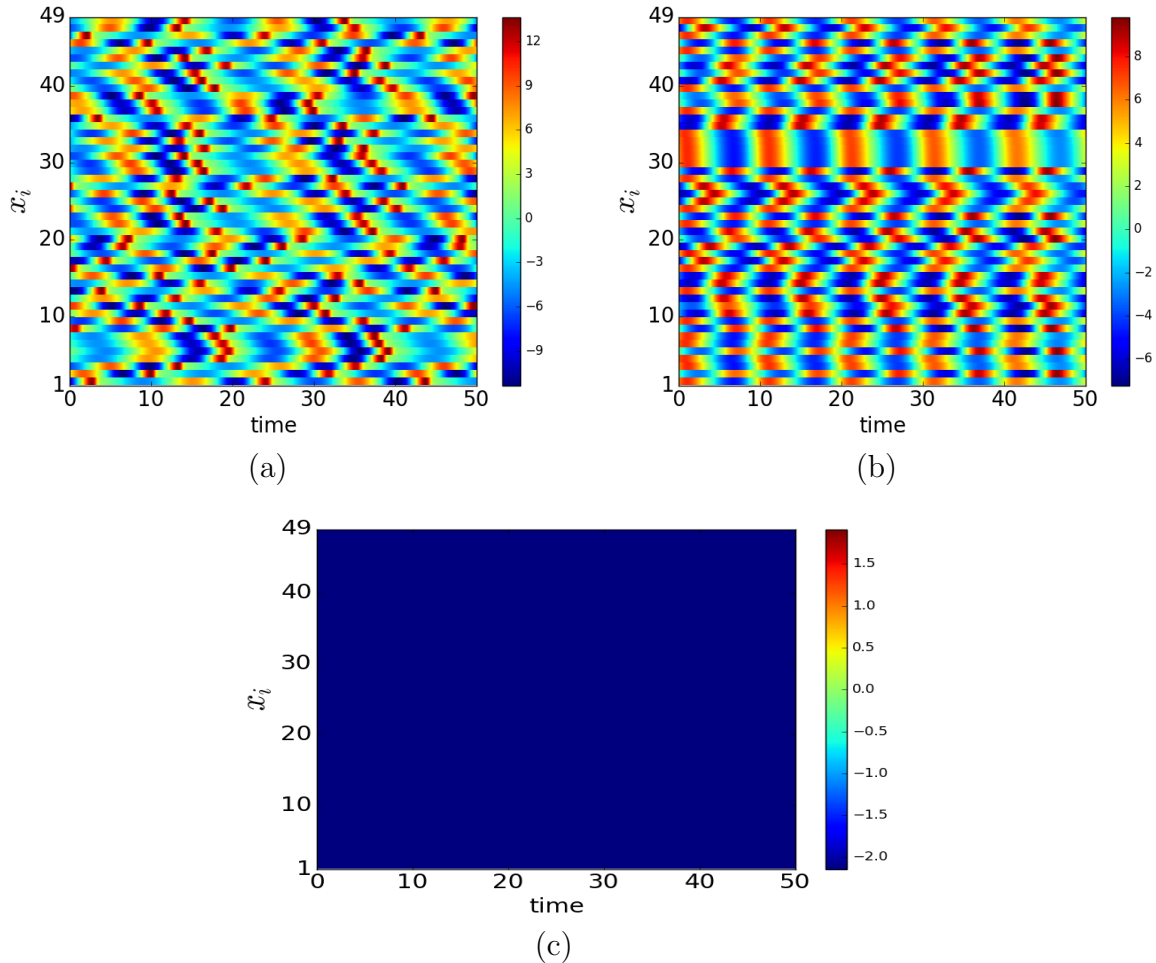
Figure 3.2: Space-time plot displaying the evolution of the state $x_i$ of the end-nodes of a star network of diffusively coupled Rössler systems for system size $n = 50$. Here coupling strength $k = 0.01$ (a), $k = 0.11$ (b), $k = 0.35$ (c), $k = 0.52$ (d).

3.3(a)). All end-nodes are in chimera states for moderate coupling strength: $k = 0.25$ for conjugate coupling (cf. Fig. 3.1)(b), $k = 0.11$ for diffusive coupling (cf. Fig. 3.2(b)) and $k = 0.11$ for mean-field coupling (cf. Fig. 3.3(b)). All end-nodes are in synchronized state at high coupling strength: $k = 0.35$ for conjugate coupling (cf. Fig. 3.1)(c), $k = 0.35$ for diffusive coupling (cf. Fig. 3.2(c)) and $k = 0.25$ for mean-field coupling (cf. Fig. 3.3(c)). In conjugate coupling the synchronized state is amplitude death state, but in diffusive and mean-field coupling the end-nodes go from oscillatory synchronized state to amplitude death synchronized state (cf. Figs. 3.2, 3.3).

A representative example of a chimera state, obtained from a typical random initial condition, in a diffusively coupled star network is displayed in Fig. 3.4. In the example, the identical end-nodes split into a synchronized set and a set of nodes that are not
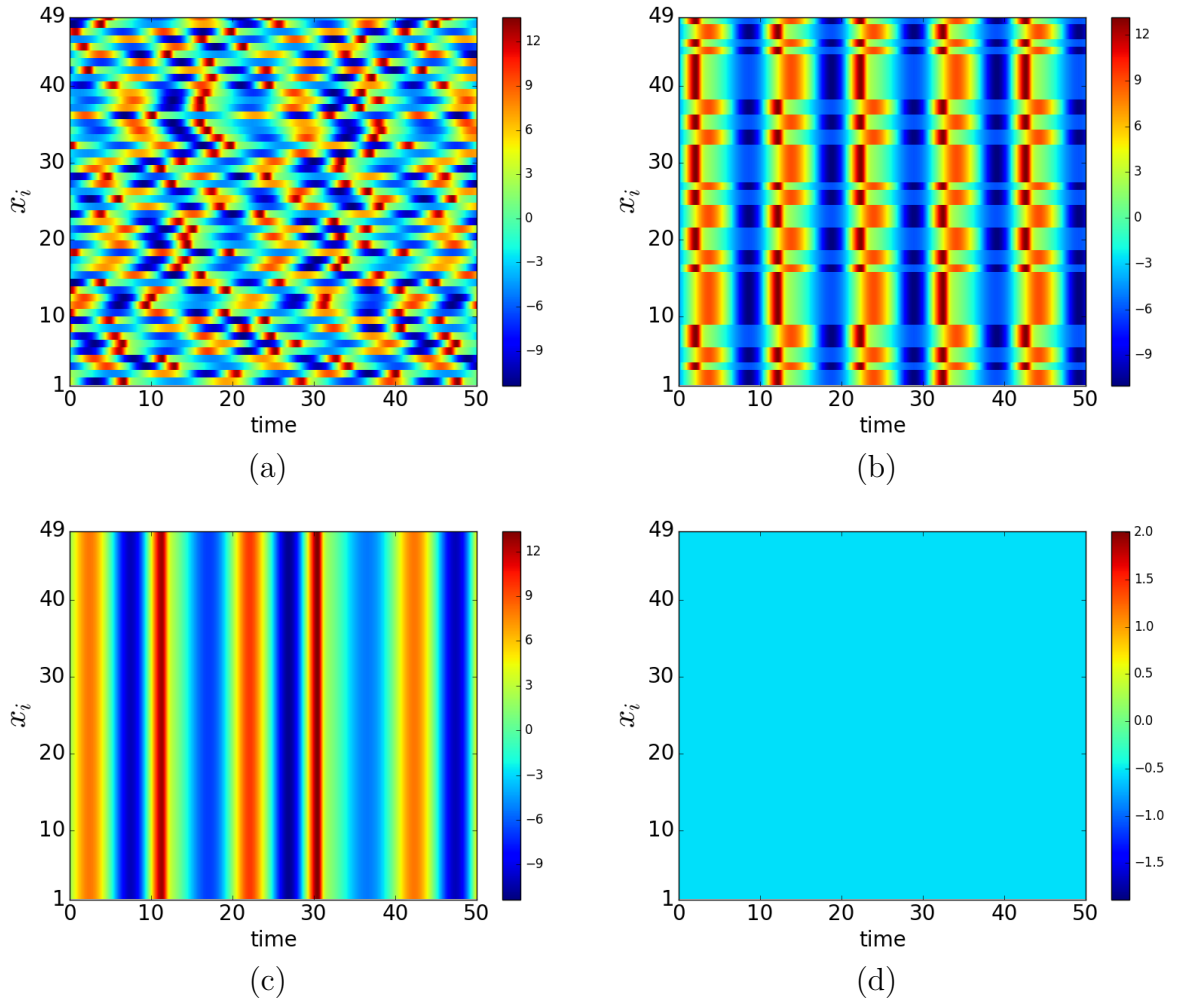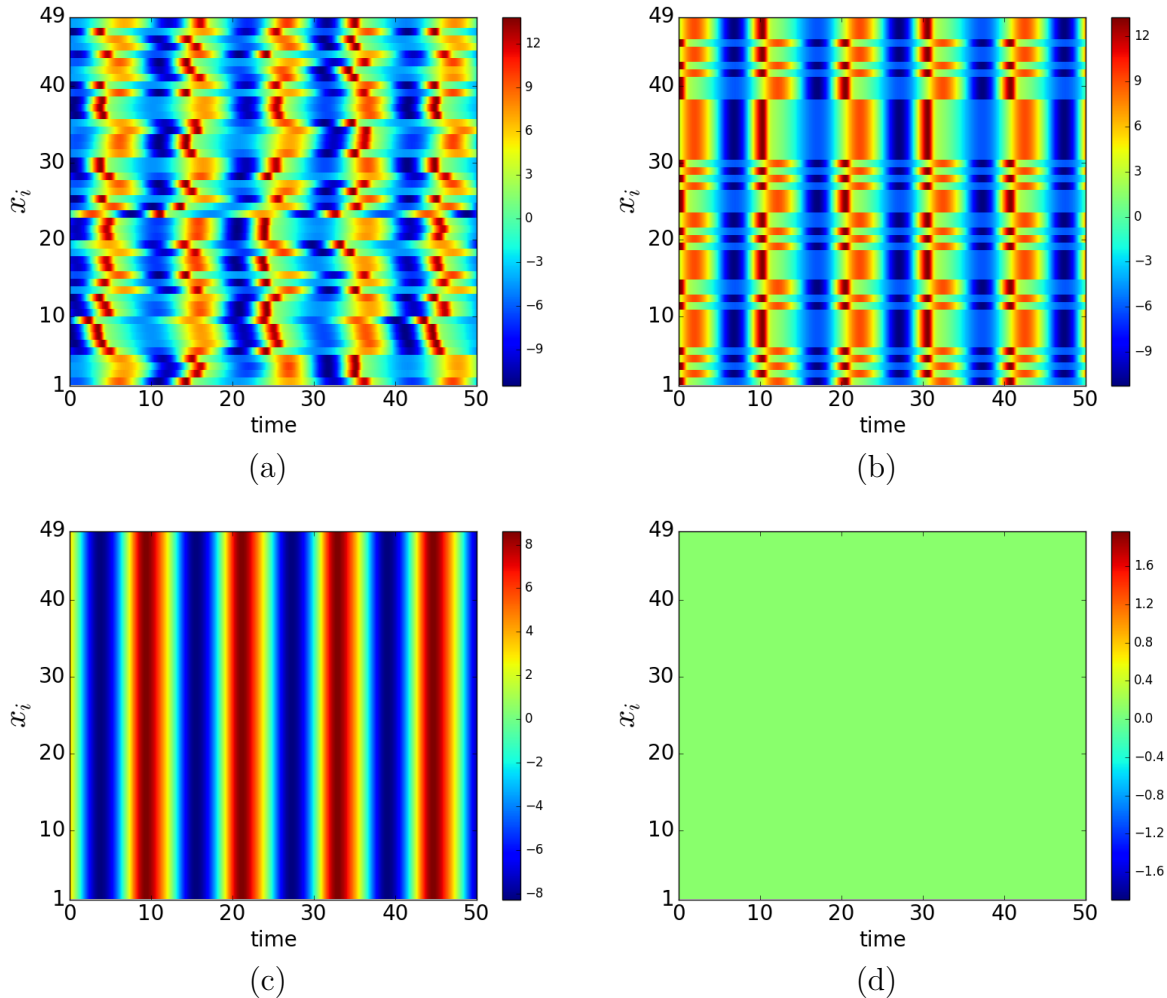
Figure 3.3: Space-time plot displaying the evolution of the state $x_i$ of the end-nodes of a star network of mean-field coupled Rössler systems for system size $n = 50$. Here coupling strength $k = 0.01$ (a), $k = 0.03$ (b), $k = 0.25$ (c), $k = 0.35$ (d).

in synchrony with any other node. The phase portraits show that the desynchronized nodes are chaotic attractors with different geometries, while the synchronized nodes show periodic behavior. So the symmetry of the end-nodes, that have identical dynamical equations and coupling environments, is broken to yield a synchronized periodic group and a desynchronized chaotic group.

This feature is highlighted in yet another representative example in Fig. 3.5, displaying the attractors obtained for the end-nodes in the diffusively coupled case. It is evident from Fig. 3.5 that sub-sets of the end-nodes display very different attractor geometries, though they have identical dynamical equations. Fig. 3.6 further shows the state of synchronization of the different end-nodes $i = 1, \ldots N - 1$ at some representative instant of time. demonstrating the co-existence of synchronized and de-synchronized groups
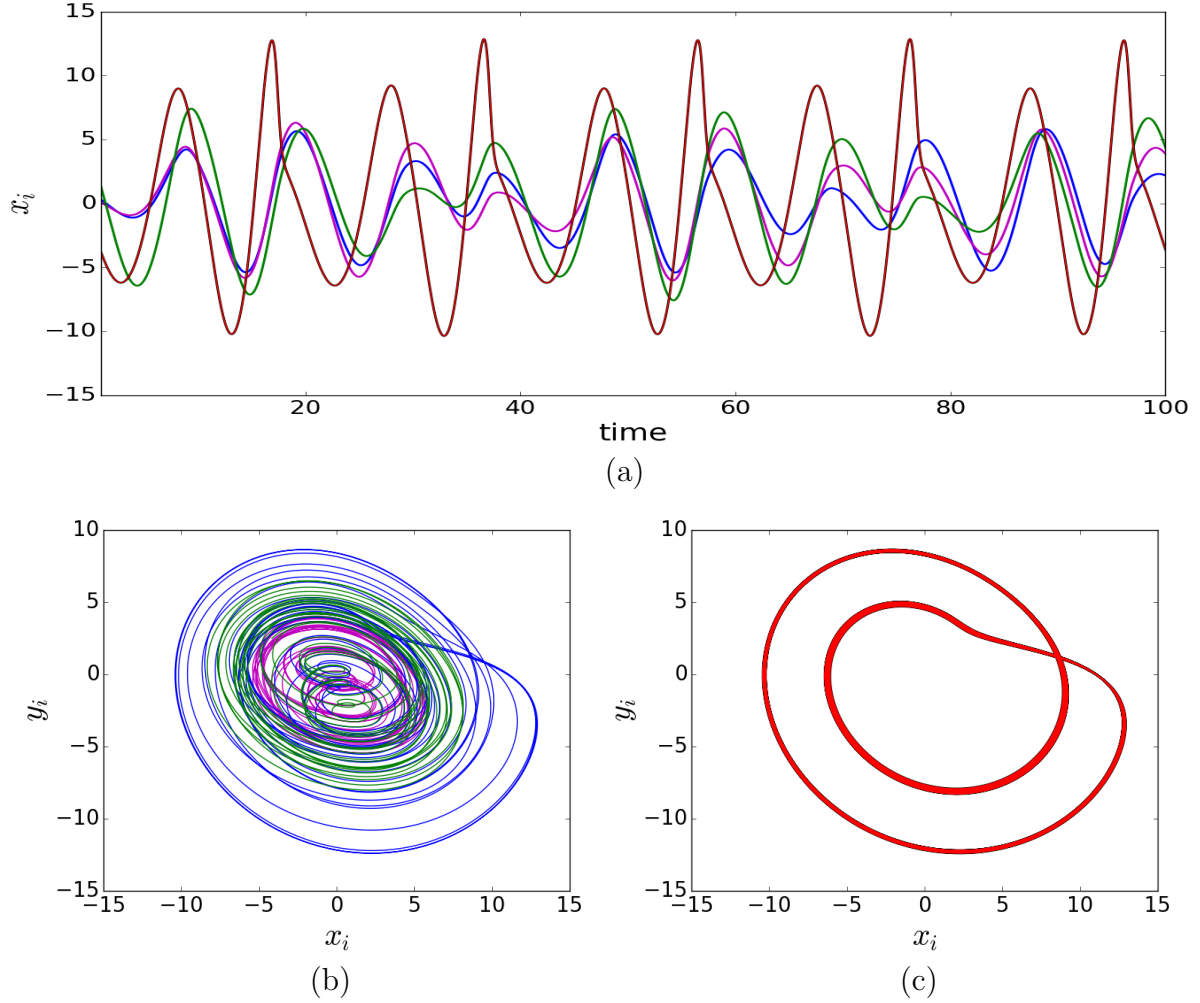
Figure 3.4: (a)Time evolution of the $x$ variable of the end-nodes of a diffusively coupled star network of Rössler systems, after transience, for coupling strength $k = 0.284$, and system size N = 100 and the corresponding attractors in phase space in the bottom row. Here the identical end-nodes split into 2 groups: a synchronized set (shown in red), and 3 nodes that are not in synchrony with any other node (shown in blue, green and magenta). The phase portraits show that the desynchronized nodes are chaotic attractors with different geometries (b), while the synchronized nodes show periodic behaviour (c).

among the identical $N - 1$ peripheral nodes in the star network. Note that there is no space ordering of the node index $i$ of the end-nodes. So the (de)synchronized nodes in a cluster are not "contiguous", as is usual in regular lattice topologies.

(a)

(b)
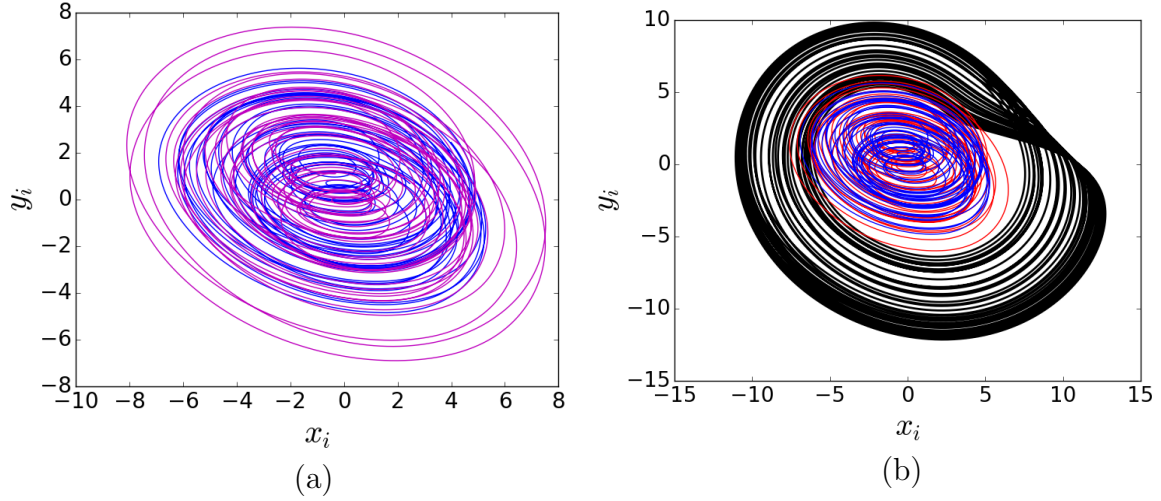
Figure 3.5: Phase portraits of diffusively coupled Rössler systems in a star network of size $N = 100$, with coupling strength $k = 0.32$ of the (a) de-synchronized set (blue and magenta) and (b) three distinct synchronized clusters (black, red and blue).
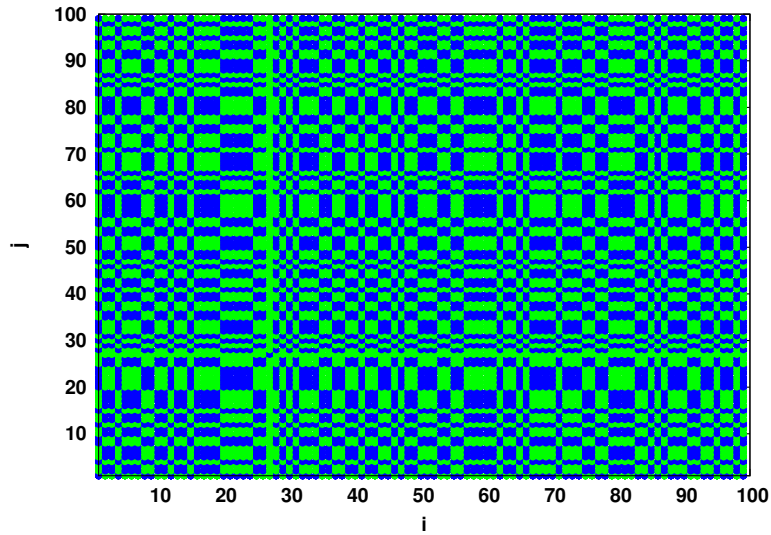


Figure 3.6: A matrix displaying the state of synchronization of nodes $i$ and $j$ in a star network of conjugately coupled Rössler systems ($i, j = 1, \ldots N - 1$). The blue color indicates that the nodes are synchronized and the green that they are de-synchronized. Here coupling strength $k = 0.24$ and system size $N = 100$. The presence of a synchronized group of nodes, along-side a de-synchronized set, can be clearly seen.

### 3.2.2 Dynamical Patterns for Coupled Lorenz Systems

We also consider the Lorenz system at the nodes given by:

$$
\begin{aligned}
f_x(x_i, y_i, z_i) &= \sigma(y_i - x_i) \\
f_y(x_i, y_i, z_i) &= (r - z_i)x_i - y_i \\
f_z(x_i, y_i, z_i) &= x_i y_i - \beta z_i
\end{aligned}
\tag{3.4}
$$

in Eqn. 3.1. With no loss of generality we consider the parameters of the local system to be $\sigma = 10$, $r = 28$ and $\beta = 8/3$, yielding double-scroll attractors.
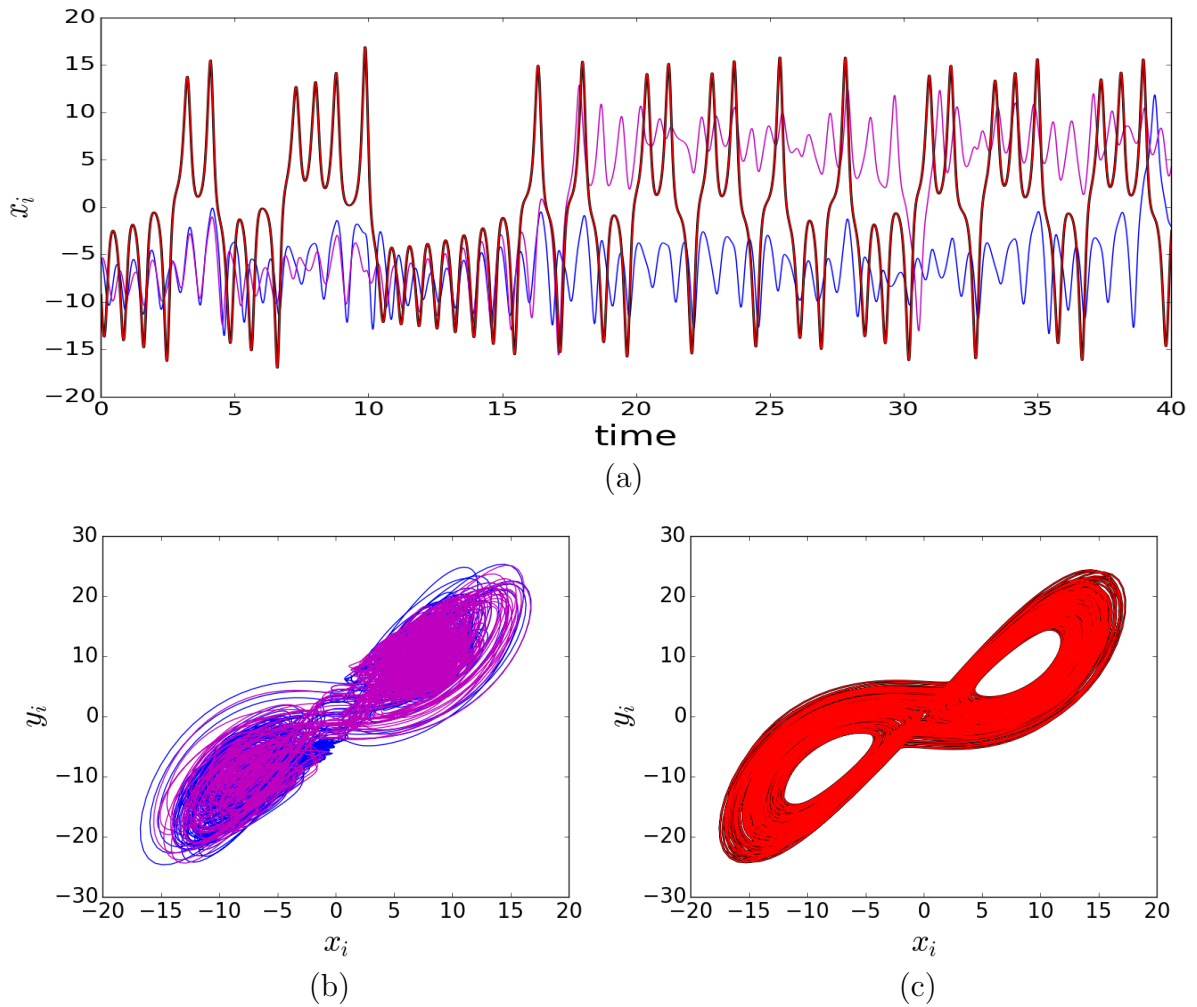


Figure 3.7: Time evolution (a) and the corresponding phase portrait, for a star network of diffusively coupled Lorenz systems with coupling strength $k = 9$, yielding a de-synchronized group (b) and a synchronized group (c).

Here again we find that as coupling strength increases, the end-nodes go from a desynchronized state to a completely synchronized state, via a large coupling parameter

regime yielding chimera states. We display some representative patterns from the chimera states in Fig. 3.7 for diffusive coupling and in Fig. 3.8 for conjugate coupling. It is clearly evident from these that the identical end-nodes split into different dynamical groups, thereby breaking symmetry. Some of these groups consist of synchronized nodes and some are clusters of desynchronized elements, as seen from Figs. 3.9, 3.10 and 3.11. Further, it is also evident from Figs. 3.7 and 3.8 that in addition to different synchronization properties, the groups also yield different attractor geometries.



(a)



(b)

(c)
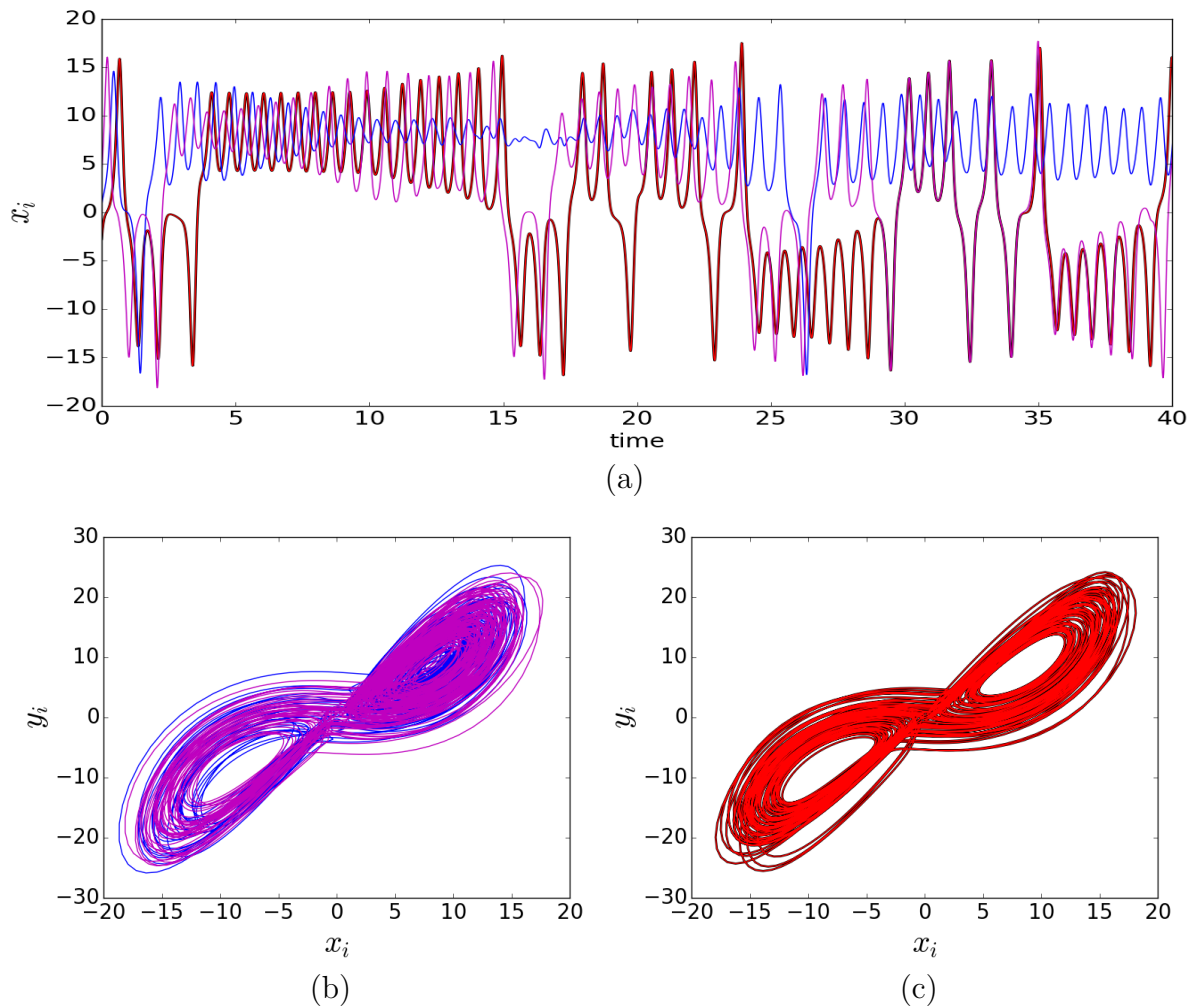
Figure 3.8: Time evolution (a) and the corresponding phase portrait, for a star network of conjugate coupled Lorenz systems with coupling strength $k = 2.9$, yielding a desynchronized group (b) and a synchronized group (c).
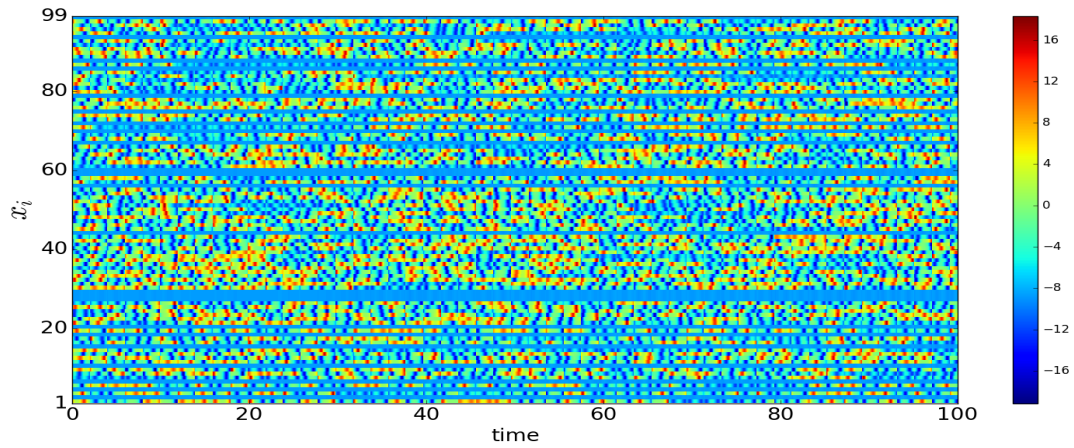
Figure 3.9: Space-time plot displaying the evolution of the state $x_i$ of the end-nodes of a star network of conjugately coupled Lorenz systems $(i = 1, \ldots N - 1)$, after transience. Here coupling strength $k = 1.32$ and system size $N = 100$. The presence of a synchronized group of nodes, along with a desynchronized set, can be clearly seen.
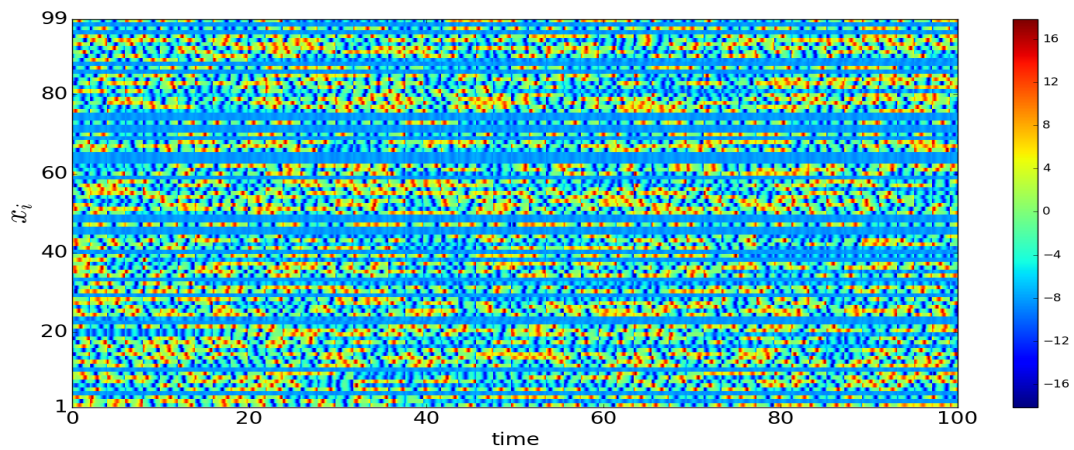


Figure 3.10: Space-time plot displaying the evolution of the state $x_i$ of the end-nodes of a star network of diffusively coupled Lorenz systems $(i = 1, \ldots N - 1)$, after transience. Here coupling strength $k = 2.48$ and system size $N = 100$. The presence of a synchronized group of nodes, along with a desynchronized set, can be clearly seen.
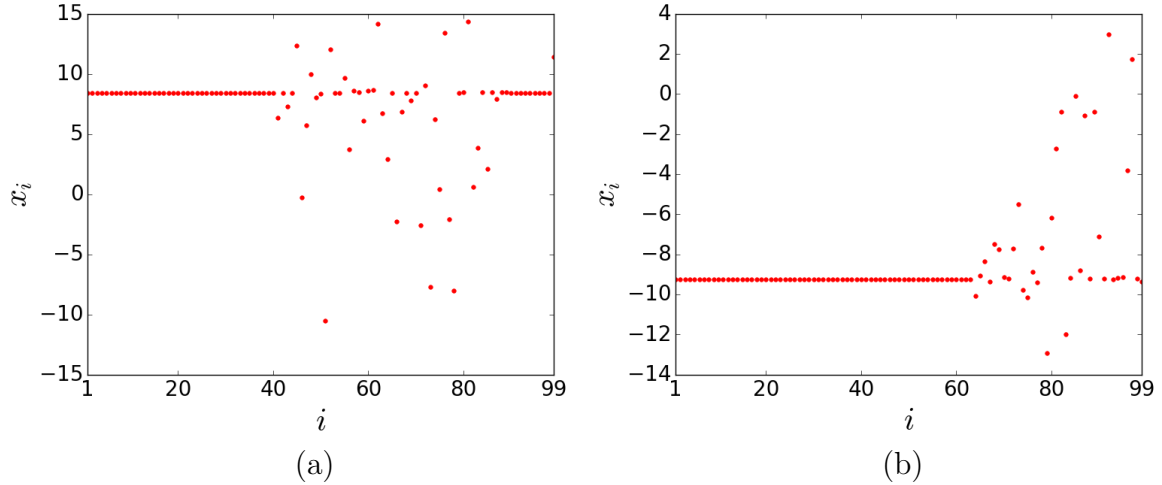
Figure 3.11: State $x_i$ of the end-nodes of a star network of conjugately coupled Lorenz systems ($i = 1, ...N - 1$), at an instant of time. Here coupling strength $k = 1.96$(a), $k = 1.98$(b) and system size $N = 100$. The presence of a synchronized group of nodes, along with a desynchronized set, can be clearly seen.
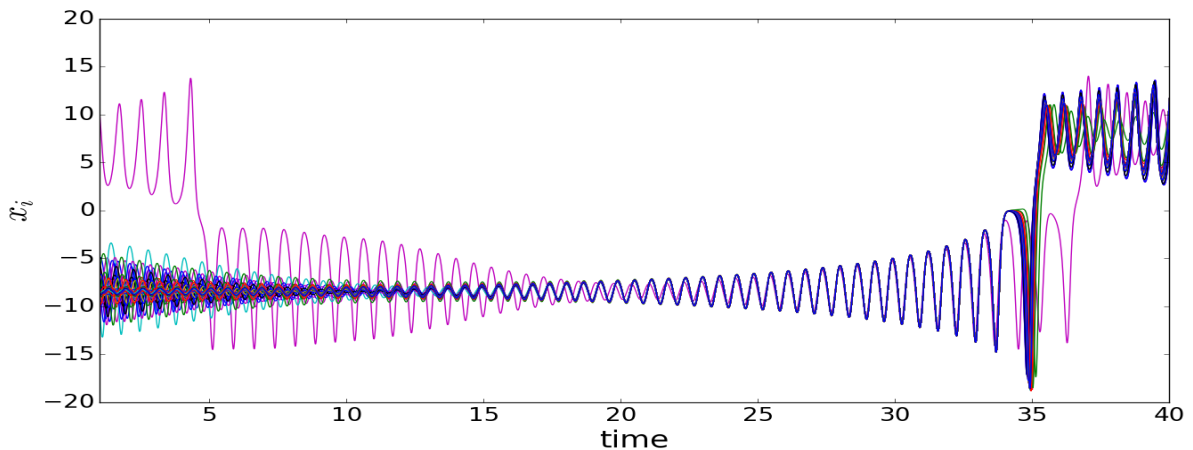


Figure 3.12: Temporal patterns of the end-nodes of a star network of diffusively coupled Lorenz systems displaying a breathing chimera state. Here coupling strength $k = 4.5$ and system size $N = 100$.

Further we find that the incoherent state maybe of two distinct types: (i) a stable chimera, namely a state where the synchronized and desynchronized sets of nodes remain unchanged in time,or (ii) a breathing chimera, which has an oscillating incoherent group that goes in and out of synchronization [43]. Such a breathing chimera-like state is displayed in Figs. 3.12 and 3.13. The occurrence of breathing chimera states is more common in the coupled Lorenz system than in coupled Rössler systems. In fact breathing chimeras were also observed in Lorenz systems coupled in a ring configuration in earlier studies [44].
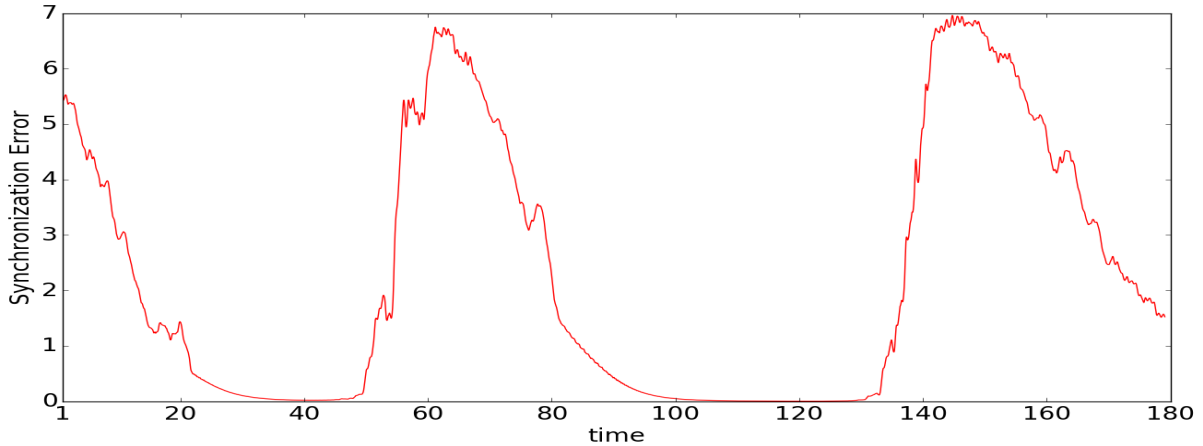
Figure 3.13: Synchronization error of the end-nodes of a star network of diffusively coupled Lorenz systems as a function of time (namely the standard deviation of $x_i$, $i = 1, \ldots N - 1$, at an instant of time). Here coupling strength $k = 5.12$ and system size $N = 100$. It is clearly evident from the oscillating synchronization error that the end-nodes move in and out of synchronization.

### 3.2.3 Prevalence of Chimera states

In order to quantify the probability of obtaining chimera states from random initial states we calculate the fraction of initial conditions leading to co-existing synchronized and de-synchronized states in the end-nodes, in a large sample of random initial states. This provides an estimate of the basin of attraction of the chimera state, and indicates the prevalence of chimeras in this system. So this measure is important, as it *allows us to gauge the chance of observing chimeras without fixing special initial states.*

Specifically, around $10^3$ initial conditions with the state variables spread uniformly over the interval $[-2:2]$ are considered. Figs. 3.14 and 3.15 display this quantity for star networks of Rössler and Lorenz systems. It is clearly evident from these figures that there exists extensive regimes of coupling parameter space where the probability of obtaining a chimera state is close to one. This quantitatively establishes the prevalence of chimeras in the end-nodes of nonlinear oscillators coupled in star configurations.

Also, Fig. 3.14 shows the dependence of chimera states on the size of the system. Rather interestingly, it is evident from the figure that *larger systems yield larger basins of attraction for the chimera state, thus having greater prevalence of chimeras.* Additionally, it can be clearly seen from Figs. 3.14-3.15 that *conjugate coupling yields larger parameter windows where the probability of obtaining a chimera state is close to* 1, namely there is

a high prevalence of chimera states in conjugately coupled star networks.



Figure 3.14: Probability of obtaining chimera states (red), synchronized clusters (magenta), fully synchronized states (green), and completely de-synchronized states (blue) in star networks of coupled Rössler systems, for the following cases: 10 nodes under (a) conjugate coupling and (b) diffusive coupling; 100 nodes under (c) conjugate coupling and (d) diffusive coupling.
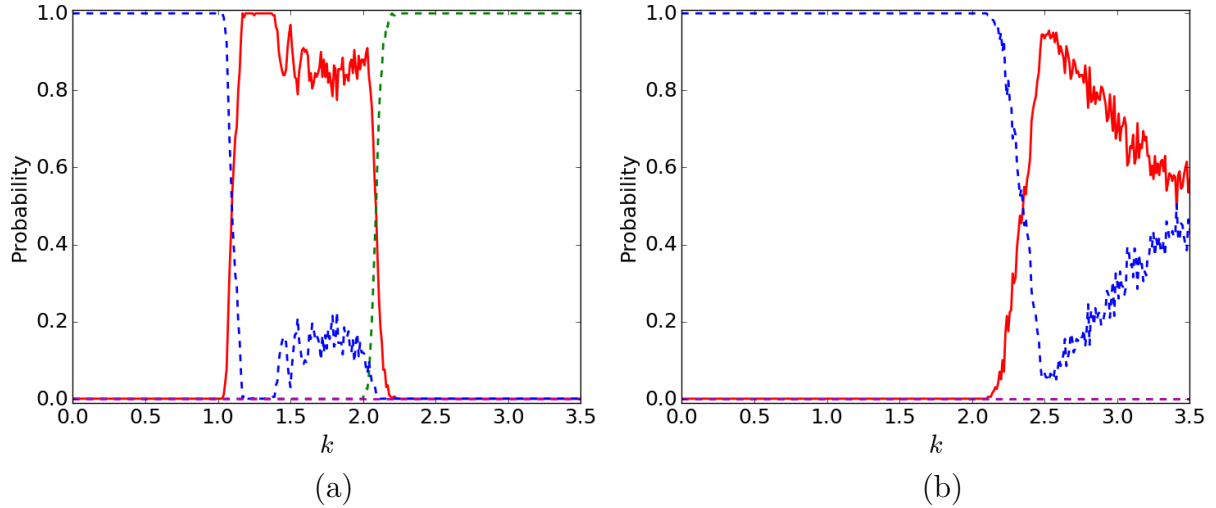
Figure 3.15: Probability of obtaining chimera states (red), synchronized clusters (magenta), fully synchronized states (green), and completely de-synchronized states (blue) in star networks of coupled Lorenz systems, of 100 nodes, under (a) conjugate coupling and (b) regular diffusive coupling.



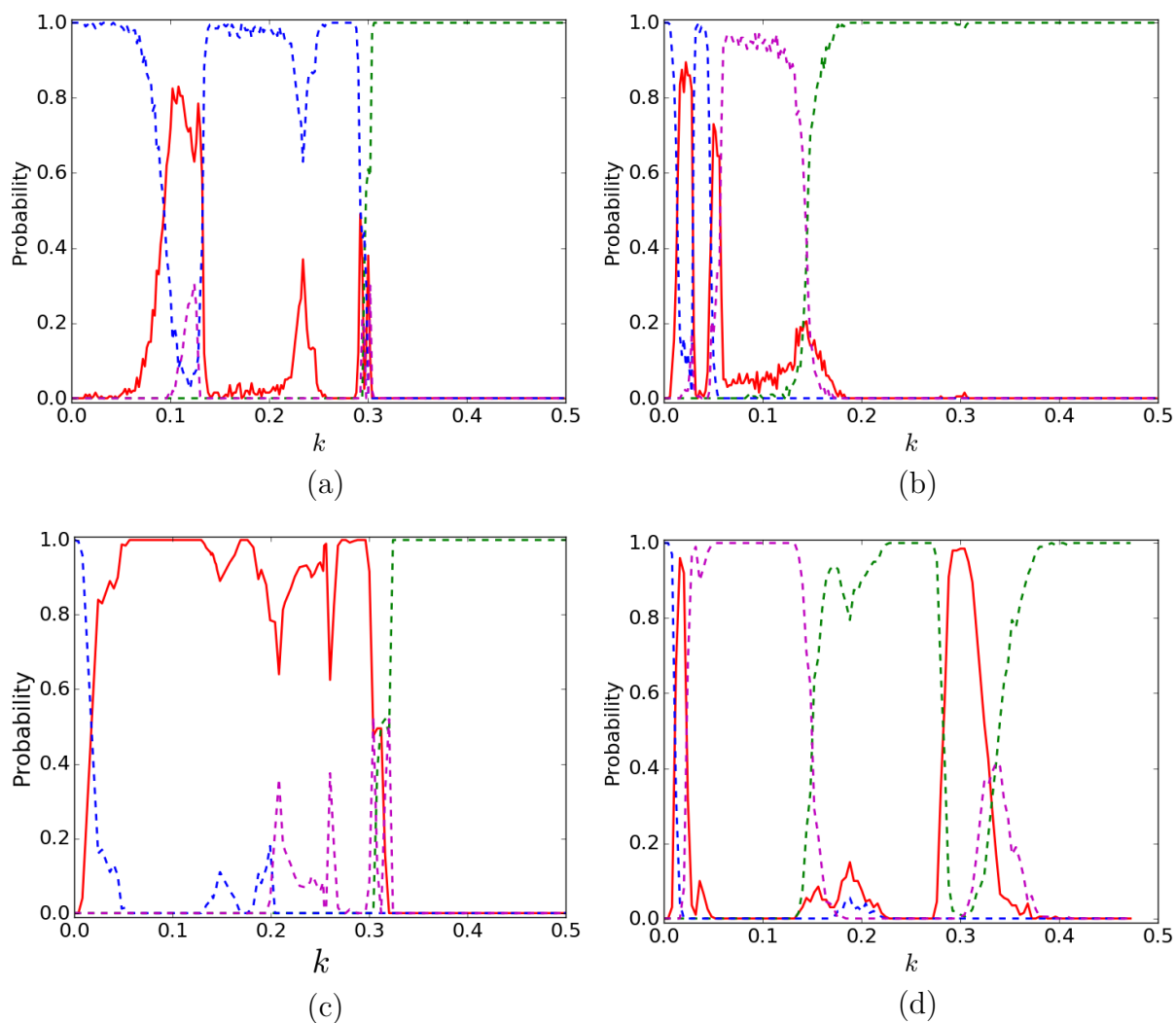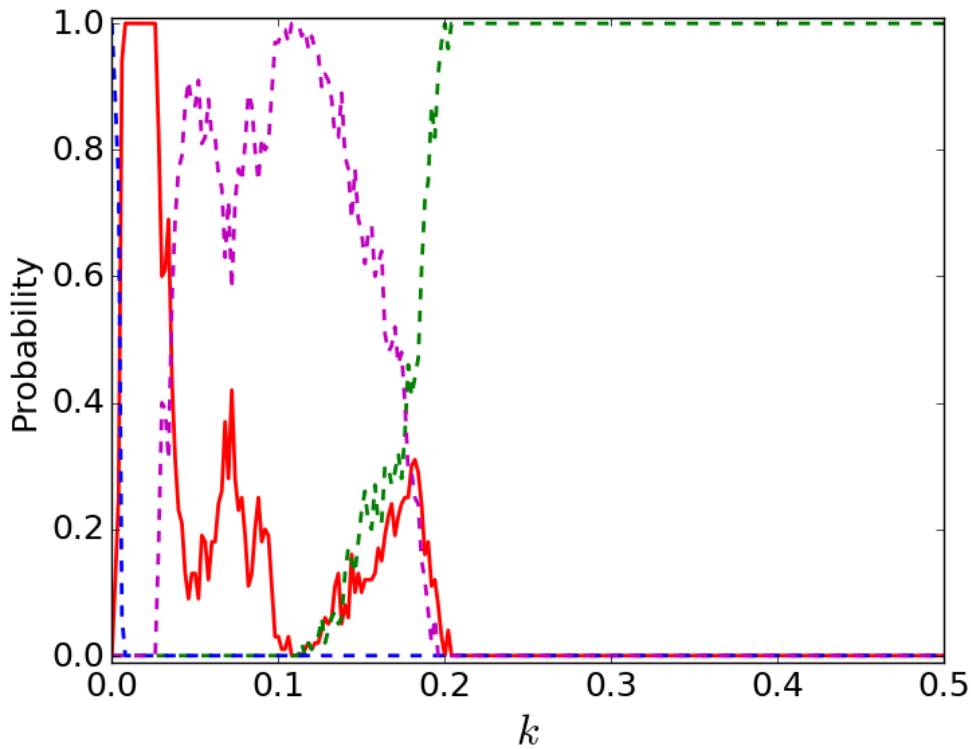Figure 3.16: Probability of obtaining chimera states (red), synchronized clusters (magenta), fully synchronized states (green), and completely de-synchronized states (blue) in star networks of coupled Rössler systems with mean-field diffusive coupling (cf. Eqns. 3-4) for a network of 100 nodes.

Lastly, we estimate the probability of obtaining the chimera state in the star network with mean- field diffusive coupling by finding, through numerical simulations, the fraction of initial states that evolve to chimera states. The results are displayed in Fig. 3.16, and it is clear that this form of coupling yields a large parameter regime where the typical initial state gives rise to a chimera state in the end-nodes.

## 3.2.4  Conclusions

In summary, we have investigated star networks of diffusively, conjugately and mean-field coupled nonlinear oscillators, with all end-nodes connected only to the central hub node. Though the end-nodes are identical in terms of the coupling environment and dynamical equations, they yielded chimera states. Namely, the symmetry of the end-nodes was broken and coexisting groups with different synchronization features and attractor geometries emerged. We find that as coupling strength increases, the end-nodes go from a de-synchronized state to a completely synchronized state, via a large coupling parameter regime yielding chimera states. The occurrence of breathing chimera states is more common in the coupled Lorenz system compare to coupled Rössler systems.

We estimated the basin of attraction of chimera states by evaluating the fraction of initial states that evolve to a chimera state, in a large sample of random initial conditions. This measure showed that in extensive regimes of coupling parameter space the probability of obtaining a chimera state is close to one. We found that larger networks yield larger basins of attraction for the chimera state. Conjugate coupling yields larger bands with high prevalence of chimera states compare to mean field diffusive and diffusive coupling.

Thus it is clearly evident from our numerical analysis that large parameter regimes of moderate coupling strengths yield chimera states from generic random initial conditions in this network topology. So star networks provide a promising class of coupled systems, in natural or human-engineered contexts, where chimeras are pervasive.

# Chapter 4

# Threshold-activated transport stabilizes chaotic populations to steady states

## 4.1 Introduction

Nonlinear systems, describing both natural phenomena as well as human-engineered devices, can give rise to a rich gamut of patterns ranging from fixed points to cycles and chaos. An important manifestion of our understanding of a complex system is the ability to control its dynamics, and so the search for mechanisms that enable a chaotic system to maintain a fixed desired activity has witnessed enormous research attention [45, 46]. In early years the focus was on controlling low-dimensional chaotic systems, and guiding chaotic states to desired target states [47, 48, 49, 50]. Efforts then moved on to the arena of lattices modelling extended systems, and the control of spatiotemporal patterns in such systems [51]. With the advent of network science to describe connections between complex sub-systems, the new challenge is to find mechanisms or strategies that are capable of stabilizing these large interactive systems [52].

In this chapter we consider a network of population patches [53, 54], or "a population of populations" [55]. Now, in analogy with reaction-diffusion processes, diffusive coupling has been very widely studied as a model of connections between population patches, with most models of metapopulation dynamics considering density dependent dispersal [56, 57, 58, 59, 60]. However, here we will investigate a different class of coupling, namely threshold-activated transport. The broad scenario underlying this is that each population patch has a critical population density it can support, and when the population in the patch, due to its inherent growth dynamics (which may be chaotic) exceeds this threshold, the excess migrates to neighbouring patches. The neighbouring patch on receiving the migrant population may become over-critical too, triggering further migrations. So this form of coupling is pulsatile and inter-patch transport occurs only when there is excessive build-up of population density in a patch, which may initiate a *cascade of transport events* [50, 61]. Though much less explored, in many situations this form of coupling may be expected to offer a more appropriate description of the connections between spatially distributed population patches.

In this chapter we will then aim to obtain broad insights on the dynamics of a complex network under threshold-activated transport, through the specific illustrative example of spatially distributed populations connected by threshold-activated migrations. Our principal question will be the following: what is the effect of threshold-activated dispersal on the dynamical patterns emerging in the network, and in particular, can threshold-activated coupling serve to *stabilize the intrinsically chaotic populations in the network to regular behaviour*, such as steady states or regular cycles? In this chapter first we will

analyze the dynamics of a single population patch under threshold-activated transport and then we will discuss details of the nodal dynamics, as well as the salient features of pulsatile transport triggered by threshold mechanisms in Random Scale-Free network. We will then go on to demonstrate, through qualitative and quantitative measures, that such threshold-activated connections manage to stabilize chaotic populations to steady states. Further we will explore how the critical threshold that triggers the migration, and the timescales of the nodal dynamics vis-a-vis transport, influences the emergent dynamics.

## 4.2   Analysis of a single population patch under threshold-activated transport

We study a prototypical map, the Ricker (Exponential) map, modelling a single population patch. Such a map has been considered as a reasonably accurate model of population growth of species with non-overlapping generations [5]. It is given by the functional form:

$$x_{n+1} = f(x_n) = x_n \exp(r(1 - x_n)) \tag{4.1}$$

where $r$ is interpreted as an intrinsic growth rate and (dimensionless) $x_n$ is the population scaled by the carrying capacity at generation $n$. We consider $r = 4$, namely, an isolated uncoupled population patch displays *chaotic* behaviour. We will now analyze the dynamics of a single Ricker map, under threshold-activated transport. Specifically then we have the following scenario: in the dynamical evolution of the system, if the updated state exceeds a critical threshold $x_c$, it transports the excess out of the system and "re-sets" to level $x_c$. So the effective map of the dynamics is:

$$x_{n+1} = f(x_n) \quad \text{if} \quad f(x_n) < x_c \tag{4.2}$$
$$x_{n+1} = x_c \quad \text{if} \quad f(x_n) \geq x_c$$

This is effectively a "beheaded" or "flat-top" map, with the curve lying above $x_{n+1} > x_c$ in the usual Ricker map being "sliced" to $x_c$ (cf. Fig. 4.1a). The level at which the map is chopped off depends on the threshold $x_c$. The fixed point solution $x^\star$ occurs at the intersection of this $f(x)$ curve and the $45^0$ line, namely $x^\star = x_c$. Remarkably, this fixed

point is *super-stable* if the intersection occurs at the "flat top", since $f'(x^\star) = 0$ there.

Clearly, as the threshold increases the intersection of the effective map and the $45^0$ line is no longer located at the "flat-top". This is clear for the effective maps for $x_c = 0.5$ vis-a-vis that for $x_c = 1.5$ in Fig. 4.1a. So $x^\star$ for sufficiently high $x_c$ will no longer be stable (eg. $x_c = 1.5$ will not yield a stable fixed point). So we go on to inspect the second iterate of the effective map, in order to ascertain if a stable period-2 cycle is obtained (cf. Fig. 4.1b). Now the period-2 cycle solutions occur at the intersection of the $f^2(x)$ curve and the $45^0$ line, and again this cycle is stable if and only if the intersection occurs at the "flat top", namely where $f'(x) = 0$. In the illustrative example displayed in Fig. 4.1b it is clear that for $x_c = 0.5$, where the fixed point is super-stable, the period-2 is also naturally super-stable. Interestingly now, for $x_c = 1.5$, which had an unstable fixed point solution, the period-2 solution is super-stable. So higher $x_c$ also controls the intrinsic chaos. However, instead of a stable steady state, it yields stable periodic behaviour.

Alternately, one can understand the emergence of stable cycles under threshold control as follows: The ergodicity of the system ensures that the system will explore the available phase space fully, and the state variable is thus guaranteed to exceed threshold at some point in time. So one can analyse the dynamics of the effective map starting with the initial state at $x_c$. Now starting from $x_c$ the dynamics will run as in the usual Ricker population map until $x_{n+1} > x_c$, at which point it is re-set back to $x_c$ and the cycle starts again. So once it exceeds the critical value it is trapped immediately in a stable cycle whose periodicity is determined by the value of the threshold. Further, this allows us to exactly obtain the values of threshold $x_c$ that yield stable fixed points $x^*$ (namely period-1). This is simply the range of $x_c$ for which the first iterate of the Ricker map lies above $x_c$. In this range $f(x_c) > x_c$. So starting from an initial state $x_c$, we will be updated in the next iterate to a state greater than $x_c$, leading to the transport of the excess $f(x) - x_c$ out of the system and the "relaxation" of the system to $x_c$.

The curves $f_n(x_c)$ as a function of threshold $x_c$ are displayed in Fig. 4.2. For $n = 0$, $f_0(x_c) = x_c$; for $n = 1$, $f_1(x_c) = x_c \exp(r(1 - x_c))$, and in general $f_n(x_c) = f \circ f_{n-1}(x_c) = f \circ f \circ \ldots f(x_c)$. From the figure it can be clearly seen that in the range of $x_c \in [0 : 1]$, $f(x_c) > x_c$. So if the threshold is in this range, the system will evolve quickly to a steady state at $x^* = x_c$, and transport the excess, namely $f(x_c) - x_c$, out of the system after every update of the population in the patch.

Similarly, it can be seen that $f_2(x_c) = f(f(x_c))$ is larger than $x_c$ (while $f(x_c) < x_c$) in the range of threshold $x_c \in (1, 2]$. So in this range of threshold, we obtain a stable

period 2 cycle. Namely, the population at $x_c$ evolves to $f(x_c) < x_c$ which then evolves to $f^2(x_c)$. Since $f^2(x_c) > x_c$, it is mapped back to $x_c$. Hence a cycle of period 2 arises, with the values of the two points in the cycle being $x_c$ and $f(x_c)$. It can be seen from Fig. 4.2 that this range is from $x_c \sim 1$ to $x_c \sim 2$. This also corroborates the analysis using effective "flat-top" maps (cf. Fig. 4.1).



(a)          (b)
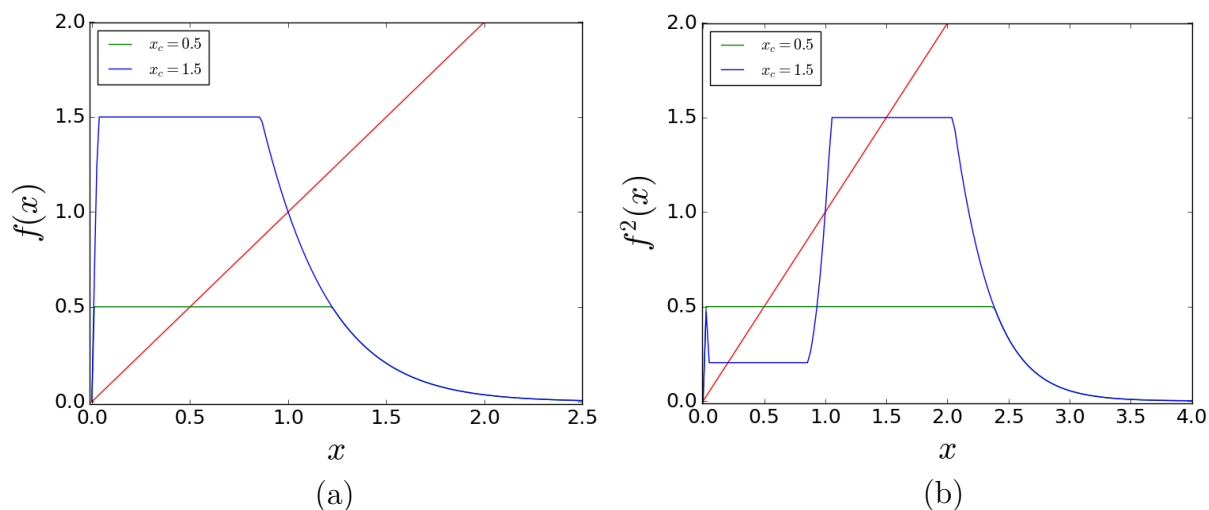
Figure 4.1: (a) $f(x)$ vs. $x$ and (b) $f^2(x)$ vs. $x$, for the effective threshold-controlled Ricker map ($r = 4$), for critical threshold levels: $x_c = 0.5$ (green) and $x_c = 1.5$ (blue). The fixed point solution occurs at the intersection of the $f(x)$ curve and the $45^0$ line, and is stable if the intersection occurs at the "flat top", namely where $f'(x) = 0$.
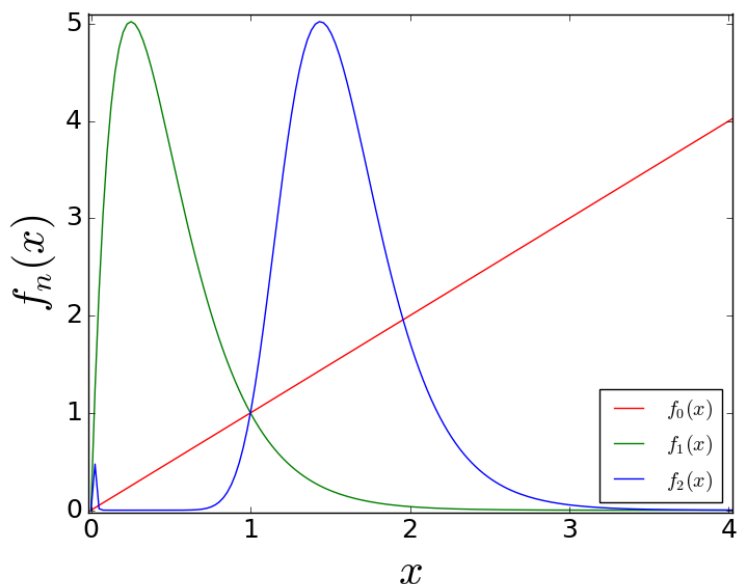


Figure 4.2: Plot of $f_n(x)$ vs $x$. Here $n = 0, 1, 2$, where $f_n(x)$ is the $n^{th}$ iterate starting from initial condition $x = x_c$ of the Ricker map with $r = 4$: $f_0(x)$ (red), $f_1(x)$ (green) and $f_2(x)$ (blue).

67

Fig. 4.3 shows the range of threshold values yielding period-1 and period-2 behaviour considering a single threshold-limited map.
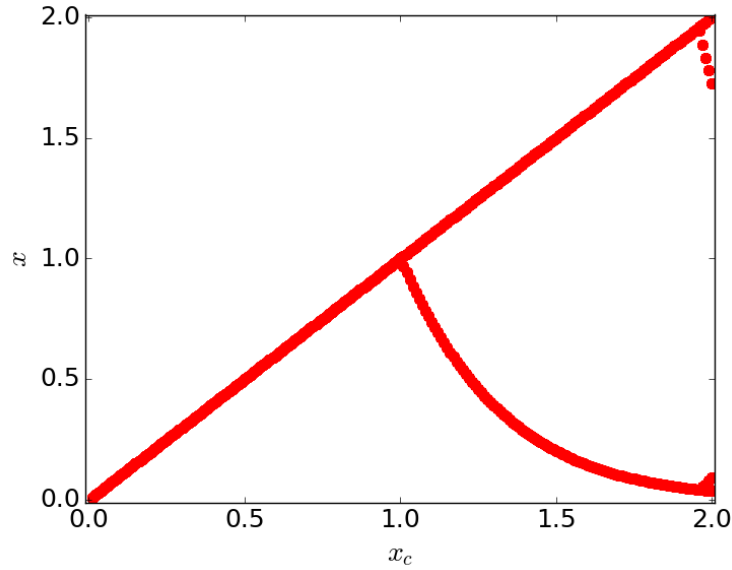


Figure 4.3: Bifurcation diagram of the threshold-controlled Ricker map (namely, the "flat-top" map), with respect to threshold level $x_c$.

## 4.3 Model

Now we will consider a network of $N$ sub-systems, characterized by variable $x_n(i)$ at each node/site $i$ ($i = 1, \ldots N$) at time instant $n$. Nodal dynamics is given by the functional form:

$$x_{n+1}(i) = f(x_n(i)) = x_n(i) \exp(r(1 - x_n(i))) \tag{4.3}$$

Where $x_n(i)$ is the population scaled by the carrying capacity at generation $n$ at node/site $i$. Note that the results we will subsequently present here, hold qualitatively for a wide class of unimodal nonlinear maps, of which the Ricker map is a specific example.

The coupling in the system is triggered by a threshold mechanisms [50, 62, 63, 64]. Namely, the dynamics of node $i$ is such that if $x_{n+1}(i) > x_c$, the variable is adjusted back to $x_c$ and the "excess" $x_{n+1} - x_c$ is distributed to the neighbouring patches. The threshold parameter $x_c$ is the critical value the state variable has to exceed in order to initiate threshold-activated coupling. So this class of coupling is *pulsatile*, rather than

the more usual continuous coupling forms, as it is triggered *only* when a node exceeds threshold.

Specifically, we study such population patches coupled in a Random Scale-Free network, where the network of underlying connections is constructed via the Barabasi-Albert preferential attachment algorithm, with the number of links of each new node denoted by parameter $m$ [10]. The resultant network is characterized by a fat-tailed degree distribution, found widely in nature. The underlying web of connections determines the "neighbours" to which the excess is equi-distributed. Further, certain nodes in the network may be open to the environment, and the excess from such nodes is transported out of the system. Such a scenario will model an open system, and such nodes are analogous to the "open edge of the system". We denote the fraction of open nodes in the network, that is the number of open nodes scaled by system size $N$, by $f^{open}$. We also consider closed systems with no nodes open to the environment, where nothing is transported out of the system, i.e. $f^{open} = 0$.

So the scenario underlying this is that each population patch has a critical population density $x_c$ it can support, and when the population in the patch, due to its inherent chaotic growth dynamics, exceeds this threshold, the excess population moves to a neighbouring patch. The neighbouring patch on receiving the excess may exceed threshold too. Thus a few over-critical patches may initiate a domino effect, much like an "avalanche" in models of self-organized criticality [65] or cascade of failures in models of coupled map lattices [66]. So the main mechanisms for mitigating excess is through redistribution of excess, which ensures that nodes that are under-critical will absorb some excess population, and through the transport of excess out of the network via the open nodes. All transport activity in the network stops, namely the cascade ceases, when all patches are under the critical value, i.e. all $x(i) < x_c$.

So there are two natural time-scales here. One time-scale characterizes the chaotic update of the populations at node $i$. The other time scale involves the redistribution of population densities arising from threshold-activated transport. We denote the time interval between chaotic updates, namely the time available for redistribution of excess resulting from threshold-activated transport processes, by $T_R$. This is analogous to the *relaxation time* in models of self-organized criticality, such as the influential sandpile model [65]. $T_R$ then indicates the comparative time-scales of the threshold-activated migration and the intrinsic population dynamics of a patch.

## 4.4 Results

We have simulated this threshold-coupled scale-free network of populations, under varying threshold levels $x_c$ ($0 \leq x_c \leq 2$). We considered networks with varying number of open nodes, namely systems that have different nodes/sites open to the environment from where the excess population can migrate out of the system. Further, we have studied a range of redistribution times $T_R$, capturing different timescales of migration vis-a-vis population change [67].

With no loss of generality, in the following sections, we will present salient results for Random Scale-Free networks with $m = 1$, and specifically demonstrate, both qualitatively and quantitatively, the stabilization of networks of chaotic populations to steady-states under threshold-activated coupling. We will also present some qualitatively important results for Random Scale-Free networks with $m = 2$.

### 4.4.1 Influence of redistribution time on emergence of steady states

First, we consider the case of large $T_R$, where the transport processes are fast compared to the population dynamics, or equivalently, the population dynamics of the patch is slow compared to inter-patch migrations. Namely, since the chaotic update is much slower than the transport between nodes, the situation is analogous to the slow driving limit [65]. In such a case, the system has time for many transport events to occur between chaotic updates, and avalanches can die down, i.e. the system is "relaxed" or "under-critical" between the chaotic updates. So when the transport/migration is significantly faster than the population update (namely the time between generations), the system tends to reach a stationary state where all nodal populations are less than critical.

Figure 4.4: State of the nodes (coded in color) in a Random Scale-Free Network of intrinsically chaotic populations under threshold-activated coupling, at different instants of time. Here the steady state value represented by the light green color. Panel (a) displays the network at initial time, showing the random initial state of the network. Panel (b) shows the network after 100 time steps, clearly showing that all nodes have evolved to a steady state (as evident from the uniform light green color). The critical threshold $x_c = 0.5$, system size $N = 100$, $m = 1$ and there is a single node open to the environment. Redistribution time $T_R = 5000$.
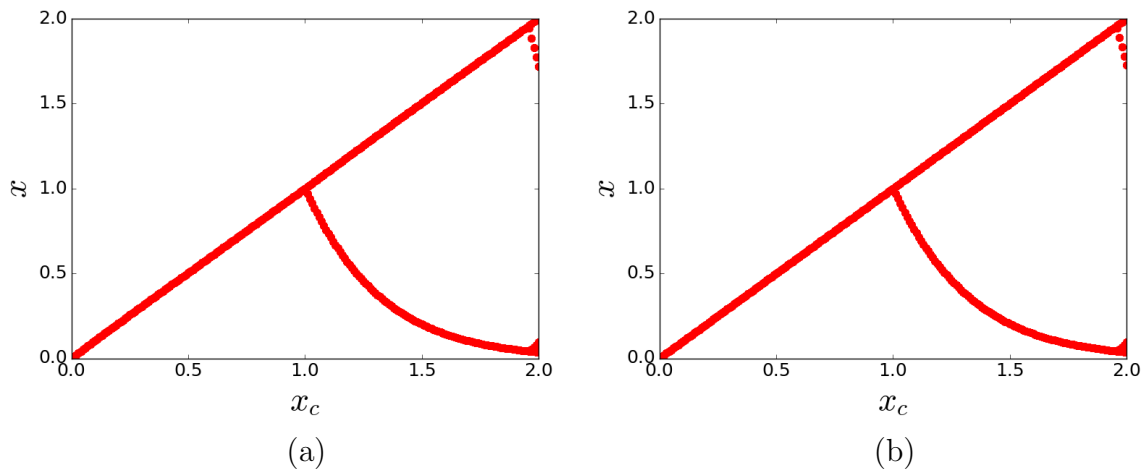


Figure 4.5: Bifurcation diagrams of the state of a representative node, with respect to critical threshold $x_c$, in a threshold-coupled Random Scale-Free network of intrinsically chaotic populations with $m = 1$ . Here $T_R = 5000$ and the network has a single open node, of degree (a) 1 and (b) 15.

An illustrative case of the state of the nodes in the network is shown in Fig. 4.4. Without much loss of generality, we display results for a network of size $N = 100$, for a representative large value of redistribution time $T_R = 5000$. It is clear that *all the nodes*
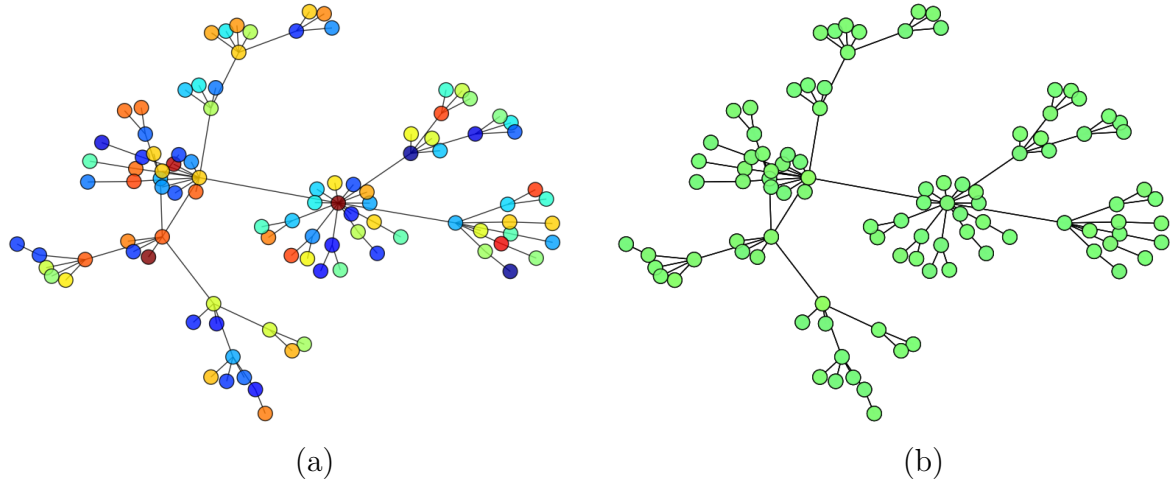
71

(a)                                    (b)
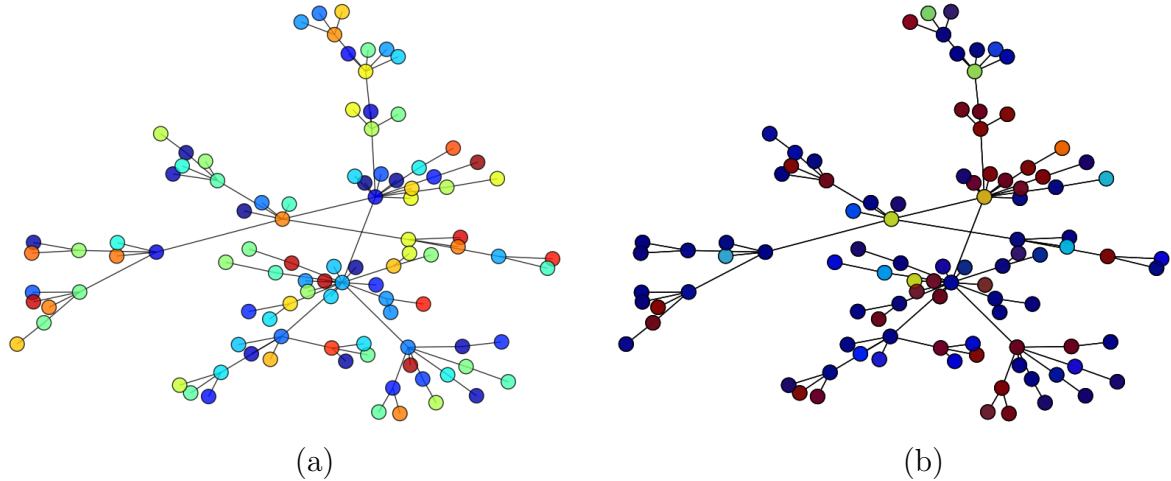
Figure 4.6: State of the nodes (coded in color) in a Random Scale-Free Network of intrinsically chaotic populations under threshold-activated coupling with $m = 1$, at different instants of time. Here the steady state value represented by the light green color. Panel (a) displays the network at initial time, showing the random initial state of the network and (b) shows the network after 100 time steps, clearly showing that all nodes have evolved to a steady state (as evident from the uniform light green color). The critical threshold $x_c = 0.5$, and there is a single node open to the environment. Redistribution time $T_R = 500$.

*in the network gets stabilized to a fixed point*, namely all population patches evolve to a stable steady state.

The next natural question is the influence of the critical threshold $x_c$ on the emergent dynamics, and this will be demonstrated through a series of bifurcation diagrams. Note that in all the bifurcation diagrams presented in this chapter we will display on the vertical axis the state $x$ of a representative site in the network, over several time steps after transience, with respect to threshold $x_c$ which runs along the horizontal axis.

It is clearly evident from the bifurcation diagrams in Fig. 4.5 that a *large window of threshold values* $(0 \leq x_c < 1)$ yield spatiotemporal steady states in the network [68, 69, 70]. It is also apparent that the degree of the open node does not affect the emergence of steady states here. Further, for threshold values beyond the window of control to fixed states, one obtains cycles of period 2. Namely for threshold levels $1 < x_c < 2$ the populations evolve in regular cycles, where low population densities alternate with a high population densities. This behaviour is reminiscent of the field experiment conducted by Scheffer et al [71] which showed the existence of self-perpetuating stable states alternating between blue-green algae and green algae. When there is enough time to relax between chaotic updates (namely $T_R$ is large and/or the number of open nodes is sufficiently high),

the collective excess of the network is transported out of the system. This implies that the individual nodes behave essentially like the "flat-top" map analysed in section 4.2. This explains why the range of threshold values yielding fixed points and period-2 cycles obtained in networks of threshold-coupled chaotic systems (cf. Fig. 4.5) matches so well with that obtained there (cf. Fig. 4.3).

So our first result can be summarized as follows: when redistribution time $T_R$ is large and the critical threshold $x_c$ is small, we have very efficient control of networks of chaotic populations to steady states. This suppression of chaos and quick evolution to a stable steady states occurs irrespective of the number of open nodes.

## 4.4.2   Influence of the number of open nodes on the suppression of chaos

Now we focus on the network dynamics when $T_R$ is small, and the time-scales of the nodal population dynamics and the inter-patch transport are comparable. When redistribution time $T_R$ is small then we do not have very efficient control of networks of chaotic populations to steady states (cf. Fig. 4.6). So now there will be nodes that may remain over-critical at the time of the subsequent chaotic update, as the system does not have sufficient time to "relax" between population updates.

The network is then akin to a rapidly driven system, with the de-stabilizing effect of the chaotic population dynamics competing with the stabilizing influence of the threshold-activated coupling. So for small $T_R$, the system does not get enough time to relax to under-critical states and so perfect control to steady states may not be achieved. Now we will see the effect of the number of open edge nodes on suppression of chaos in the network.

Importantly now, the fraction of open nodes $f^{open}$ is crucial to chaos suppression. In general, a larger fraction of open nodes facilitates control of the intrinsic chaos of the nodal population dynamics, as the de-stabilizing "excess" is transported out of the system more efficiently. We investigate this dependence, through space-time plots of representative networks with varying number of open nodes and redistribution times (cf. Fig. 4.7), and through bifurcation diagrams of this system with respect to critical threshold $x_c$ (cf. Fig. 4.8).

It is apparent from Fig. 4.7, that when there are enough open nodes, the network

73

relaxes to the steady state even for low redistribution times. Also notice from Fig. 4.7(d) that the system *reaches the steady state very rapidly*, namely within a few time steps, from the random initial state. So more open nodes yields better control of the intrinsic chaos of the nodal population dynamics to fixed populations.
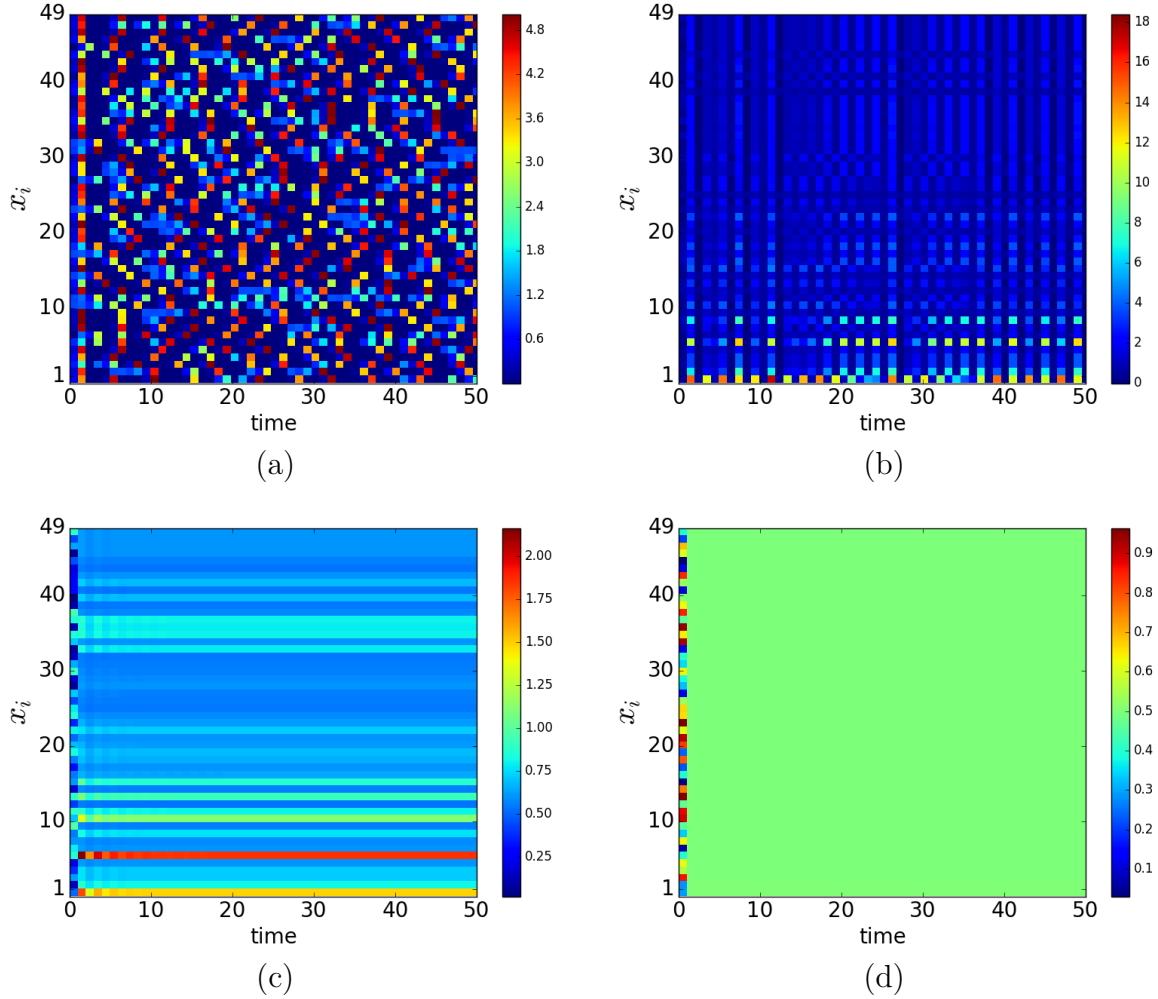


Figure 4.7: Space-time plots displaying the spatiotemporal behaviour of a Random Scale-Free network of intrinsically chaotic populations with $m = 1$ . Panel (a) shows the case of uncoupled chaotic populations evolving from a representative random initial state. Panels (b), (c), (d), (e) and (f) show the evolution of the same populations connected through threshold-activated coupling. System size $N = 50$, the critical threshold $x_c = 0.5$, redistribution time $T_R = 50$, and the number of open nodes in the network is (b) 1, (c) 10, (d) 30.

This is also corroborated in the bifurcation diagrams displayed in Fig. 4.8, where control to steady states is seen even for low $T_R$, when there are large number of open

nodes, vis-a-vis networks with few open nodes. Further contrast this with the dynamics of a system with large $T_R$, shown earlier in Fig. 4.5, where even a *single* open node leads to stable steady states for a large range of threshold values.
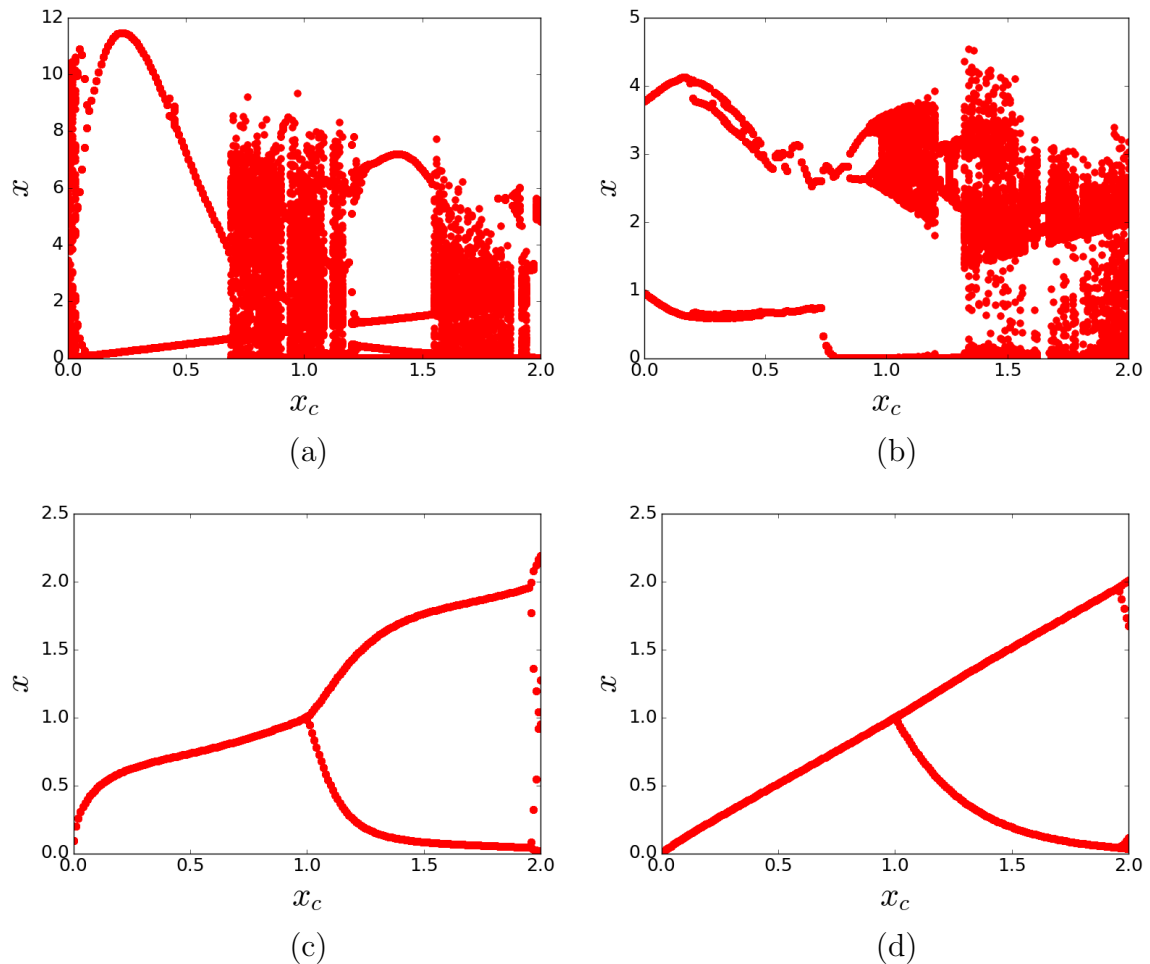


Figure 4.8: Bifurcation diagrams for one representative node in a threshold-coupled Random Scale-Free network of intrinsically chaotic populations with $m = 1$, with respect to critical threshold $x_c$ with $m = 1$. Here $T_R = 50$ and the number of open nodes is (a) 1, (b) 10, (c) 30 and (d) 60.

Similar qualitative trends are also borne out in Random Scale-Free network with $m = 2$, where again more open nodes (cf. Fig. 4.9) and longer redistribution times result in better control to fixed population densities (cf. Fig. 4.10).
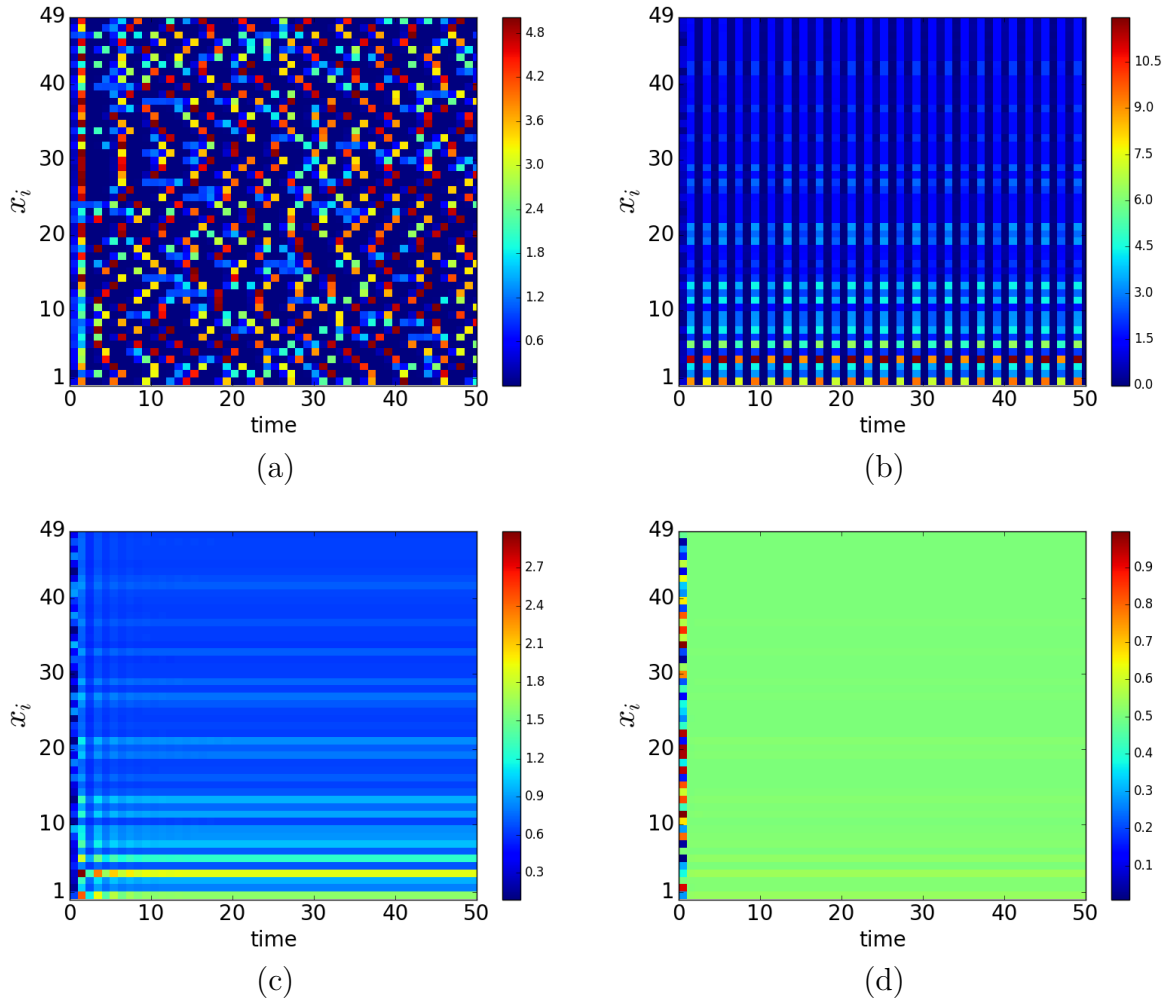
Figure 4.9: Space-time plots displaying the spatiotemporal behaviour of a Random Scale-Free network of intrinsically chaotic populations with $m = 2$. Panel (a) shows the case of uncoupled chaotic populations evolving from a representative random initial state. Panels (b), (c), (d), (e) and (f) show the evolution of the same populations connected through threshold-activated coupling. System size $N = 50$, the critical threshold $x_c = 0.5$, redistribution time $T_R = 50$, and the number of open nodes in the network is (b) 1, (c) 10, (d) 30.

Figure 4.10: Bifurcation diagrams of the state of a representative node, with respect to critical threshold $x_c$, in a threshold-coupled Random Scale-Free network of intrinsically chaotic populations with $m = 2$. Here the network has a single open node randomly chosen and $T_R = 500$ for (a), $T_R = 5000$ for (b)

### 4.4.3 Suppression of chaos in closed system

As a limiting case, we also studied the spatiotemporal behaviour of threshold-coupled networks without open nodes. Here the network of coupled population patches is a closed system.



Figure 4.11: Bifurcation diagram displaying the state of a representative site, for threshold-coupled populations in a Random Scale-Free network with $m = 1$. Here $T_R = 5000$ and there are no open nodes. Panel (a) shows the bifurcation diagram of one node and (b) shows for another node.

Again the intrinsic chaos of the populations is suppressed to regular behaviour, for large ranges of threshold values. However, rather than steady states, one now obtains period-2 cycles. This is evident through the bifurcation diagram of a closed network (cf. Fig. 4.11) vis-a-vis networks with at least one open node (cf. Fig. 4.5). Also, note the similarity of the bifurcation diagram of the closed system with that of a system with low $T_R$ and few open nodes. This similarity stems from the underlying fact that in both cases the network cannot relax to completely under-critical states by redistribution of excess between the population updates, either due to paucity of time for redistribution (namely low $T_R$) or due to the absence of open nodes to transport excess out of the system.

### 4.4.4 Influence of nodal properties in suppression of chaos

Further, we explore the case of networks with very few (typically 1 or 2) open nodes, and study the effect of the degree and betweenness centrality [1] of these open nodes on the control to steady states. We expect the degree and betweenness centrality of the open nodes to play a significant role for the following reason: the main mechanism for mitigating excess is through the transport of excess out of the network via the open nodes. This implies that the emergence of steady states is crucially dependent on the movement of excess occuring at any node in the network to an open edge in $T_R$ steps. So if an open node has more links to other nodes (namely, is of high degree), this would naturally facilitate the transport of excess to it, in parallel, through its many links. Also, an open node with high betweeness centrality implies that the node lies on many shortest paths connecting pairs of nodes. So this too should aid the process, as excess can reach the open node in fewer time steps.

Our expectations above are indeed verified through extensive simulations, where we observe the following: when there are very few open nodes, the degree and betweenness centrality of the open node is important, with the region of control being large when the open node has the high degree/betweenness centrality, and vice versa [2] See: [72]. This interesting behaviour is clearly seen in the bifurcation diagrams shown in Figs. 4.12a-d, which demonstrate that the degree and betweeness centrality of the open node has a pronounced influence on control.

---

[1]Betweenness centrality of a node is given as $b(i) = \sum_{s,t \in I} \frac{\sigma(s,t|i)}{\sigma(s,t)}$, where $I$ is the set of all nodes, $\sigma(s,t)$ is the number of shortest paths between nodes $s$ and $t$ and $\sigma(s,t|i)$ is the number of shortest paths passing through the node $i$.

[2]This is similar to the behaviour of heterogeneously connected networks of active-inactive elements, whose ability to maintain its dynamical activity is dependent on the degree of the node where local perturbations occured.
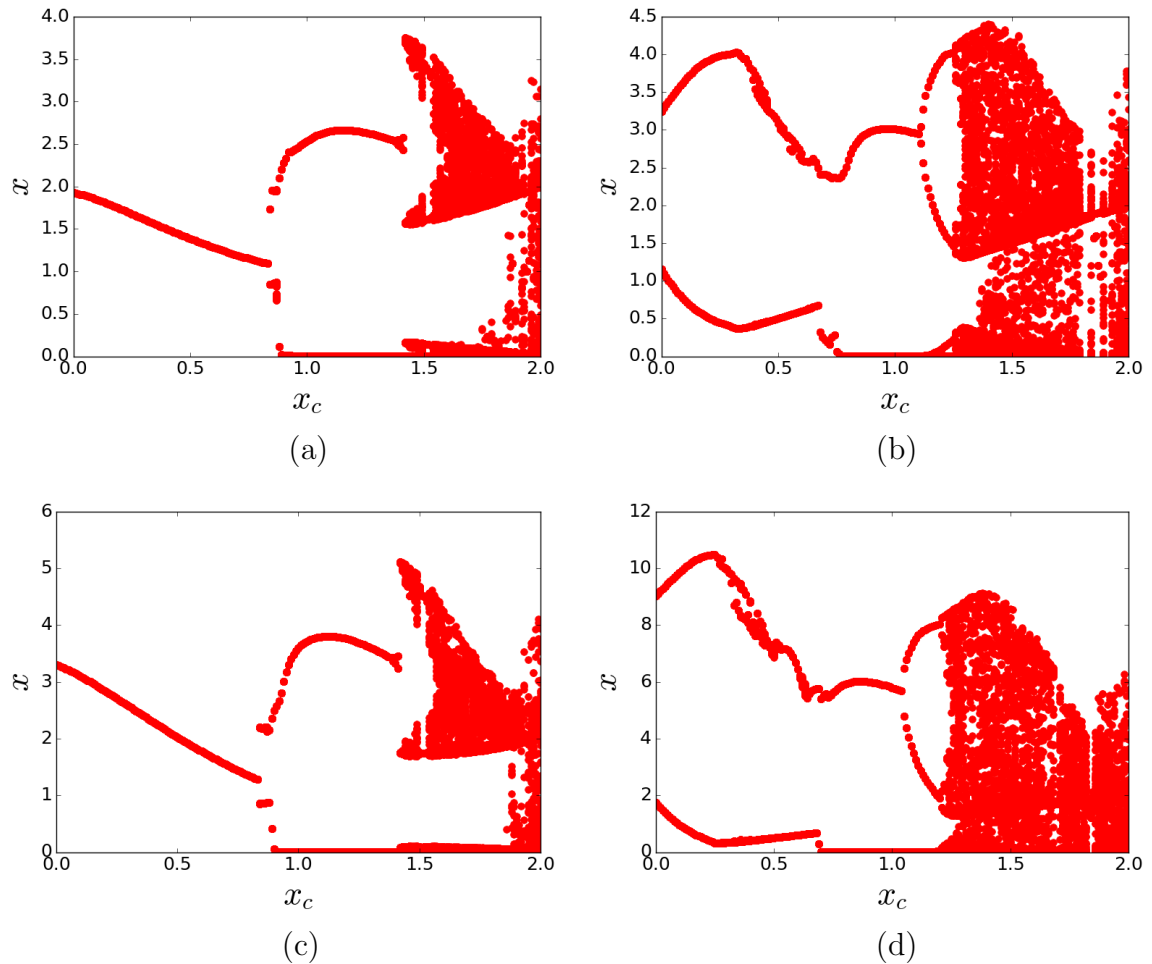
Figure 4.12: Bifurcation diagrams displaying the state of a representative node, with respect to critical threshold $x_c$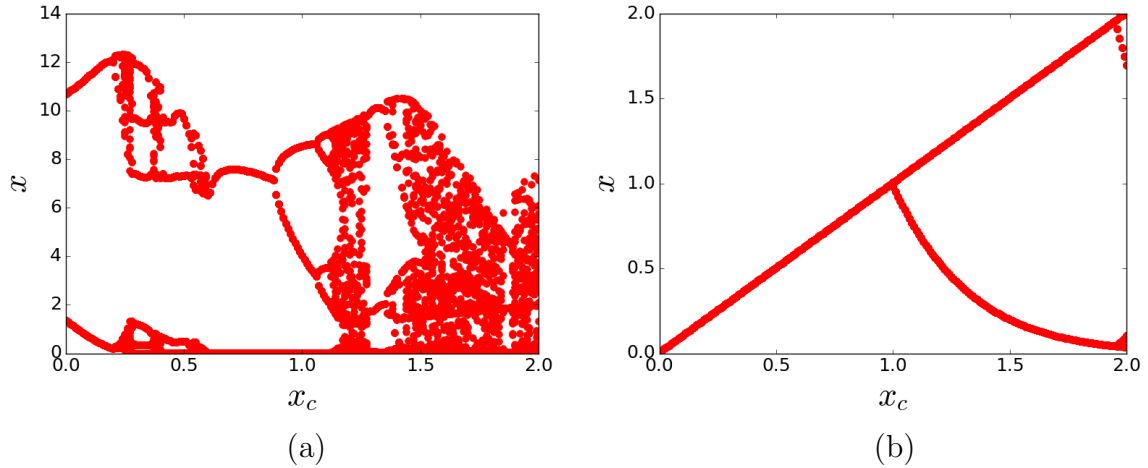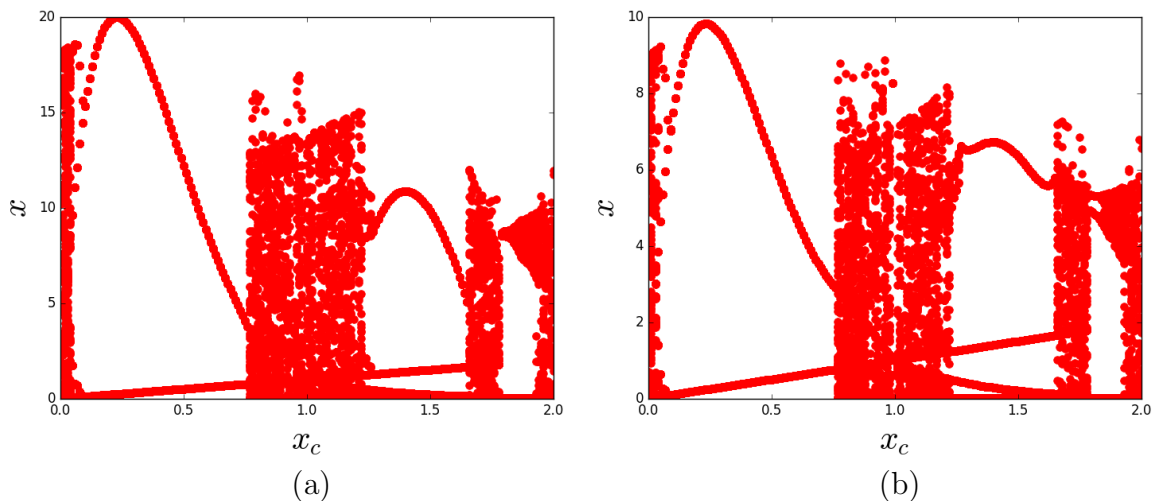, in a threshold-coupled Random Scale-Free network of intrinsically chaotic populations with $m = 1$. Here $T_R = 500$ and there is a single open node, with this open node having (a) the highest betweenness centrality, (b) the lowest betweenness centrality, (c) the highest degree and (d) the lowest degree in the network.

## 4.4.5 Quantitative Measures of the Efficiency of Chaos Suppression

We now investigate a couple of quantitative measures that provide indicators of the efficiency and robustness of the suppression of chaos in the network. The first quantity is the average redistribution time $\langle T \rangle$, defined as the time taken for all nodes in a system to be under-critical (i.e. $x_i < x_c$ for all $i$), averaged over a large sample of random initial states and network configurations. So $\langle T \rangle$ provides a measure of the efficiency of stabilizing the system, and reflects the rate at which the de-stabilizing "excess" is transported out of the network.
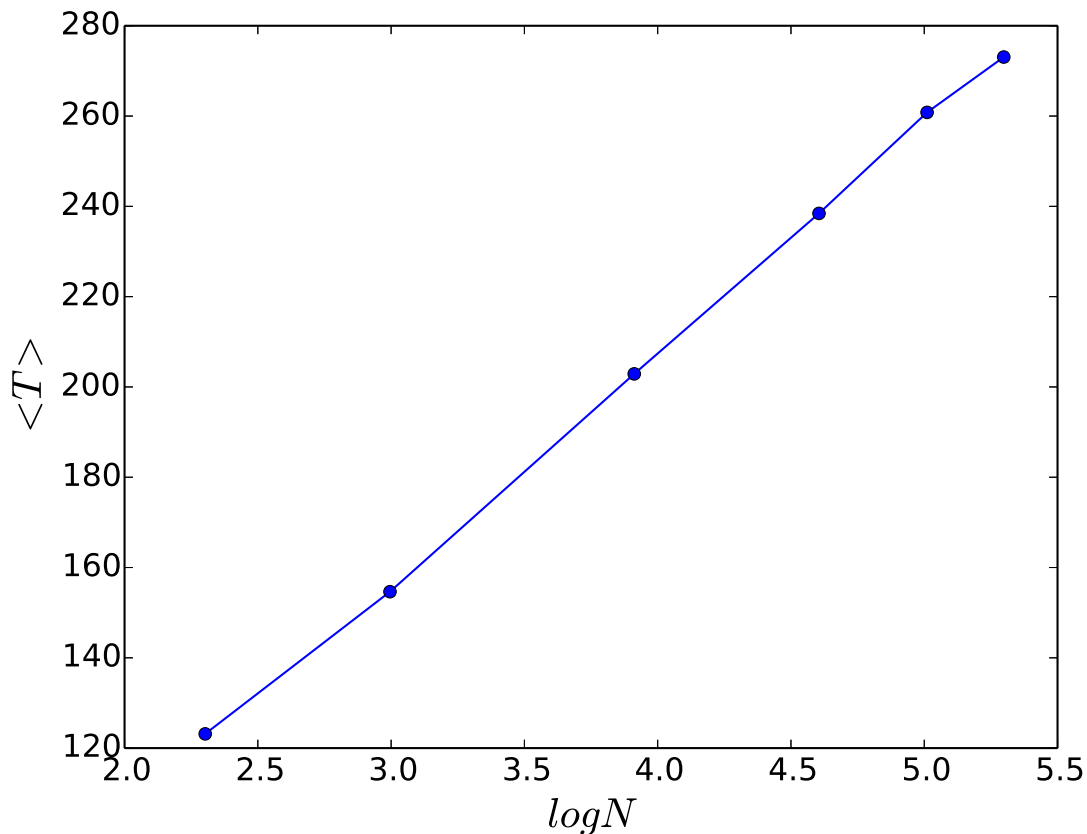


Figure 4.13: Average redistribution time $\langle T \rangle$, as a function of the logarithm of the network size $N$. Here $\langle T \rangle$ is defined as the time taken for all nodes in a system to be under-critical (i.e. $x_i < x_c, \forall i$), averaged over a large sample of random initial states and network configurations, the fraction of open nodes in the network is 0.2 and $x_c = 0.5$.

Fig. 4.13 shows the dependence of $\langle T \rangle$ on system size $N$. Clearly, while larger networks need longer redistribution times in order to reach steady states, this increase is only logarithmic. This can be rationalized as follows: the average redistribution time needed

for all nodes in a system to be under-critical reflects the average time taken by the excess from any over-critical node in the network to reach some open edge. So this should be determined by the diameter of the random scale-free graph, namely the maximum of the shortest path lengths over all pairs of nodes in the network, which scales with network size as $\ln N$.

This is further corroborated by calculating the average fraction of nodes in the network that go to steady states with respect to the redistribution time $T_R$, for networks of different sizes, with varying number of open nodes (cf. Fig. 4.14). Clearly for small systems, with sufficiently high $f^{open}$, very low $T_R$ can lead to stabilization of all nodes. Importantly, when the fraction of open nodes is very small, the average redistribution time $\langle T \rangle$ depends sensitively on the betweenness centrality of the open node, and to a lesser extent its degree. Figs. 4.15a-b present illustrative results demonstrating this observation.
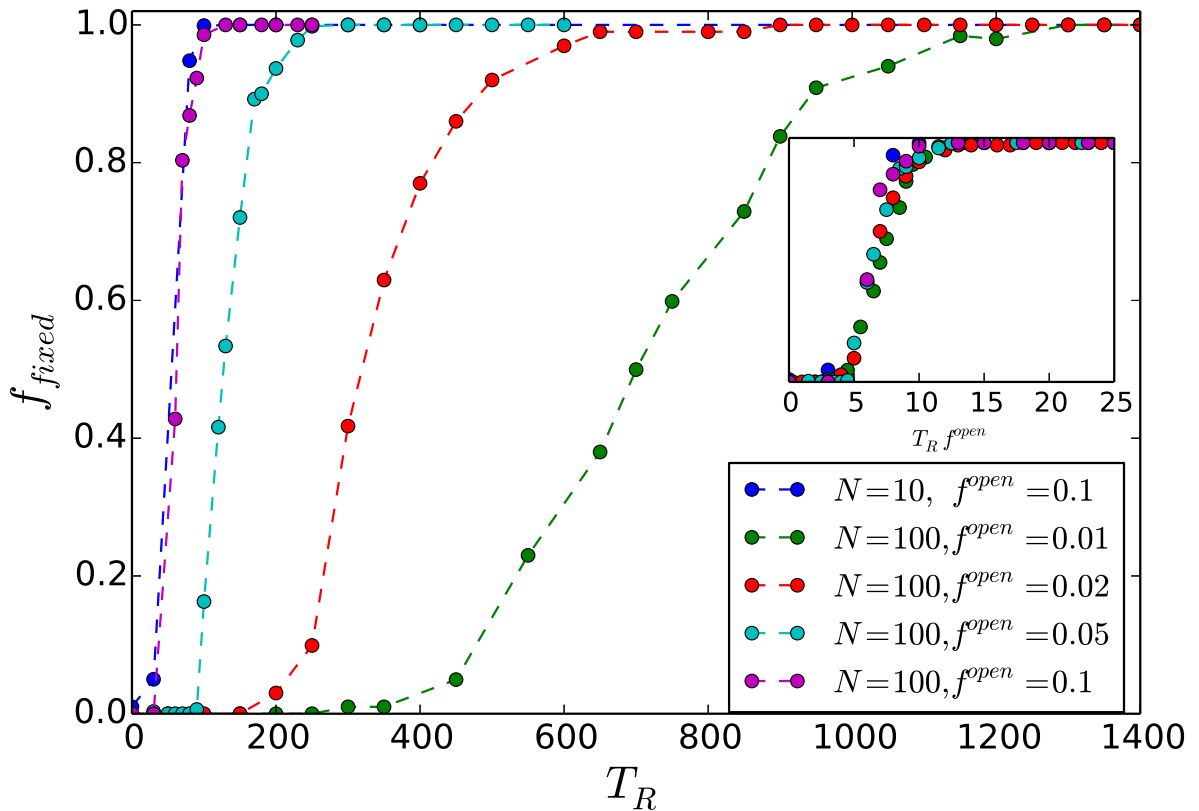


Figure 4.14: Fraction of nodes in the network that go to steady states, denoted by $f_{fixed}$, with respect to the redistribution time $T_R$. Here $f_{fixed}$ is averaged over different network configurations and initial states, $x_c = 0.5$ and the fraction of open nodes $f^{open}$ in the network is $0.01, 0.02, 0.05, 0.1$ for $N = 100$ (i.e. $1, 2, 5, 10$ open nodes in the network respectively) and $0.1$ for $N = 10$ (i.e. 1 open node in the network). *Inset*: data collapse indicating the scaling relation $f_{fixed} \sim g(T_R f^{open})$.

Next we examine the *range of threshold values yielding steady states*, averaged over a large sample of network configurations and initial states, denoted by $\langle R \rangle$. Larger $\langle R \rangle$ implies that steady states will be obtained in a larger window in $x_c$ space, thereby signalling a more robust control. We have explored the dependence of this quantity on redistribution time $T_R$, and also on the fraction of open nodes in the network, denoted by $f^{open}$. From Fig. 4.16 we see that the steady-state window in $x_c$ rapidly converges to $\sim 1$ (namely, the range $0 \leq x_c < 1$), as the number of open nodes increases. So the window yielding suppression of chaos is almost independent of the number of open nodes, after a sufficiently large fraction of open nodes. Also notice that there is a critical fraction of open nodes $f_c^{open}$, after which the network yields a non-zero range of steady states, namely $\langle R \rangle > 0$ for $f^{open} > f_c^{open}$.
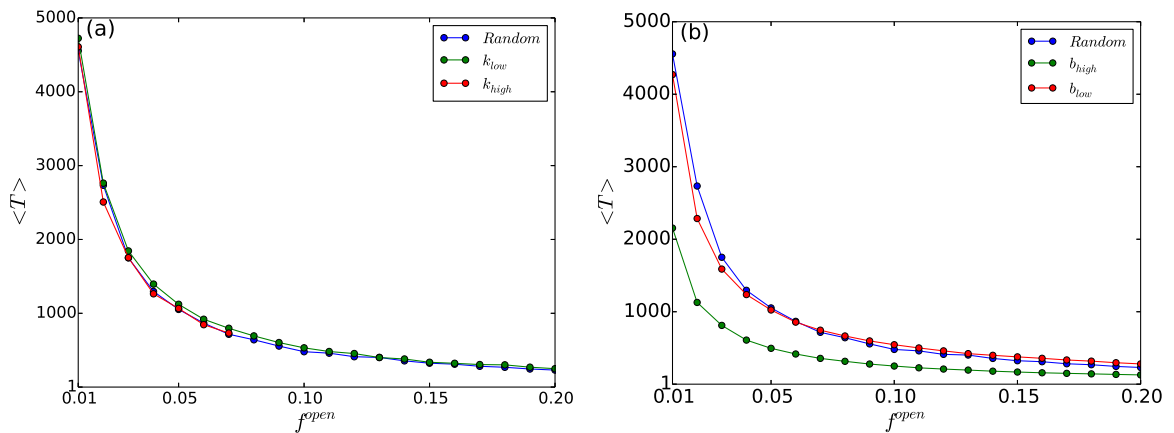


Figure 4.15: Average redistribution time $\langle T \rangle$, as a function of the fraction of open nodes in the network $f^{open}$. Here $\langle T \rangle$ is defined as the time taken for all nodes in the threshold-coupled Random Scale-Free Network of chaotic populations, to be under-critical (i.e. $x_i < x_c, \forall i$), averaged over a large sample of random initial states and network configurations. There are 100 chaotic populations connected via threshold-activated transport in a Random Scale-Free network. In panel (a) the case of open nodes chosen in descending order of degree starting from nodes with the highest $k$ (marked as $k_{high}$) and the case of open nodes chosen in ascending order of degree starting from nodes with the lowest $k$ (marked a $k_{low}$), are displayed. In panel (b) the case of open nodes chosen in descending order of betweeness centrality starting from nodes with the highest $b$ (marked as $b_{high}$) and the case of open nodes chosen in ascending order of betweeness centrality starting from nodes with the lowest $b$ (marked a $b_{low}$), are displayed. In both panels, the case of open nodes chosen at random is also shown for reference.
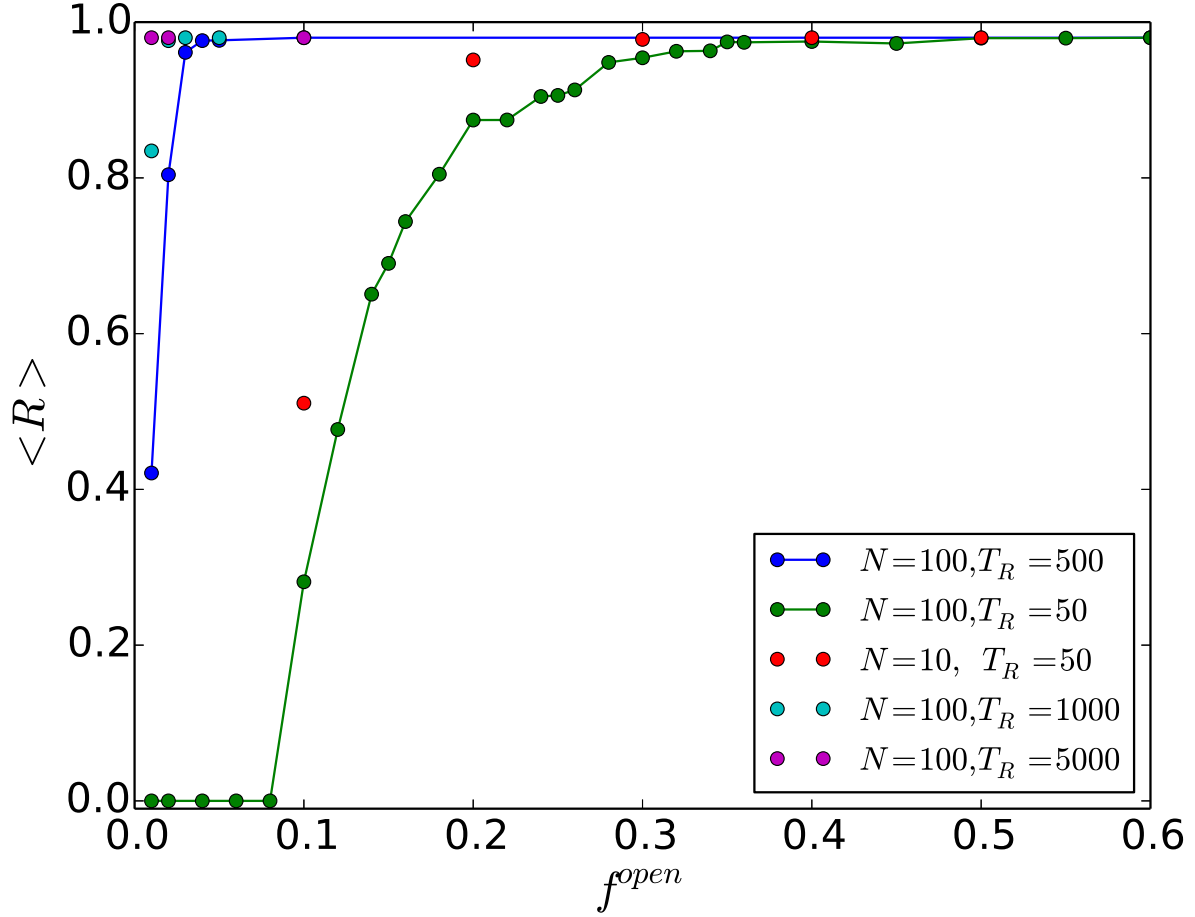
Figure 4.16: Range of threshold values that yield steady states, $\langle R \rangle$, as a function of the fraction of open nodes in the network $f^{open}$. Here $\langle R \rangle$ is averaged over different network configurations and initial states and the open nodes are randomly chosen. Results from different redistribution times ($T_R = 50, 500, 1000, 5000$) and system sizes ($N = 10, 100$) are shown.

We observe that $f_c^{open}$ tends to zero as the redistribution time increases and system size decreases, implying that *very few open nodes are necessary in order to lead the network to a steady state* [3] See:[73].

_____

[3]The transition to a global steady state after a critical fraction of open nodes is reminiscent of the effect of inactive elements at fixed states on a group of active elements in oscillatory states. In that situation too there was a transition to a macroscopic steady state, with respect to increasing number of inactive elements, at a critical value of inactive nodes.
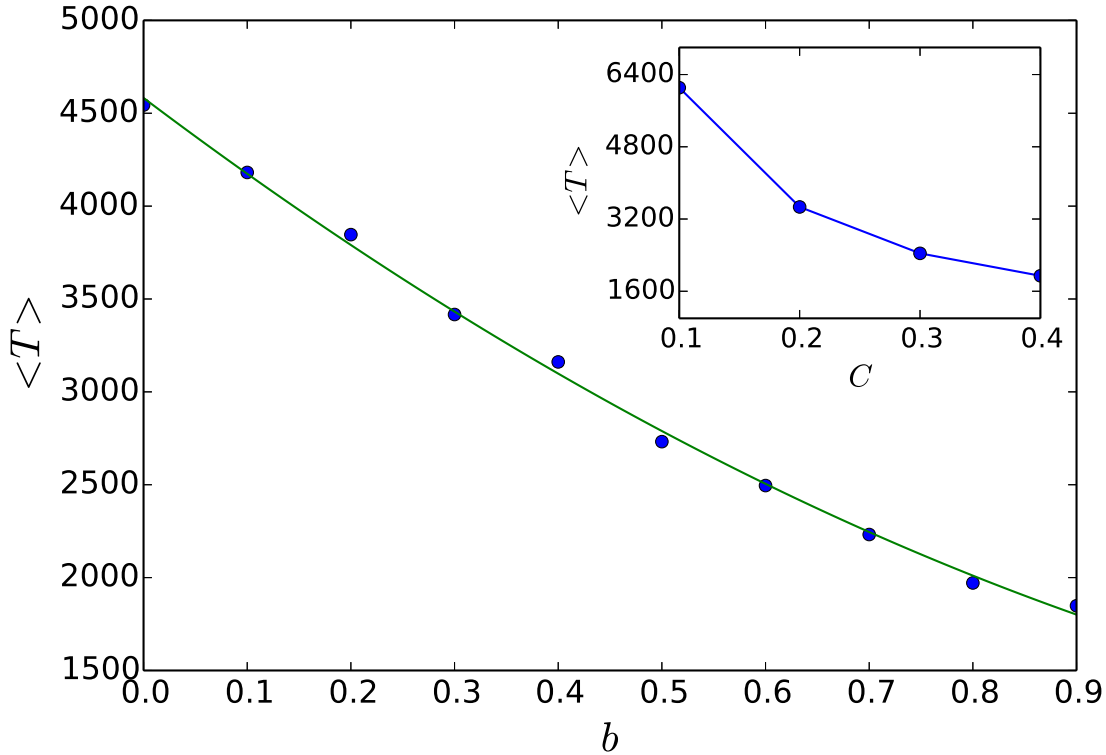
Figure 4.17: Average redistribution time $\langle T \rangle$, as a function of the betweeness centrality $b$ of the open node. Here $\langle T \rangle$ is defined as the time taken for all nodes in the threshold-coupled Random Scale-Free Network of chaotic populations, to be under-critical (i.e. $x_i < x_c, \forall i$), averaged over a large sample of random initial states and network configurations, in a network with a single open node. The solid curve shows the best quadratic polynomial fit. *Inset*: Average redistribution time $\langle T \rangle$, as a function of the closeness centrality $C$ of the open node.

One can understand these observations by noting that $f_c^{open}$ is determined by the time available to the system for threshold-activated transport (i.e. $T_R$), and the system size $N$. Now, as mentioned earlier, the average redistribution time needed for all nodes in a system to be under-critical, which reflects the time taken by the excess from any over-critical node in the network to reach some open edge, should scale with the diameter of the random scale-free network. This is known to scale with network size as $\ln N$. Further, note that not all nodes are open, and so the probability of reaching an open edge is inversely proportional to $f^{open}$. This implies that it takes longer to move all the excess to the open node(s) when $f^{open}$ is smaller. In order to reach a steady state the average time for cascades to cease should be less than the available time $T_R$. So if the

available redistribution time $T_R$ is low, and the network size $N$ is large, the cumulative excess from all the over-critical nodes in the system will not manage to reach the open edge. So no steady states will emerge (i.e. $\langle R \rangle = 0$). However, once $f^{open} > \ln N / T_R$, a global steady state will emerge. This offers as estimate of $f_c^{open}$. For instance, for $N = 100$ and $T_R = 50$, this argument suggests that $f_c^{open} \sim 0.09$, which is close to the numerically obtained value. This also implies that for sufficiently large redistribution time, or small enough network size, the system can attain steady state even when there is a *single* open node (i.e. $f_c^{open} \to 0$). In fact we can also obtain an estimate for the minimum $T_R$, which we denote as $T_R^{min}$, necessary for allowing the network to reach a steady state with just a single open node, namely $f_c^{open} = 1/N$. So for networks of size $N = 100$ one obtains $T_R^{min} \sim N \ln N \sim 460$, while for networks of size $N = 10$ one obtains $T_R^{min} \sim 23$. This estimate is consistent with the numerical results shown in Fig. 4.16, from where it is clear that for when $T_R > T_R^{min}$, e.g. for $N = 10, T_R = 50$ and for $N = 100, T_R = 500, 1000, 5000$, $\langle R \rangle$ is always non-zero, while for $N = 100, T_R = 50$ (i.e. when $T_R < T_R^{min}$) $\langle R \rangle = 0$ for $f^{open} < f_c^{open}$, after which there is a transition to non-zero $\langle R \rangle$.

Lastly we explore the scenario of very few open nodes ($f^{open} << f_c^{open}$) in greater depth, through the quantitative measures $\langle R \rangle$ and $\langle T \rangle$. In particular, we investigate the limiting case of a *single* open node. Our attempt will be to understand the influence of the degree $k$ and betweeness centrality $b$ of the open node on the capacity to suppress chaos. We have already observed the significant effect of the betweeness centrality of the open node on the efficiency of control to steady states through bifurcation diagrams in Fig. 4.12. This is now further corroborated quantitatively by the dependence of $\langle R \rangle$ and $\langle T \rangle$, displayed in Figs. 4.17 and 4.18(b). The effect of the degree of the open node is less pronounced, though it also does have a discernable effect on the suppression of chaos. As evident from Fig. 4.18(a), when the open node has a higher degree, it has a higher $\langle R \rangle$, indicating that open nodes with higher degree yield larger steady state windows.

Finally, note that the different centrality measures are most often strongly correlated and therefore do not offer new insights. For instance, we have also studied the network with respect to open nodes of varying closeness centrality, where closeness centrality is the average length of the shortest path between the node and all other nodes in the graph. We find that qualitatively same broad trends emerge with respect to closeness centrality, as observed for betweenness centrality (cf. Fig. 4.17 and its inset).

These results can be understood intuitively as follows: the emergence of steady states is crucially dependent on the efficacy of the excess being transported out of the network.

Namely, excess population from any over-critical node in the network needs to reach an open node within $T_R$ steps. So if an open node has high degree transport of excess is facilitated, as the excess can flow to the node simultaneously through its many links. Further one can rationalize the effect of the betweeness centrality of an open node on the stabilization of the steady state, as betweeness is a measure of centrality in a graph based on shortest paths. If an open node has high betweenness centrality, a large number of shortest paths pass through it. This naturally aids the cascading process, as excess reaches the open node in fewer time steps. The trends expected from these arguments are corroborated in the results from simulations shown in Figs. 4.17 and 4.18.
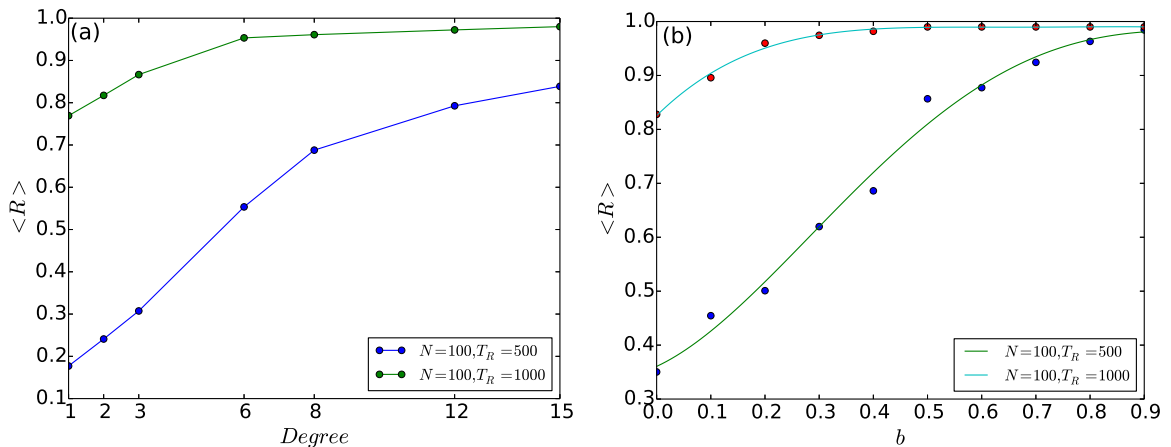


Figure 4.18: Range of threshold values that yield steady states $\langle R \rangle$, as a function of the (a) degree $k$, and (b) betweeness centrality $b$, of the open node. Here $\langle R \rangle$ is averaged over different network configurations and initial states, in a network with a single open node, (with the solid curve showing the best quadratic polynomial fit).

## 4.5 Conclusions

We have explored Random Scale-Free networks of populations under threshold-activated transport. Namely we have a system comprising of many spatially distributed sub-populations connected by migrations triggered by excess population density in a patch. We have simulated this threshold-coupled Random Scale-Free network of populations, under varying threshold levels $x_c$. We considered networks with varying number of open nodes, namely systems that have different nodes/sites open to the environment from where the excess population can migrate out of the system. Further, we have studied a range of redistribution times $T_R$, capturing different timescales of migration vis-a-vis population change.

Our first important observation is as follows: when redistribution time $T_R$ is large and the critical threshold $x_c$ is small ($0 \leq x_c < 1$), we have very efficient control of networks of chaotic populations to steady states. This suppression of chaos and quick evolution to a stable steady states occurs irrespective of the number of open nodes. Further, for threshold values beyond the window of control to fixed states, one obtains cycles of period 2. Namely for threshold levels $1 < x_c < 2$ the populations evolve in regular cycles, where low population densities alternate with a high population densities. This behaviour is reminiscent of field experiments [71] that show the existence of alternating states. We offer an underlying reason for this behaviour through the analysis of a single threshold-limited map.

For small redistribution time $T_R$, the system does not get enough time to relax to under-critical states and so perfect control to steady states may not be achieved. Importantly, now the number of open nodes is crucial to chaos suppression. We clearly demonstrate that when there are enough open nodes, the network relaxes to the steady state even for low redistribution times. So more open nodes yields better control of the intrinsic chaos of the nodal population dynamics to fixed populations. We corroborate all qualitative observations by quantitative measures such as average redistribution time, defined as the time taken for all nodes in a system to be under-critical, and the range of threshold values yielding steady states.

We also explored the case of networks with very few (typically 1 or 2) open nodes in detail, in order to gauge the effect of the degree and betweenness centrality of these open nodes on the control to steady states. We observed that the degree of the open node does not have significant influence on chaos suppression. However, betweenness centrality of the open node is important, with the region of control being large when the open node has the high betweenness centrality, and vice versa.

The emergence of steady states in this system, not only suggests potential underlying mechanisms for stabilization of intrinsically chaotic populations, but also has bearing on the broad problem of control in complex networks. When a steady state is the desired state of the nodal populations in the network, the threshold mechanism offers a very simple and potent strategy for achieving this, as we have demonstrated clearly. If the aim is to prevent steady states, as may be the case in variants of this model relevant to neuronal dynamics, our results suggest what threshold levels need to be avoided in order to prevent evolution to global fixed points. Note that a large class of control strategies entail complicated algorithms to calculate feedback, and these require knowledge of the global network topology and details of the network dynamics, which are often unknown.

Here on the other hand, the nodes respond independently at the local level to a simple threshold limiter condition, requiring knowledge of only the local state at any point in time.

Lastly, interestingly, analogs of this class of coupling have been realized in CMOS circuit implementation using pulse-modulation approach [74, 75]. So some of these results may be of potential interest to the engineering community as well. In the biological context, some experiments have studied similar dynamics in replicate laboratory metapopulations of Drosophila [76]. So our results have the potential to be demonstrated in extensions of such experiments in the future.

In summary, threshold-activated transport yields a very potent coupling form in a network of populations, leading to robust suppression of the intrinsic chaos of the nodal populations on to regular steady states or periodic cycles. So this suggests a mechanism by which chaotic populations can be stabilized rapidly through migrations or dispersals triggered by excess population density in a patch.

# Chapter 5

# Robustness of networks of multi-stable chaotic systems to targetted attacks

# 5.1　Introduction

Collective spatiotemporal patterns emerging in dynamical complex systems are determined by the interplay of the dynamics of each node and the nature of the interactions among the nodes. Interactions among nodes are often modelled by interesting coupling topologies and coupling forms, and these interactions influence spatiotemporal pattern formation in the network. So it is of utmost relevance to ascertain how significantly the properties of an individual node impact the collective dynamics of a network. The influence of a node on the dynamics of a network depends on how much information flows through this node and how critical the node is to that flow. Understanding this significance will allow us to determine which nodes render the network most susceptible to external influences. Alternately, it will potentially suggest which nodes to protect more stringently from perturbations in order to protect the dynamical robustness of the entire network.

In particular, we consider three properties of the nodes, and try to correlate these with the robustness of the collective dynamics. The three nodal features we focus on are the following:

(i) Normalized degree of a node $i$ in an undirected network: this is given by the number of neighbors that are directly connected to the node scaled by the total number of nodes $N$, and is denoted by $k_i$. So a high degree node indicates that there is direct contact with a larger set of nodes.

(ii) Normalized betweeness centrality of a node $i$ [77, 78]: this is defined as

$$b_i = \frac{2}{(N-1)(N-2)} \sum_{s,t \in I} \frac{\sigma(s,t|i)}{\sigma(s,t)}$$

where $I$ is the set of all nodes, $\sigma(s,t)$ is the number of shortest paths between nodes $s$ and $t$ and $\sigma(s,t|i)$ is the number of shortest paths passing through the node $i$. So if node $i$ has high betweeness centrality, it implies that it lies on many shortest paths, and thus there is high probability that a communication from $s$ to $t$ will go through it.

(iii) Normalized Closeness Centrality: this is defined as

$$c_i = \frac{N-1}{\sum_j d(j,i)}$$

where $d(j,i)$ is the shortest path between node $i$ and node $j$ in the graph. Namely, it is

the inverse of the average length of of the shortest path between the node and all other nodes in the network[79]. So high closeness centrality indicates short communication path to other nodes in the network, as there are minimal number of steps to reach other nodes.

Since the above features of a node determine the efficiency of information transfer originating from it, or through it, they are expected to influence the propagation of perturbations emanating from the node. As a test-bed for understanding this we consider the collective dynamics of a group of coupled Duffing oscillators in this Chapter. First we analyse the dynamical behaviour of the Duffing oscillators and identify the parameter values where co-existing attractors are present. We look for both coexisting limit cycles, as well as coexisting chaotic attractors. We will then go on to explore pattern formation in such multi-stable Duffing oscillators, connected in star, ring and random scale-free networks.

In an earlier work [80] we had investigated the basin stability of the synchronized state in networks of coupled bi-stable elements. That is, we considered dynamical systems with two co-existing fixed points, coupled in different network topologies. Our focus was the stability of the collective state where all the elements were in the same well, i.e. in the vicinity of the same fixed point attractor. The central result of that study was that the *betweeness centrality of the perturbed node was most crucial for dynamical robustness*, and influenced the stability of the network much more strongly than closeness centrality or degree of the perturbed node. This result will potentially help us decide which nodes to safeguard in order to maintain the collective state of this network against targetted localized attacks. In this chapter we will exploit the fact that the Duffing oscillator has multi-stable attracting states that are dynamically more complex, such as co-existing limit cycles and chaotic attractors, unlike previous studies where the co-existing states were all fixed points. So we will use the Duffing system as a test-bed to *generalize* our earlier results from networks of fixed point attractors to networks of more complex dynamical attractors. Also note that in this Chapter a "synchronized state" will imply one where all nodes in the network are in the basin of attraction of the same attractor of the multi-stable oscillator. So it does not imply complete synchronization. Rather, the constituent oscillators inhabit the same region of phase space, associated with the basin of one, or the other, of the coexisting dynamical states.

To gauge the global stability and robustness of a state, we will *introduce a variant of the recent framework of multi-node basin stability* [81]. In general, the basin stability of a particular attractor of a multi-stable dynamical system is given by the fraction of

perturbed states that return to the basin of the attraction of the dynamical state under consideration. We will first discuss some concepts we will use to assess the effect of different nodal properties on the resilience of a network. At the outset we will consider all nodes of the network localized on one of the two stable attractors, i.e. $\{x_i, y_i\}$ of all nodes $i$ lie on different phase-space points of one of the attractors. We then give a large perturbation to some fraction of nodes, denoted by $f$. We consider three distinct types of perturbations:

(i) Perturbations onto another Attractor (P1): here we perturb the nodes on to randomly chosen phase-space points lying on a different attractor. For instance, for the case of Duffing oscillators with two co-existing limit cycles, if the initial states of the nodes in the network are localized on the attractor with negative $x$ values (cf. Fig 5.2(d)), then the perturbed nodes will lie on the limit cycle with positive $x$ values (cf. Fig 5.2(b)).

(ii) Perturbations onto a small phase-space volume in the basin of attraction of another co-existing attractor (P2).

(iii) Perturbations randomly chosen in a large phase-space volume (P3) : This type of perturbation is most commonly used in previous studies. For instance, for the case of coupled Duffing oscillators we perturb the nodes onto a randomly chosen phase-space point in the phase-space box $x \in [-1 : 1]$ and $y \in [-1 : 1]$.

After perturbations, we check whether all the oscillators return to their original attractors, i.e. if the perturbed system recovers completely to the initial state. We repeat this "experiment" over a large sample of perturbed nodes and perturbations strengths, and find the fraction of times the system manages to revert to the original state. This measure of global stability is then a variant of multi-node basin stability and it is indicative of the robustness of the collective state to perturbations localized at particular nodes in the network. It reflects the fraction of the volume of the state space of a sub-set of nodes that belong to the basin of attraction of the synchronized state. The importance of this concept stems from the fact that it determines the probability of the system to remain in the basin of attraction of the synchronized state when random perturbations affect a specific number of nodes. *This allows us to extract the contributions of individual nodes to the overall stability of the collective behaviour of the dynamical network.* Further, since one perturbs subsets of nodes with certain specified features, our variant of multi-node BS will suggest which nodal properties make the network more vulnerable to attack.

So the focus of this chapter will be to examine the global stability of a network of cou-

pled multi-stable nonlinear systems with co-existing limit cycles and co-existing chaotic attractors. Specifically we will investigate Duffing oscillators in the multi-stable regime, coupled in different network topologies. First we will analyze the dynamics of single Duffing oscillator and then we will explore collective behaviour and multi-node basin stability of different networks of Duffing oscillators, under the three above mentioned classes of perturbations. The central question we will investigate here is the following: *what are the effects of the characteristics of the perturbed nodes on the global stability of the network?* So we will search for discernable patterns amongst the nodes that aid the maintenance of the stability of the collective dynamics of the network on one hand, and the nodes that rapidly destroy it on the other. That is, we will explore the extent to which the features of the nodes, given by its degree and centrality properties, influences the recovery of a network from large localized perturbations.

## 5.2  Study of the single Duffing Oscillator

First we analyze the dynamical behaviour of single Duffing oscillator, under varying parameter values and initial conditions. This analysis will be helpful in understanding the problem of networks of coupled Duffing oscillators.

The Duffing oscillator is governed by the nonlinear second order differential equation given by Eqn. 5.1. Associating $\dot{x} = y$ gives:

$$
\begin{aligned}
f_x(x,y) &= y \\
f_y(x,y) &= -(\delta y + \alpha x + \beta x^3) + a\,sin(\omega t)
\end{aligned}
\tag{5.1}
$$

Where $\delta$ controls the amount of damping, $\alpha$ control the linear stiffness, $\beta$ controls the amount of nonlinearity in the resorting force, $a$ is the amplitude and $\omega$ is the angular frequency of the periodic driving force. Here we consider parameter values $\alpha = 1$, $\delta = 0.5$, $\beta = -1$ and $\omega = 1$, and we vary the amplitude of the periodic driving force given by parameter $a$.
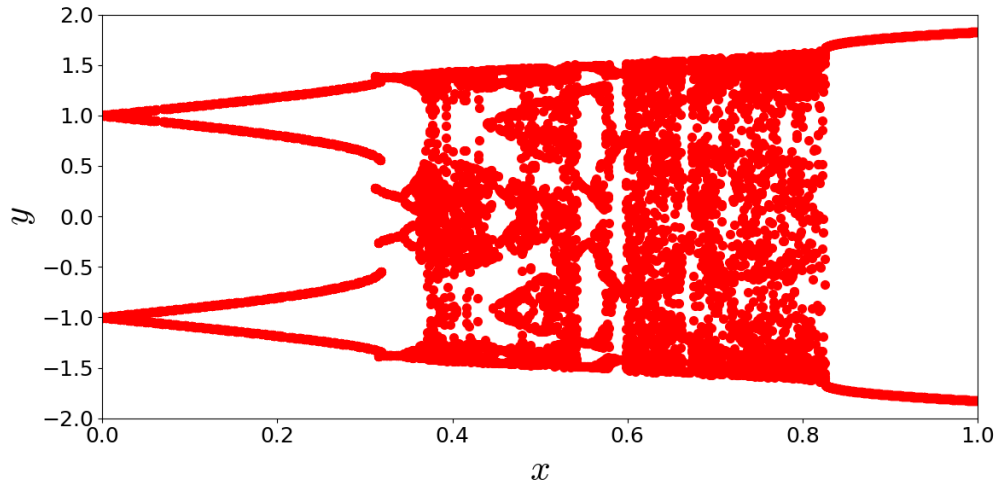
Figure 5.1: Bifurcation diagram of the state of the Duffing oscillator given by Eqn. 5.1 (with the $x$-variable displayed), as a function of amplitude of periodic forcing $a$.



(a)



(b)



(c)



(d)
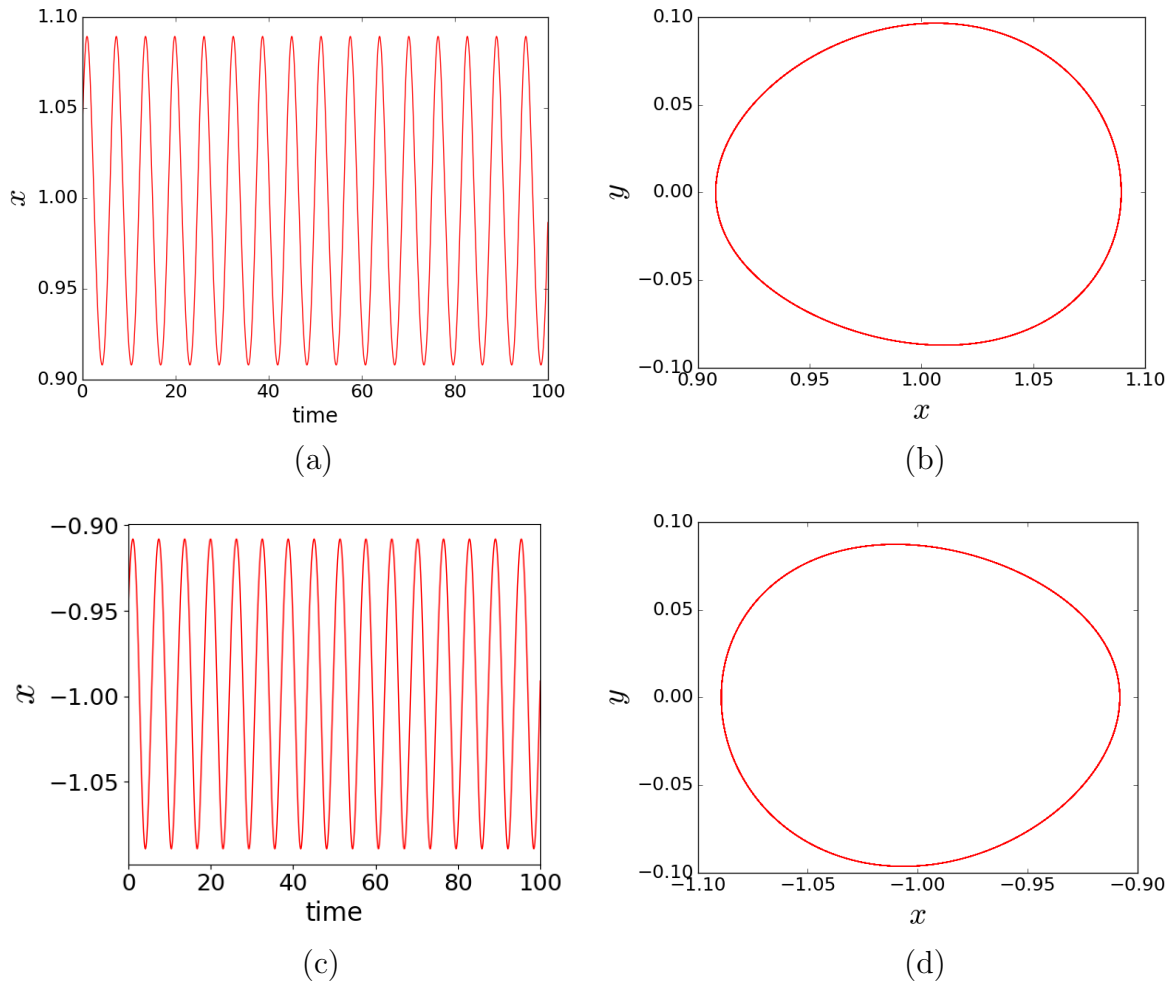
Figure 5.2: Time series and phase portraits of the single Duffing oscillator for $a = 0.1$, evolving from different initial conditions.

The Duffing oscillator displays rich dynamics of multi-stable limit cycle and chaos, as evident from its bifurcation diagram (cf. Fig. 5.1). Importantly, we find that there is coexistence of limit cycles in the parameter range $0 < a < 0.35$, co-existence of chaotic attractors in the range $0.35 < a < 0.85$ and a single limit cycle attractor for $0.85 < a < 1$. Time series and phase portraits of the co-existing limit cycles are displayed in Fig. 5.2, the co-existing chaotic attractors in Fig. 5.3, and the single limit cycle in Fig. 5.4. So it is clearly evident that the Duffing oscillator is a multi-stable system, with co-existing attractors bounded in distinct regions of phase space.
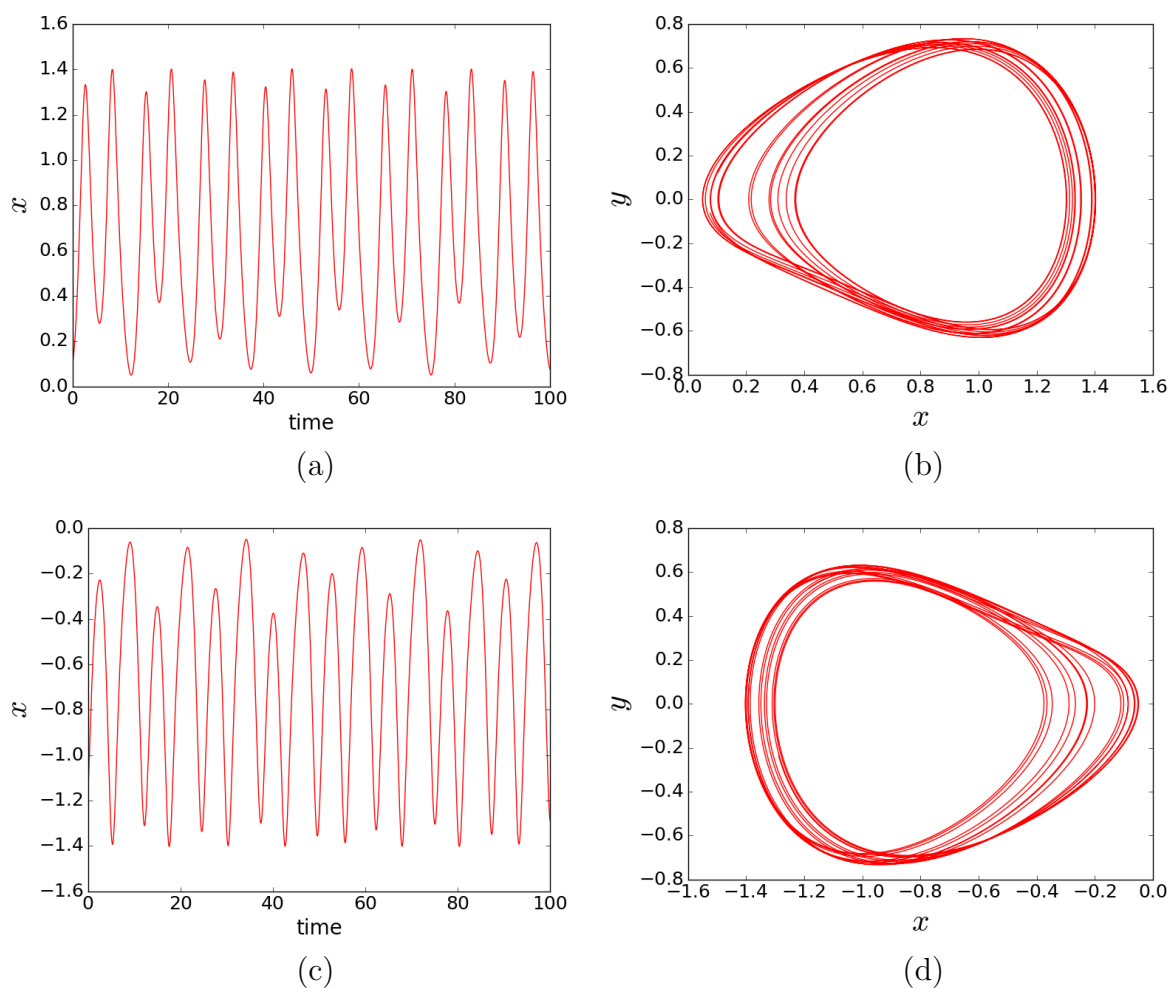


Figure 5.3: Time series and phase portraits of the single Duffing oscillator for $a = 0.36$, evolving from different initial conditions.

In order to quantitatively characterize the nature of the multi-stable dynamical states, we explore the basin volume of the co-existing limit cycle and chaotic attractors. It is evident from the basins of attraction shown in Fig. 5.5 that the basin volume for the co-existing limit cycles for $a = 0.1$ is different from the basin volume for the co-existing

95

chaotic attractors for $a = 0.36$, with the basin boundary being more complex for co-existing chaotic attractors.



(a)

(b)
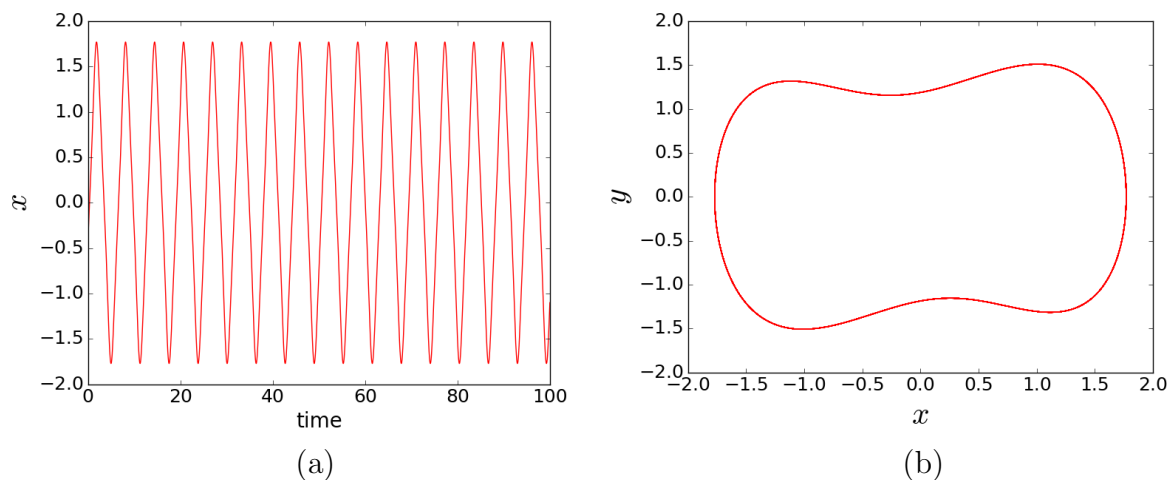
Figure 5.4: Time series and phase portrait of the single Duffing oscillator for $a = 0.9$.



(a)

(b)
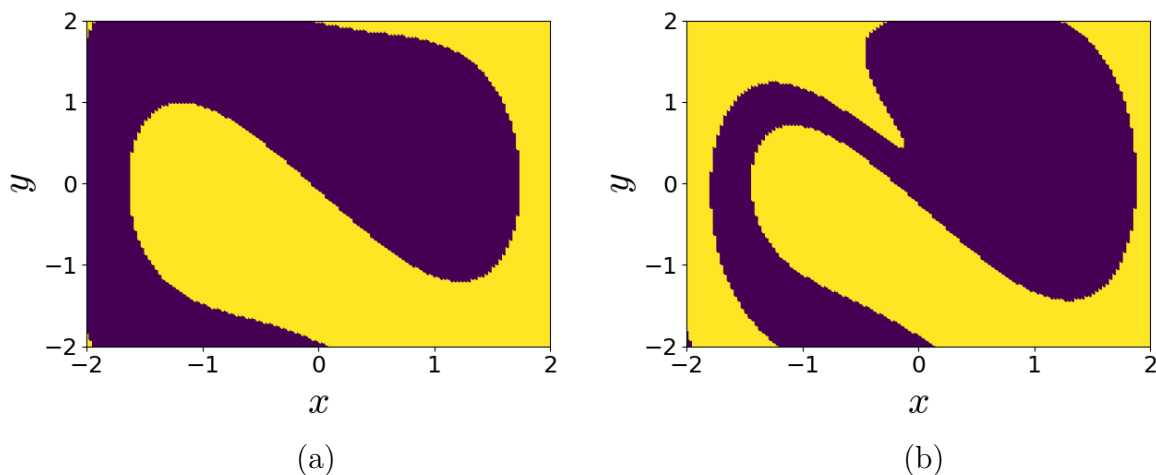
Figure 5.5: Basins of attraction of a single Duffing oscillator with (a) $a = 0.1$ and (b) $a = 0.36$. The purple color indicates the results for one type of attractor and the yellow color represents a different co-existing attractor.

## 5.3 Coupled Oscillators

Now we consider a mean-field diffusive coupled network of Duffing oscillators. The general form of a coupled system comprised of the local dynamics, and the coupling interactions, is given as:

$$\dot{x}_i = f_x(x_i, y_i) + C\frac{1}{K_i}\sum_j (x_j - x_i) = f_x(x_i, y_i) + C(\langle x_i^{nbhd}\rangle - x_i) \qquad (5.2)$$

$$\dot{y}_i = f_y(x_i, y_i)$$

where index $i$ specifies the site/node in the network, with $i = 1, \ldots N$, where $N$ is the size of the network. $C$ is the coupling constant reflecting the strength of coupling. The set of $K_i$ neighbours of node $i$ depends on the topology of the underlying connectivity, and this form of coupling is equivalent to each site evolving diffusively under the influence of a "local mean field" generated by the coupling neighbourhood of each site $i$, $\langle x_i^{nbhd}\rangle = \frac{1}{K_i}\sum_j x_j$, where $j$ is the node index of the neighbours of the $i^{th}$ node, with $K_i$ being the total number of neighbours of the node. In this work, the isolated dynamics at each node/site of the network is given by the Duffing oscillator (cf. Eqn. 5.1).

## 5.3.1 Random Scale-Free network of multi-stable Duffing oscillators

We will first investigate Random Scale-Free (RSF) Networks of Duffing oscillators. Specifically, we construct these networks via the Barabasi-Albert preferential attachment algorithm, with the number of links of each new node denoted by parameter $m$ [10]. In particular, we will show representative results for networks of size $N = 100$, with $m = 1$ and $m = 2$. For the nodal dynamics we will take the value of parameter $a = 0.1$ yielding co-existing limit cycles, and $a = 0.36$ yielding co-existing chaotic attractors. In the following sections we will explore the features of the perturbed nodes which influence the recovery of a network from large localized perturbations under the three perturbations schemes (P1, P2, P3) mentioned above.

### Perturbations onto another Attractor (P1)

Here we consider the initial states of the nodes to be randomly distributed on the attractor with negative $x$, and the perturbed nodes to be on the other attractor with positive $x$. Nodal dynamics with co-existing limit cycles, as well as chaotic attractors will be studied. First we explore the influence of the *fraction f of perturbed nodes* on the collective dynamics of oscillators in a network. We investigate this dependence, through space-time plots and phase space plots of the networks with varying number of perturbed

nodes. Here nodes with the highest betweeness centrality are chosen for perturbation. From Figs. 5.6, 5.7 and 5.8 we observe the following: when the fraction of perturbed nodes is relatively small ($f < 0.2$), then these perturbed nodes return to their original states, and remain synchronized with the other oscillators. When there are moderately large number of perturbed nodes, then the perturbed nodes switch their states to other attractor and also disturb the stability of some other oscillators dragging them to the other attracting state. When the number of perturbed nodes reach a critical value, then *all* oscillators switch from their original attractor to the other attractor, i.e. all the oscillators move from the negative attractor to the positive one. So one can say that as the fraction of perturbed nodes increases, the stability of one synchronized state (where all oscillators are in the negative state, in our example) is lost, while another synchronized state (where all oscillators are in the positive state) gains stability. This transition occurs via a short range of co-existence of these two synchronization states. The important question then is as follows: what is the critical fraction of perturbed nodes needed for loss of dynamical robustness, for different types of dynamical attractors. In order to answer this question, we will first analyse the case of co-existing limit cycles and then we go on to the case of co-existing chaotic attractors.

We will now present the dependence of the global stability of the collective dynamics on different centrality measures in this heterogeneous network, quantitatively, through multi-node basin stability measures. In particular, in order to explore the correlation between a given centrality measure of the nodes and the resilience of the system, we will estimate the multi-node basin stability under perturbations on sub-sets of nodes with increasing (or decreasing) values of the centrality under consideration, starting from nodes with lowest (or highest) centrality. That is, we order the nodes according to the centrality we are probing, and consider the effect of perturbations on fraction $f$ of nodes with the highest (or lowest) centrality.

The influence of perturbations on nodes with the highest and lowest betweeness, closeness and degree centrality in a RSF network are displayed in Fig. 5.9a-c for the case of co-existing limit cycles and in Fig. 5.9d-f for the case of co-existing chaotic attractors. The broad trends are similar for all three centrality measures, as is intuitively expected. It is clearly evident from Figs. 5.9 that when nodes with the highest betweeness, closeness and degree centrality are perturbed, multi-node basin stability falls drastically. On the other hand, on perturbing the same number of nodes of low centrality results in the multi-node stability falling slowly. We also observe that for the case of co-existing limit cycles, when nodes of increasing closeness centrality, starting from nodes with lowest $c$, are perturbed (cf. Fig. 5.9b vis-a-vis 5.9a and Fig. 5.9c) the system loses stability at much

Figure 5.6: Time evolution of 100 Duffing oscillators coupled in a Random Scale-Free network with $m = 2$, given by Eqn. 5.2, with coupling strength $C = 1$ and $a = 0.1$. Here perturbed nodes are of highest betweeness centrality and the number of perturbed nodes are (a) 15, (b) 25, (c) 30 and in (d) 35.

lower $f$ than for the case where the perturbed have the lowest degree and betweeness centrality. This difference is also discernable for the case of co-existing chaotic attractors, though not as pronounced as in the case of co-existing limit cycles. The underlying reason for this lies in the marked difference in the probability distribution of the different centrality measures at the low end. For closeness centrality, the probability of finding nodes with low $c$ is very low. This is in contradistinction to the case for degree and betweeness, where the probability of finding nodes with low $b$ and $k$ is the highest.

Fig. 5.9 also shows the basin stability of a network where the perturbed nodes are randomly chosen, corresponding to *random attacks* on a subset of nodes. Clearly, a *targetted attack on nodes with high centrality can destroy the collective dynamics much more efficiently than random attacks.*

Now we will investigate two important questions. First, which property of the nodes
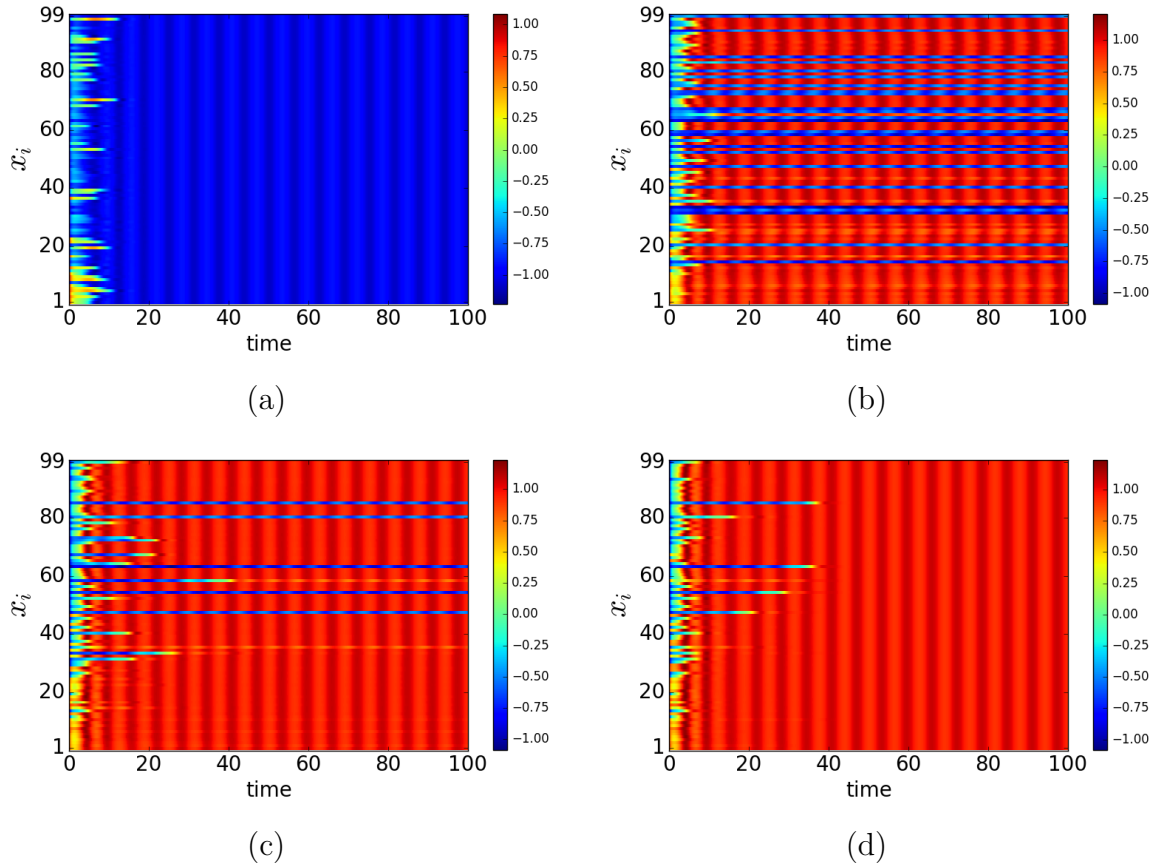
Figure 5.7: Phase portrait of 100 Duffing oscillators coupled in a Random Scale-Free network with $m = 2$, given by Eqn. 5.2, with coupling strength $C = 1$ and $a = 0.1$. Here perturbed nodes are of highest betweeness centrality and the number of perturbed nodes are (a) 15, (b) 25, (c) 30 and in (d) 35.

is most crucial in determining the global robustness of the synchronization state in the network of multi-stable Duffing oscillators? Secondly, is this property is independent of the dynamical nature of the attractors? To answer these questions we go through the following numerical experiment: we compare the basin stability of the collective dynamics of RSF networks with $m = 1$ and $m = 2$ for networks of Duffing oscillators with co-existing chaotic and limit cycle attractors, sampled over different nodal centrality measures.

Fig. 5.10 displays the dependence of the multi-node basin stability on the fraction of perturbed nodes $f$ in the RSF network with $m = 1$ and $m = 2$. For the limit cycle case, as number of perturbed nodes increases, the multi-node basin stability falls significantly for RSF networks with $m = 1$, while RSF networks with $m = 2$ remain robust up to
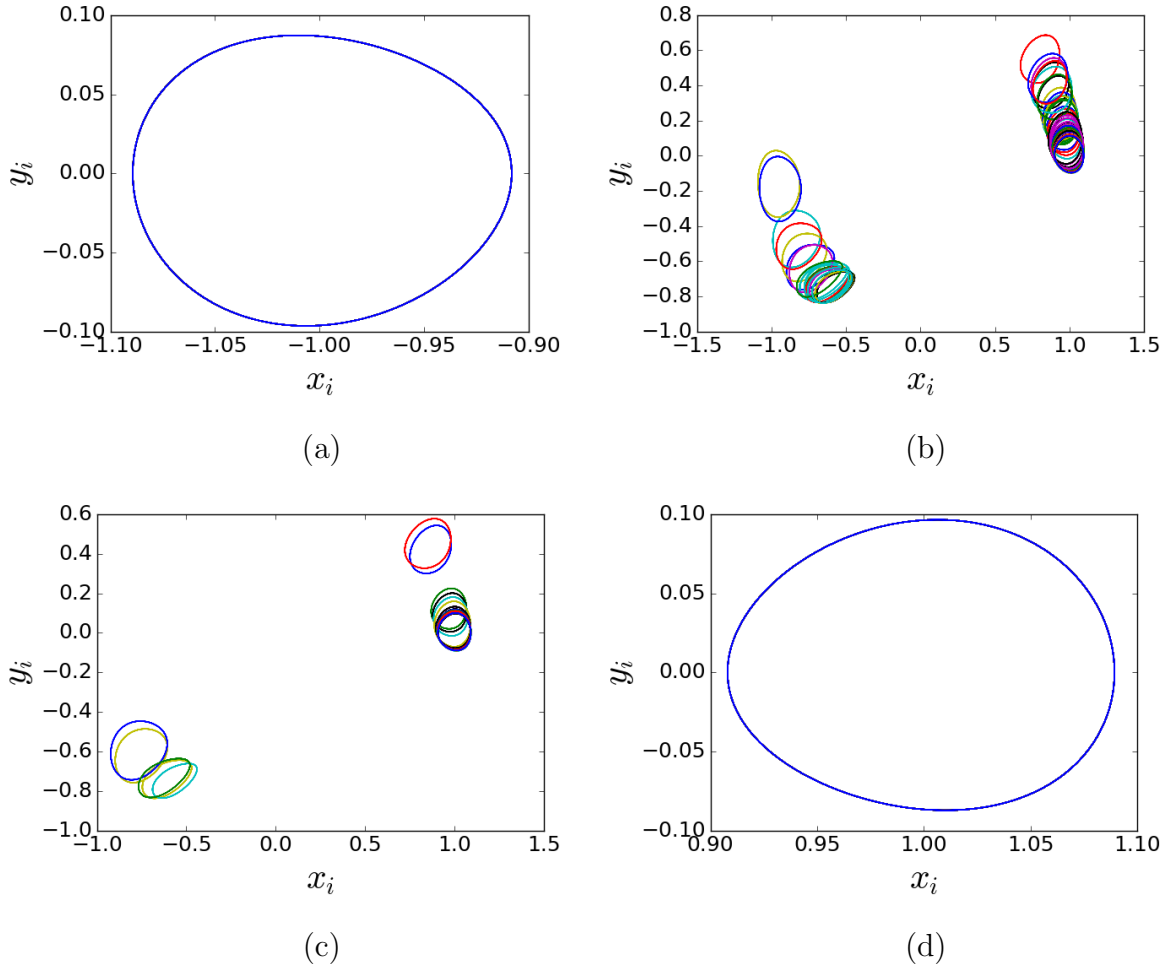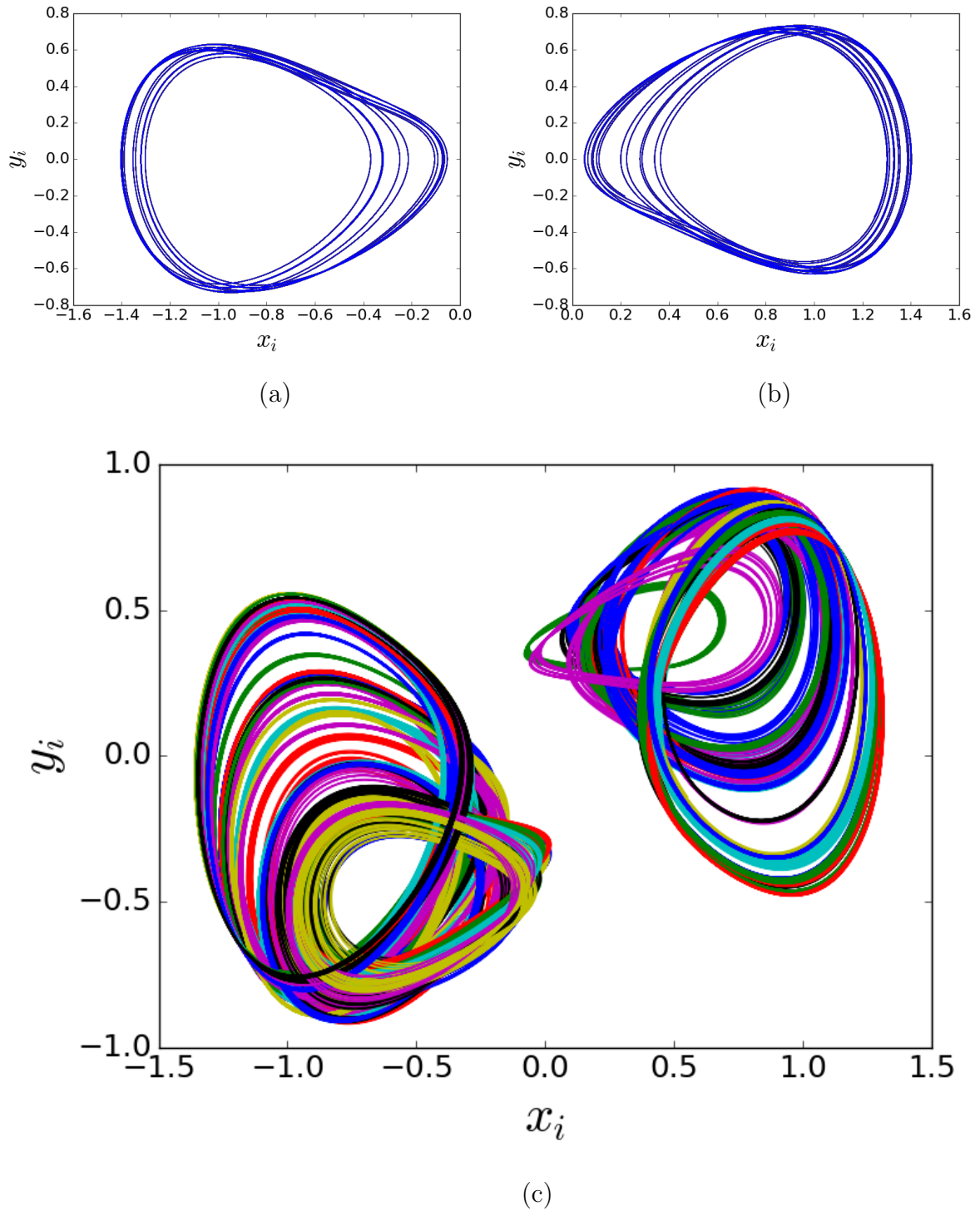
Figure 5.8: Phase portrait of 100 Duffing oscillators coupled in a Random Scale-Free network with $m = 2$, given by Eqn. 5.2, with coupling strength $C = 1$ and $a = 0.36$. Here perturbed nodes are of highest betweeness centrality and the number of perturbed nodes are (a) 25, (b) 80, (c) 40.
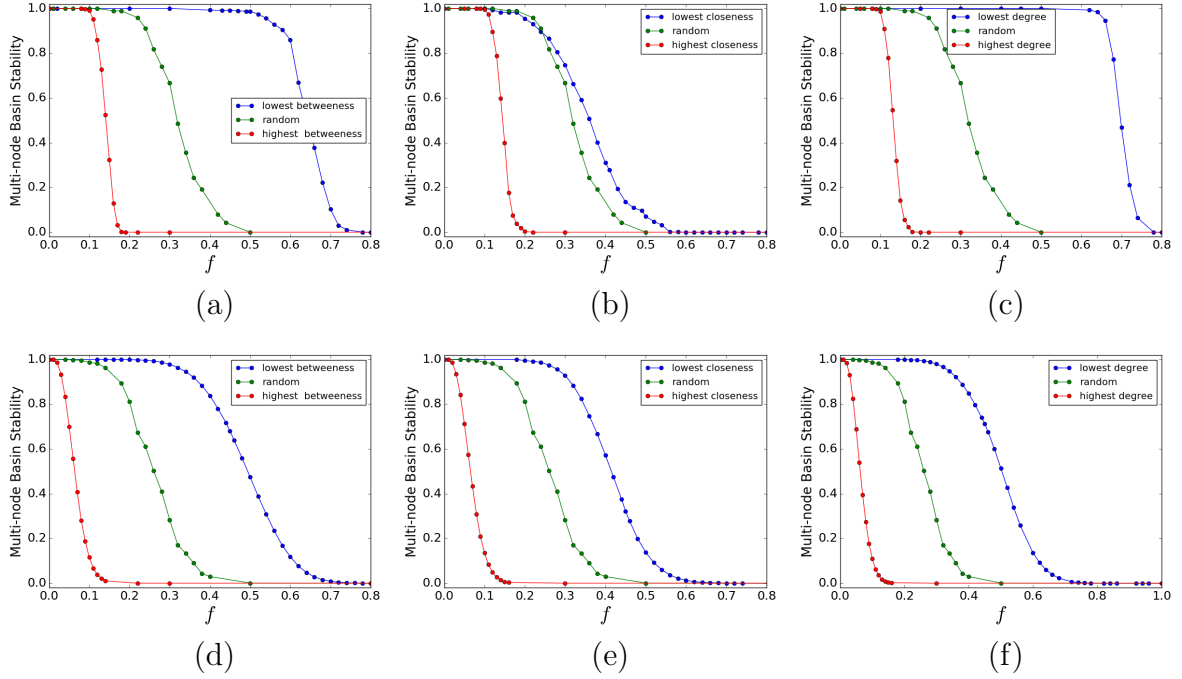
Figure 5.9: Dependence of the multi-node basin stability of Random Scale-Free networks of size $N = 100$, with $m = 2$ and $C = 1$, on the fraction of perturb nodes. For the top row (a,b,c) $a = 0.1$ and for the bottom row (d,e,f) $a = 0.36$. In the panels, three cases are shown. In the first case, the perturbed nodes are chosen at random (green curves). In the second case (red curves) the perturbed nodes are chosen in descending order of (a,d) betweeness centrality, (b,e) closeness centrality and (c,f) degree (i.e. the perturbed nodes are the ones with the highest $b$, $c$ or $k$ centrality measures). In the third case (blue curves) the perturbed nodes are chosen in ascending order of (a,d) betweeness centrality, (b,e) closeness centrality and (c,f) degree (i.e. the perturbed nodes are the ones with the lowest $b$, $c$ or $k$ centrality measures).

a critical fraction $f_{crit}$ of perturbed nodes, with $f_{crit} \sim 0.1$, For the case of co-existing chaotic attractors, as the fraction of perturbed nodes increases, the multi-node basin stability falls rapidly for RSF networks with $m = 1$ as well as $m = 2$. It is clearly evident from Fig. 5.10 then, that a *network of oscillators with co-existing limit cycles is much more robust than a network of oscillators with co-existing chaotic attractors.* So when nodes with high centrality are perturbed, the type of dynamics at the nodes plays a significant role in determining the global stability of the collective dynamics.

Lastly, we study the effect of system size on multi-node basin stability. Networks sizes ranging from 50 to 200 are studied, perturbing nodes in decreasing order of betweeness centrality. The results for networks of Duffing oscillators with co-existing limit cycles and co-existing chaotic attractors are displayed in Fig. 5.11a-b and Fig. 5.11c-d respectively. We observe that a Random Scale-Free network with limit cycle dynamics, yields $f_{crit} \to 0$
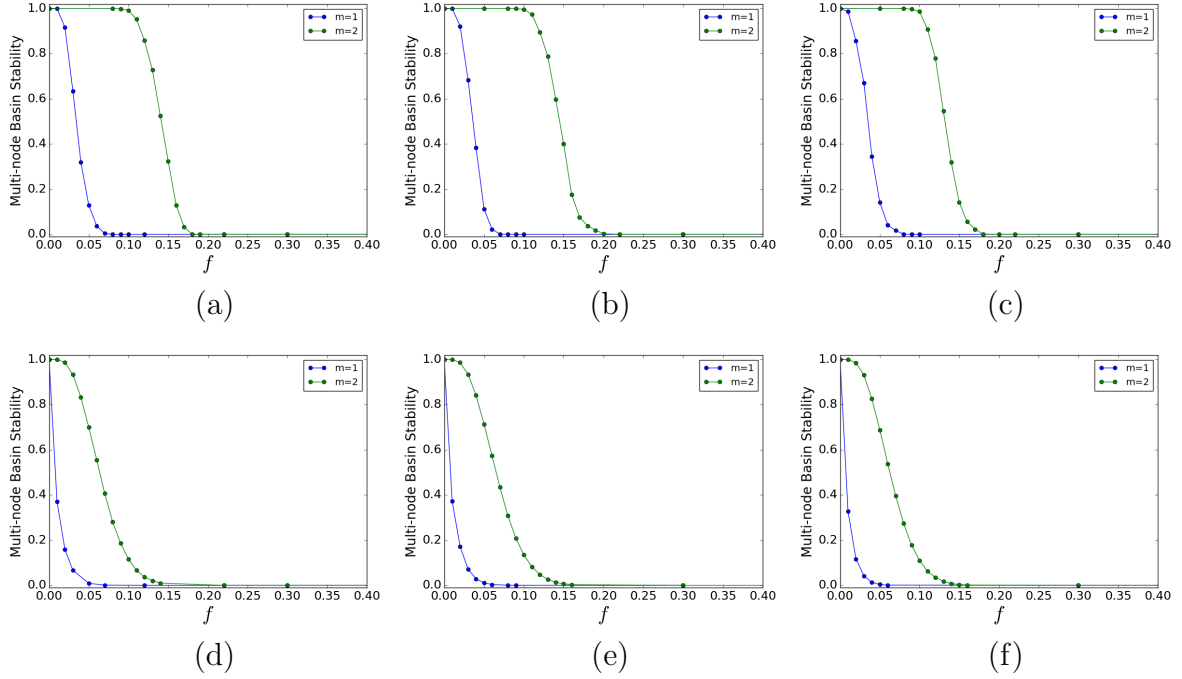
Figure 5.10: Multi-node basin stability vs fraction $f$ of nodes perturbed, for Random Scale-Free network of size $N = 100$, coupling strength $C = 1$, with $m = 1$ and $m = 2$, where the perturbed nodes are chosen in descending order of (a,d) betweeness centrality, (b,e) closeness centrality and (c,f) degree (i.e. the perturbed nodes are the ones with the highest $b$, $c$ or $k$ centrality measures). In the top row (a,b,c) $a = 0.1$ and $a = 0.36$ for the bottom row (d,e,f).

for $m = 1$ i.e. the smallest non-zero fraction of perturbed nodes destroy the collective state in this network. On the other hand, $f_{crit} \sim 0.1$ for the case of $m = 2$. So in the $m = 2$ case, even when nearly 10% of the nodes with the highest betweeness centrality are perturbed, the entire network still manages to return to the original state. This implies that a RSF network with $m = 2$ is more robust to localized perturbations than a network with $m = 1$. Notice though, that RSF networks of oscillators with co-existing chaotic attractors, are very sensitive to perturbations on the nodes with the highest centrality, for both $m = 1$ and $m = 2$. So the smallest fraction of perturbed nodes destroy the collective state in RSF networks with $m = 1$ and 2, when the dynamics is chaotic.
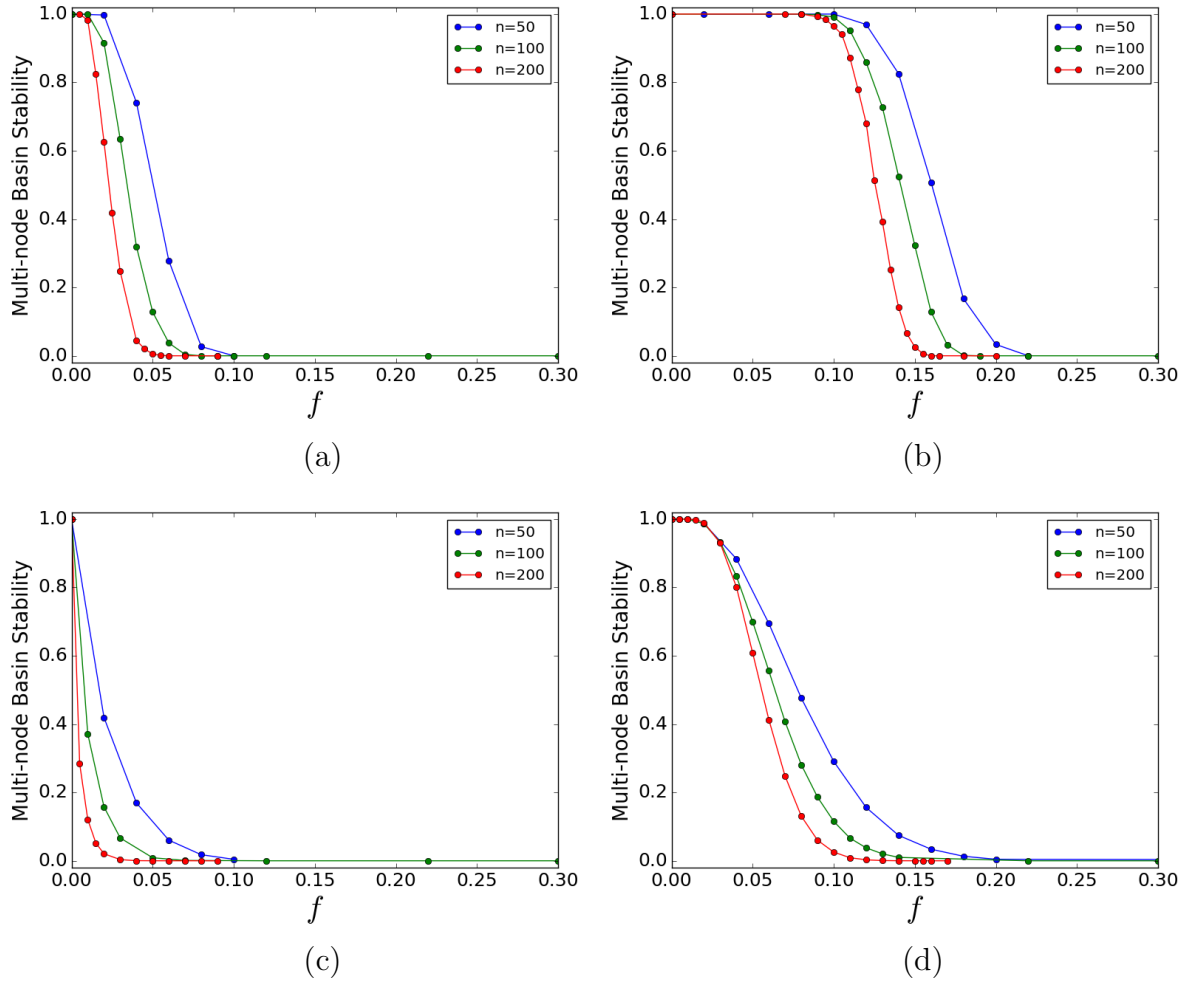
Figure 5.11: Multi-node basin stability vs fraction $f$ of nodes perturbed, for $C = 1$, $a = 0.1$, Random Scale-Free network of size $N = 50$ (blue), 100 (green) and 200 (red) for $m = 1$ (a,c) and $m = 2$ (b,d), where the perturbed nodes are chosen in descending order of betweeness centrality. In the top row $a = 0.1$ and $a = 0.36$ for the bottom row.

**Perturbations onto a small phase-space volume in the basin of attraction of another co-existing attractor:**

In this perturbation scheme, initial states of the nodes in the network are localized on the phase space points of one attracting state, and fraction $f$ of nodes are perturbed onto a small sub-set of the basin volume of the other co-existing attractor. The influence of this type of large perturbation on nodes with the highest and lowest betweeness, closeness and degree in a RSF network are displayed in Fig. 5.12a-c for limit cycles and in Fig. 5.12d-f for chaotic attractors. The broad trends are similar for all three centrality measures, as we had observed in our earlier perturbation scheme.
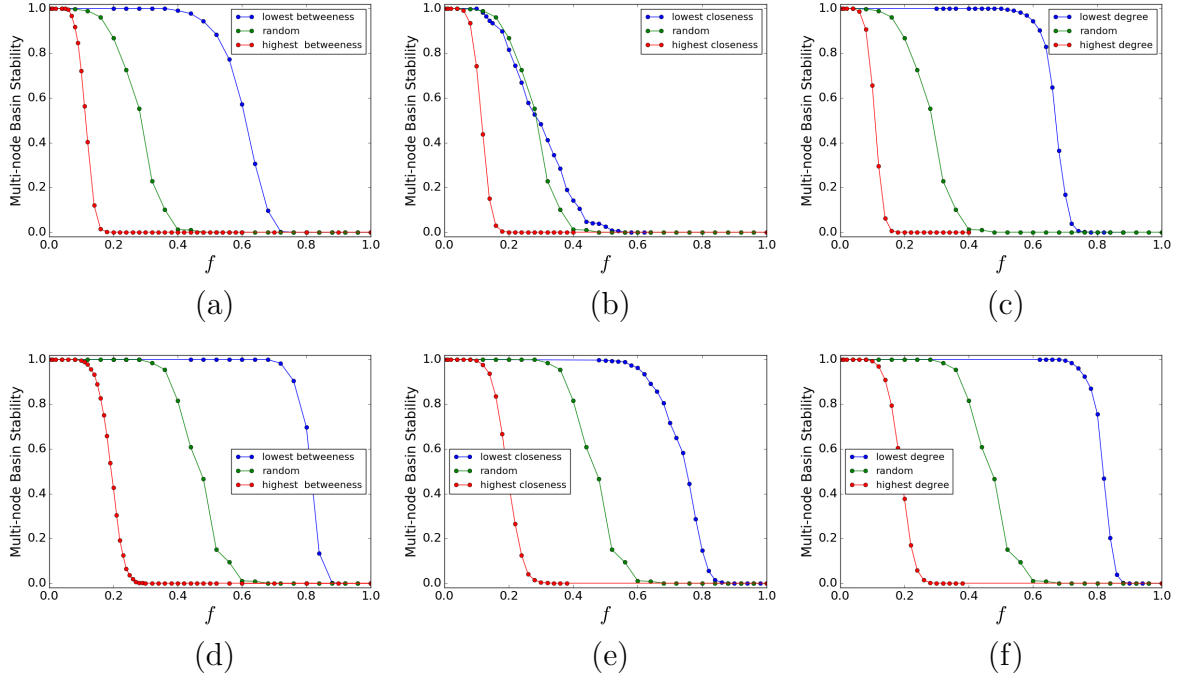
Figure 5.12: Dependence of the multi-node basin stability of Random Scale-Free networks of size $N = 100$, with $m = 2$ and $C = 1$, on the fraction of perturb nodes. For the top row $a = 0.1$ and for the bottom row $a = 0.36$. In the panels, three cases are shown. In the first case, the perturbed nodes are chosen at random (green curves). In the second case (red curves) the perturbed nodes are chosen in descending order of (a,d) betweeness centrality, (b,e) closeness centrality and (c,f) degree (i.e. the perturbed nodes are the ones with the highest $b$, $c$ or $k$ centrality measures). In the third case (blue curves) the perturbed nodes are chosen in ascending order of (a,d) betweeness centrality, (b,e) closeness centrality and (c,f) degree (i.e. the perturbed nodes are the ones with the lowest $b$, $c$ or $k$ centrality measures).

It is clearly evident from Figs. 5.12 that when nodes with the highest betweeness, closeness and degree centrality are perturbed, multi-node basin stability falls drastically. On the other hand, on perturbing the same number of nodes of low centrality results in the multi-node stability falling slowly. We again observe that for the case of co-existing limit cycles, when nodes of increasing closeness centrality, starting from nodes with lowest $c$, are perturbed (cf. Fig. 5.12b vis-a-vis 5.12a and Fig. 5.12c) the system loses stability at much lower $f$ than for the case where the perturbed have the lowest degree and betweeness centrality. This difference is also discernable for the case of co-existing chaotic attractors, but again not as pronounced as in the case of co-existing limit cycles. As before, we also show the basin stability of a network where the perturbed nodes are randomly chosen, corresponding to random attacks on a subset of nodes. Again clearly, a targeted attack on nodes with high centrality can destroy the collective dynamics much more efficiently

than random attacks. Further one notices that on increasing the fraction of perturbed nodes, where the nodes are chosen in ascending order of centrality, the robustness of the network of limit cycle oscillators is lost faster vis-a-vis networks of chaotic attractors.

Fig. 5.13 displays the dependence of the multi-node basin stability on the fraction of perturbed nodes $f$ in the RSF network with $m = 1$ and $m = 2$, for the case of networks of oscillators with co-existing limit cycles (a,b,c) and with co-existing chaotic attractors (d,e,f). As the fraction of perturbed nodes increases, the multi-node basin stability falls significantly for RSF networks with $m = 1$, while RSF networks with $m = 2$ remains robust up to a critical fraction $f_{crit}$ of perturbed nodes, with $f_{crit} \sim 0.05$ for limit cycle dynamics and $f_{crit} \sim 0.1$ for chaotic dynamics.
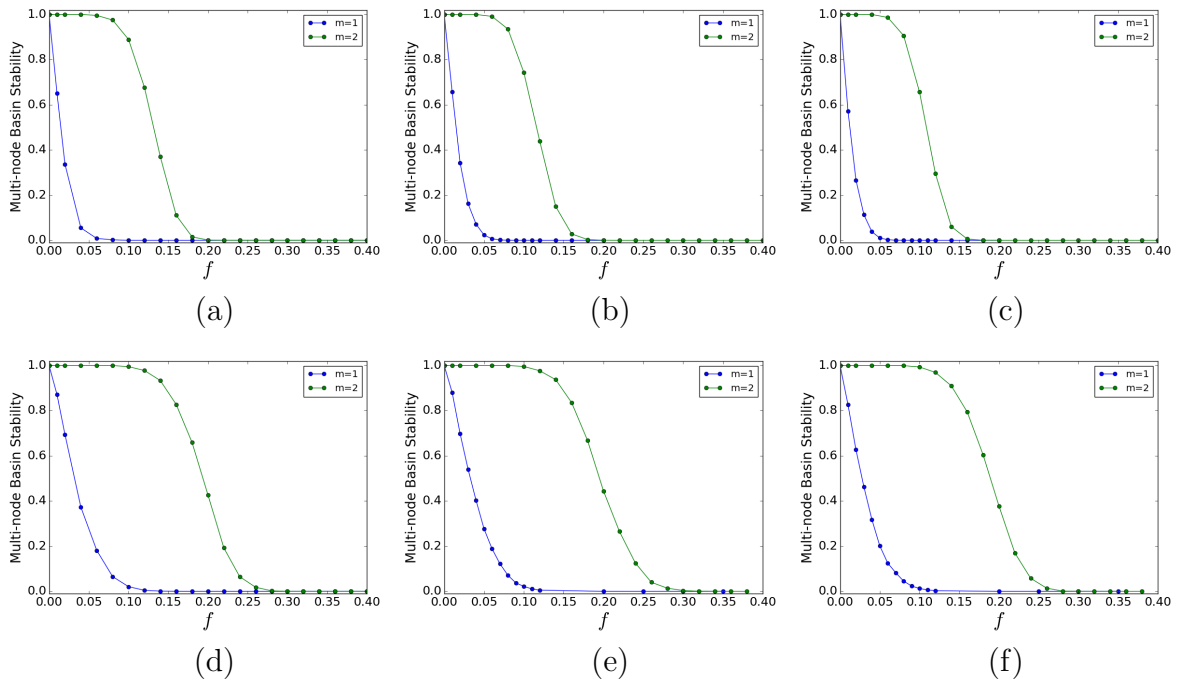


Figure 5.13: Multi-node basin stability vs fraction $f$ of nodes perturbed, for Random Scale-Free network of size $N = 100$, coupling strength $C = 1$, with $m = 1$ and $m = 2$, where the perturbed nodes are chosen in descending order of (a,d) betweeness centrality, (b,e) closeness centrality and (c,f) degree (i.e. the perturbed nodes are the ones with the highest $b$, $c$ or $k$ centrality measures). In the top row $a = 0.1$ and in the bottom row $a = 0.36$.

Lastly, we study the effect of system size on multi-node basin stability. Networks sizes ranging from 50 to 200 are studied, perturbing nodes in decreasing order of betweeness centrality. The results for networks of Duffing oscillators with co-existing limit cycles and co-existing chaotic attractors are displayed in Fig. 5.14a-b and Fig. 5.14c-d respectively.

We observe that a RSF network with $m = 1$ yields $f_{crit} \to 0$ (i.e. the smallest fraction of perturbed nodes destroy the collective state), while for the case of $m = 2$, for the limit cycle case, $f_{crit} \sim 0.06$ and $f_{crit} \sim 0.1$ for the chaotic case. So a RSF network with $m = 2$ is more robust to localized perturbations than a a RSF network with $m = 1$, as in the $m = 2$ case, even when nearly 10% of the nodes of the highest betweeness centrality are perturbed the entire network still manages to return to the original state.
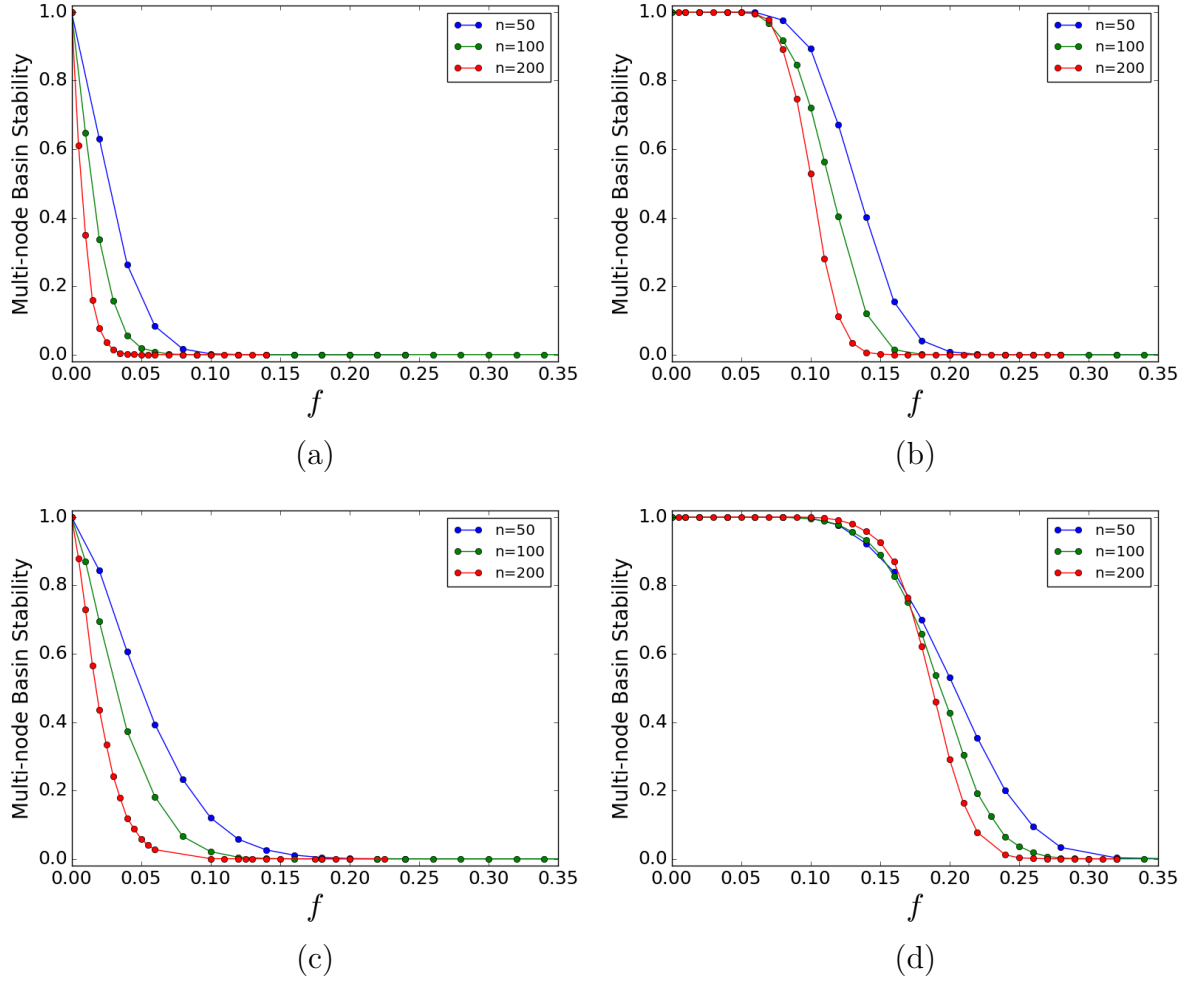


Figure 5.14: Multi-node basin Stability vs fraction $f$ of nodes perturbed, for $C = 1$, Random Scale-Free network of size $N = 50$ (blue), 100 (green) and 200 (red) for $m = 1$ (a,c) and $m = 2$ (b,d), where the perturbed nodes are chosen in descending order of betweeness centrality. In the top row $a = 0.1$ and $a = 0.36$ for the bottom row.

**Perturbations randomly chosen in a large phase-space volume:**

In this perturbation scheme, initial states of the nodes in the network are localized on one of the two co-exiting attractors, and then a fraction $f$ of nodes are given large

perturbations that take them to phase points randomly distributed in a large volume of phase space. This perturbation scheme is closer to the commonly used method of estimating basin stability. The influence of this type of large perturbation on nodes with the highest and lowest betweeness, closeness and degree in a RSF network are displayed in Fig. 5.15a-c for limit cycles and in Fig. 5.15d-f for chaotic attractors. The broad trends are similar for all three centrality measures, as we had observed in our earlier perturbation schemes. It is clearly evident from Figs. 5.15 that when nodes with the highest betweeness, closeness and degree centrality are perturbed, multi-node basin stability falls drastically. On the other hand, on perturbing the same number of nodes of low centrality results in the multi-node stability falling slowly. Further notice that the distinct trends for the case of perturbed nodes with increasing closeness centrality, though still discernable for the limit cycles, is much less pronounced than for the perturbation schemes above.
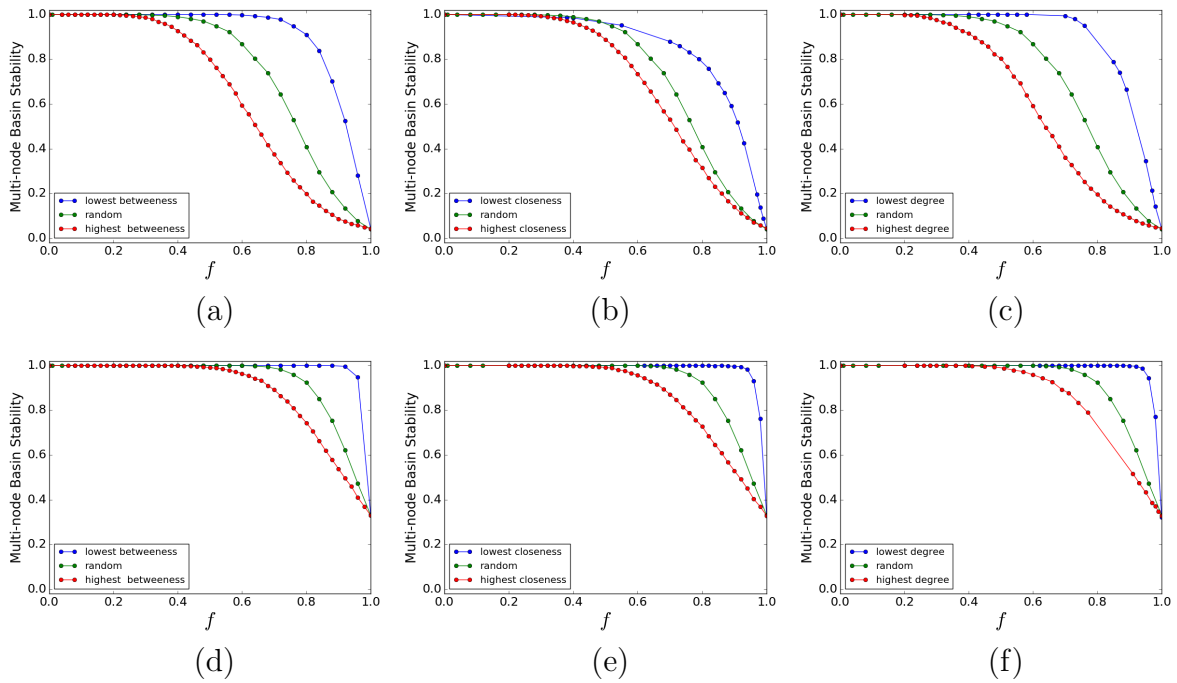


Figure 5.15: Dependence of the multi-node basin stability of Random Scale-Free networks of size $N = 100$, with $m = 2$ and $C = 1$, on the fraction of perturb nodes. For the top row $a = 0.1$ and for the bottom row $a = 0.36$. In the panels, three cases are shown. In the first case, the perturbed nodes are chosen at random (green curves). In the second case (red curves) the perturbed nodes are chosen in descending order of (a,d) betweeness centrality, (b,e) closeness centrality and (c,f) degree (i.e. the perturbed nodes are the ones with the highest $b$, $c$ or $k$ centrality measures). In the third case (blue curves) the perturbed nodes are chosen in ascending order of (a,d) betweeness centrality, (b,e) closeness centrality and (c,f) degree (i.e. the perturbed nodes are the ones with the lowest $b$, $c$ or $k$ centrality measures).

As before, we also show the basin stability of a network where the perturbed nodes are randomly chosen, corresponding to random attacks on a subset of nodes. Again clearly, a targetted attack on nodes with high centrality can destroy the collective dynamics much more efficiently than random attacks. Further one notices that on increasing the fraction of perturbed nodes, where the nodes are chosen in ascending order of centrality, the robustness of the network of limit cycle oscillators is lost faster vis-a-vis networks of chaotic attractors.



Figure 5.16: Multi-node basin Stability vs fraction $f$ of nodes perturbed, for Random Scale-Free network of size $N = 100$, coupling strength $C = 1$, with $m = 1$ and $m = 2$, where the perturbed nodes are chosen in descending order of (a,d) betweeness centrality, (b,e) closeness centrality and (c,f) degree (i.e. the perturbed nodes are the ones with the highest $b$, $c$ or $k$ centrality measures). $a = 0.1$ for the top row (a,b,c)and $a = 0.36$ for the bottom row (d,e,f).

Fig. 5.16 displays the dependence of the multi-node basin stability on the fraction of perturbed nodes $f$ in the RSF network with $m = 1$ and $m = 2$, for the case of networks of oscillators with co-existing limit cycles (top panels) and with co-existing chaotic attractors (bottom panels). As the fraction of perturbed nodes increases, the multi-node basin stability falls significantly for RSF networks with $m = 1$, while RSF networks with $m = 2$ remains robust up to a critical fraction $f_{crit}$ of perturbed nodes, with $f_{crit} \sim 0.28$ for limit cycle dynamics and $f_{crit} \sim 0.5$ for chaotic dynamics. Notice that the $f_{crit}$ here is larger than the $f_{crit}$ obtained in the earlier two perturbation schemes. The

reason for this is the following: in the two perturbation schemes above the perturbation considered pushed the node to the basin of attraction of the other co-existing attractor. However here the perturbation is as large in magnitude as in the earlier schemes, but it is not designed to push the perturbed node to the other basin. So now we have a lower probability of the perturbation taking the perturbed node to the basin of attraction of the other co-existing attractor. Hence the fraction of nodes needed to de-stabilize the collective dynamics here is larger on an average (i.e. $f_{crit}$ is larger).
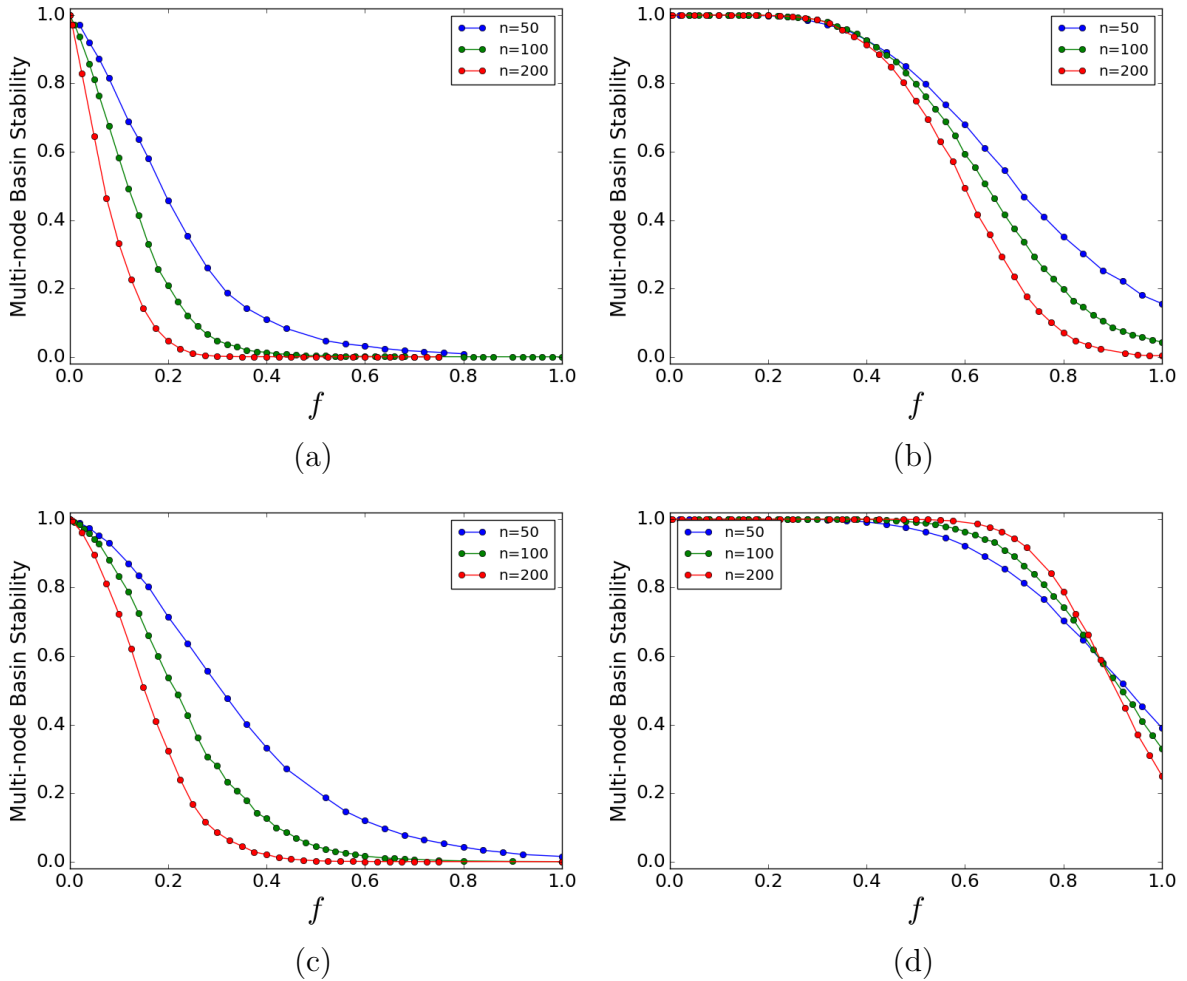


Figure 5.17: Multi-node basin stability vs fraction $f$ of perturbed nodes, for $C = 1$, RSF network of size $N = 50$ (blue), 100 (green) and 200 (red) for $m = 1$ (a,c) and $m = 2$ (b,d), where the perturbed nodes are chosen in descending order of betweeness centrality. In the top row (a,b) $a = 0.1$ and $a = 0.36$ for the bottom row (c,d).

Lastly, we study the effect of system size on multi-node basin stability. Networks sizes ranging from 50 to 200 are studied, perturbing nodes in decreasing order of betweeness centrality. The results for networks of Duffing oscillators with co-existing limit cycles and

co-existing chaotic attractors are displayed in Fig. 5.17a-b and Fig. 5.17c-d respectively. We observe that a RSF network with $m = 1$ yields $f_{crit} \to 0$ (i.e. the smallest fraction of perturbed nodes destroy the collective state), while for the case of $m = 2$, for the limit cycle case, $f_{crit} \sim 0.28$ and $f_{crit} \sim 0.5$ for the chaotic case. So a RSF network with $m = 2$ is more robust to localized perturbations than a a RSF network with $m = 1$.

In conclusion, the following broad trends hold for all three schemes of perturbations:

(i) Firstly, we find that when nodes with the highest betweeness, closeness and degree centrality are perturbed, the multi-node basin stability falls drastically. On the other hand, on perturbing the same number of nodes of low centrality results in the multi-node stability falling slowly.

(ii) Secondly, the network is less vulnerable to perturbations on randomly chosen nodes, corresponding to random attacks on a subset of nodes. This implies that a targetted attack on nodes with high centrality can destroy the collective dynamics much more efficiently than random attacks.

(iii) Lastly, we showed that under increasing fraction of perturbed nodes with high betweeness centrality, the multi-node basin stability falls rapidly for RSF networks with $m = 1$, while RSF networks with $m = 2$ remain robust up to a critical fraction $f_{crit}$ of perturbed nodes. This can be rationalized by the difference in the probability distributions of the centrality measures in $m = 1$ and $m = 2$ networks, with nodes in a $m = 1$ network having a significantly greater probability of having high betweeness values.


## 5.3.2  Dynamics of a Ring of multi-stable Duffing oscillators

Now we study a ring of oscillators, that is, a one-dimensional lattice with periodic boundary conditions. We consider each node to be connected to two nearest neighbours. In a ring network all nodes have the same degree, closeness and betweeness centrality. Therefore, now our focus is on the effect of the fraction of perturbed nodes and the distribution of the perturbed nodes on multi-node basin stability.

So we consider a ring where initially the states of all the nodes are distributed over phase points of one of the attractors. Then we perturb a fraction $f$ of nodes by a large perturbation to the phase space points of the other coexisting attractor (i.e. perturbation scheme P1). We perturb the nodes in clusters, where the perturbed nodes are contiguous to each other. We also examine the case where the perturbed nodes are randomly

distributed over the ring.
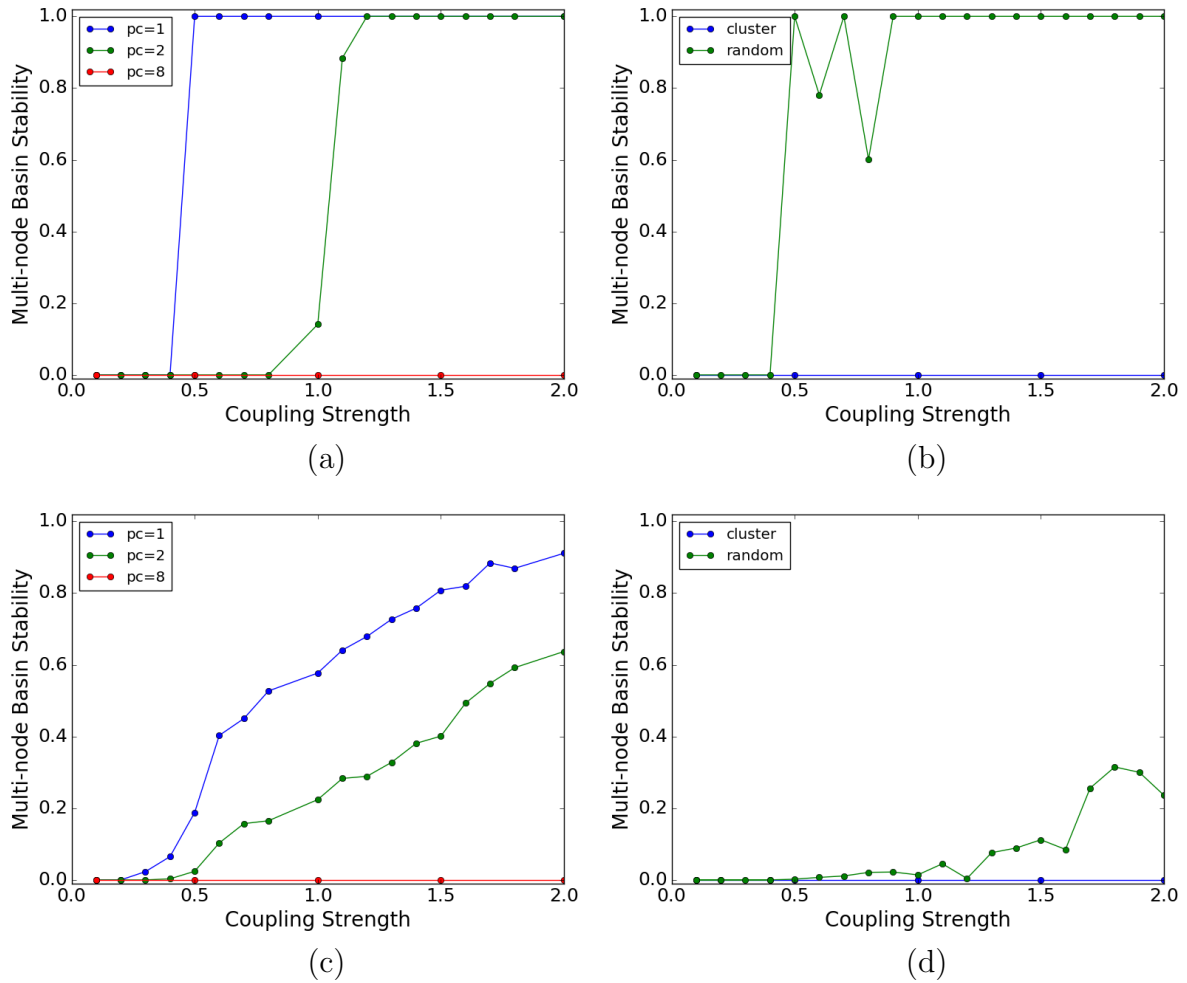


Figure 5.18: Dependence of multi-node basin stability on coupling strength, for a ring of Duffing oscillators given by Eqn. 5.2, with the fraction of perturbed nodes $f$ equal to 0.01 (blue), 0.02 (green) and 0.08 (red). Here the size of the ring is $N = 100$, and size of the coupling neighbourhood is $k = 2$, namely each site couples to its two nearest neighbours. Left panel shows the case where the perturbed nodes occur in clusters for (a) $a = 0.1$ and (c) $a = 0.36$. Right panel shows the multi-node basin stability for the case of perturbations at randomly located nodes, for $f = 0.08$ for (b) $a = 0.1$ and (d) $a = 0.36$. The case of perturbation in clusters (blue) is also shown for reference, for the same fraction of perturbed nodes in panels (b) and (d).

First we investigate the effect of coupling on the robustness of the dynamics. Fig. 5.18(a,c) shows the multi-node basin stability for this system, as the coupling strength is increased in the range 0 to 2, for clusters of perturbed nodes, with $f$ ranging from 0.01 to 0.08. It is evident from the basin stability of the system, that there is a *sharp transition* for the limit cycle case (cf. Fig. 5.18a) from zero basin stability, namely the situation where *no*

perturbed state returns to the original state, to basin stability close to one, namely where *all* sampled perturbed states return to the original state. Unlike limit cycles, for the case of co-existing chaotic attractors (cf. Fig. 5.18a) the transition is less sharp and the transition to complete recovery on increasing coupling strength is more gradual (cf. Fig. 5.18c). Further, the figure also demonstrates the extreme sensitivity of basin stability to the number of nodes being perturbed. We find that the system fails to return to the original state, even at very high coupling strengths, even when only few nodes experience perturbations. For instance, for $f = 0.08$, where a cluster of 8 nodes are perturbed in the ring of 100 elements, there is zero basin stability in the entire coupling range. In contrast, Fig. 5.18(a) shows the case of a single perturbed node (i.e. $f = 0.01$), where the entire network recovers for coupling strengths stronger than approximately 0.4. So a ring loses its ability to return to the original state rapidly with increasing number of perturbed nodes.

So clearly, the stability of the ring with respect to localized perturbations depends on whether the perturbed nodes are in a cluster (cf. the case in Fig. 5.18(a,c)) or randomly spread over the ring, with the locations of the perturbed nodes being uncorrelated. Fig 5.18(b,d) shows the multi-node basin stability when nodes perturbed are chosen randomly for different values of coupling. We observe that the system is more stable here, as compared to the case when nodes are perturbed in clusters, namely *perturbations at random locations in a ring allows the system to recover its original dynamical more readily than perturbations on a cluster of contiguous nodes.* Also, it is clearly evident that a network of Duffing oscillators with co-existing limit cycles is more robust compared with a network where the oscillators have co-existing chaotic attractors.

### 5.3.3  Dynamics of Star Network of Multi-stable Duffing oscillators

Lastly, we study a star network of multi-stable Duffing oscillators. In this network there exists a very large difference between the degree, closeness and betweeness centrality of the central hub node and that of the peripheral (edge) nodes. So this network provides a good framework to investigate the correlation between specific properties of a node and the resilience of the network to large localized perturbations at such nodes. In this study we consider a star network where the initial states of all the nodes are distributed over phase points of one of the attractors. Then we perturb a fraction $f$ of nodes by a large perturbation to the phase space points of the other coexisting attractor (i.e. perturbation

scheme P1), and estimate the multi-node basin stability of the network.
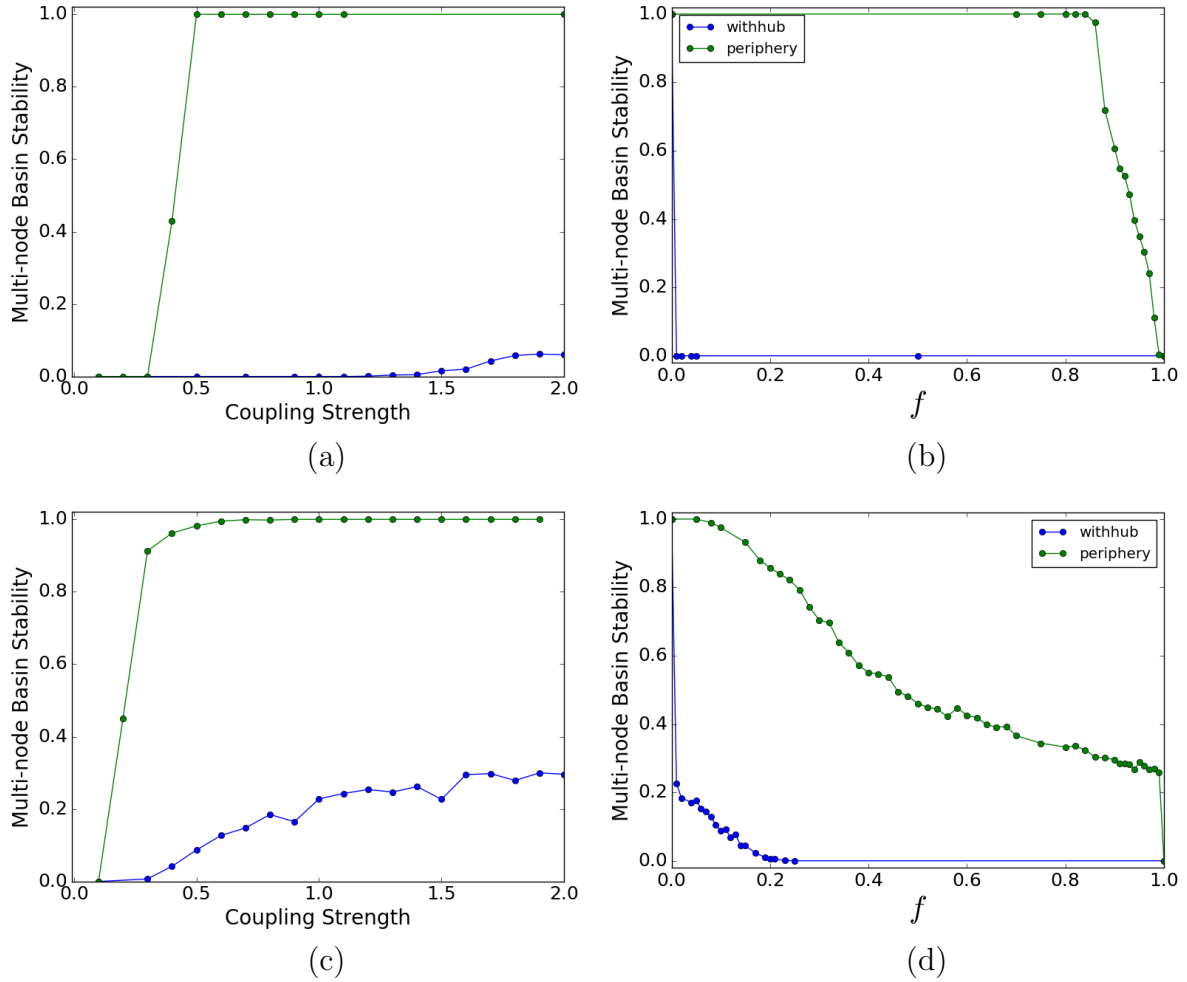


Figure 5.19: In the left panel (a,c) multi-node basin stability vs coupling strength for a star network of size $N = 100$: the hub node is perturbed (blue) and a single peripheral node is perturbed (green). In the right panel (b,d) multi-node basin stability vs number of nodes perturbed in the star network of Duffing oscillators. Here the size of the network $N = 100$ and coupling strength $C = 1$. The green curve represents the case where only peripheral nodes are perturbed, while blue represents the case where the hub is perturbed along with peripheral nodes. In the top row $a = 0.1$ and in the bottom row $a = 0.36$.

We consider fraction $f$ of perturbed nodes ranging from single node in Fig. 5.19(a) to the case where nearly all nodes in the system are perturbed $f \sim 1$. It is evident from the single node basin stability of a network of Duffing oscillators with co-existing limit cycles, where the single perturbed node is the hub (cf. Fig. 5.19a), that the basin stability is almost zero even for high coupling strength. Similarly, the single node basin stability of a network of Duffing oscillators with co-existing chaotic attractors, where the single perturbed node is the hub (cf. Fig. 5.19c), shows that the basin stability is very low even

for high coupling strengths. So it is clear that *just a single node is enough to destroy the stability of the network, if that node has very high degree, closeness and betweeness centrality, such as the hub node, irrespective of the nature of the nodal dynamics.*

Next we study the multi-node basin stability for the case where some fraction of the low centrality peripheral nodes are perturbed. It is evident from Fig. 5.19b, for networks of Duffing oscillators with co-existing limit cycles, that even when $f$ is as high as 0.8 (i.e. where 80% of the peripheral nodes are strongly perturbed), there is no discernable difference in the basin stability, which remains close to 1. This implies that even when more than half the nodes in the network are perturbed, the entire system almost always recovers to the original state. However, for the case of networks of Duffing oscillators with co-existing chaotic attractors, even when very few peripheral nodes are perturbed (e.g. $f = 0.08$) the network loses its stability (cf. Fig. 5.19d). In the conclusion we can say that the resilience of a star network on localized perturbations on low centrality peripheral nodes depends on the type of nodal dynamics, with chaotic attractors being more vulnerable to destabilization.

## 5.4    Conclusions

We have explored the collective dynamics of multi-stable Duffing oscillators connected in different network topologies, ranging from Rings to Random Scale-Free networks and Stars, under mean-field diffusive coupling. We estimated the dynamical resilience of such networks by introducing a variant of the concept of multi-node basin stability, using three types of perturbation schemes. This measure allowed us to gauge the global stability of the dynamical network in response to perturbations affecting the nodes of the system.

First we have explored Random Scale-Free Networks with $m = 1$ and $m = 2$, under the three perturbation schemes. We showed that for all types of perturbations, the perturbed nodes with high centrality significantly reduce the capacity of the system to return to the desired attractor. We also showed that RSF networks with $m = 2$ are more robust than RSF networks with $m = 1$ under targetted attckes on highest betweeness centrality nodes. Further, we observed that the robustness of the network of multi-stable systems depends on the nature of the dynamical attractors, as well as the perturbation schemes. For instance, when nodes are perturbed onto another coexisting attractor, then networks of limit cycles oscillators are more robust than networks of chaotic attractors. However, interestingly, when nodes are perturbed onto a small phase space volume of another attractor, or they are perturbed to randomly chosen points in a large volume

of phase-space, then the network of chaotic attractors is more robust than network of limit cycles. The underlying reason for this could be the interplay of two competing factors. The first is the distance in phase-space between the co-existing attractors (this is more for co-existing limit cycles compraed to co-existing chaotic attractors). The second contributing factor is the typical amplitude of the perturbations in each scheme, and probability of the perturbation taking the node to the basin of attraction of some other attractor.

Lastly, we explored the robustness of rings and star networks of multi-stable Duffing oscillators to large localized perturbations. Here we consider all nodes of the initial system to be on one of the attractors. Then a fraction of nodes are perturbed onto the other attractor. We observed the following: a ring network is more robust to random attacks compared to attacks on a cluster of nodes. Further, the network with co-existing limit cycles is more stable than co-existing chaotic attractors. In the star network, when the central hub node was perturbed, the stability of the network was lost very quickly. This de-stabilization occured even for a very small fraction of perturbed nodes, as well as for low coupling strengths, if the perturbed nodes include the hub.

In summary, *targetted attack on nodes with high centrality in a scale-free networks, and targetted attacks on clusters of nodes in a ring network, can destroy the collective dynamics much more efficiently than random attacks.* This feature appears to be general and holds for networks of coupled limit cycles, as well as coupled chaotic attractors.

# Chapter 6

# Conclusions and future directions

Broadly speaking, in this thesis we have explored the effect of the interplay of dynamical complexity and structural complexity on emergent collective dynamical behaviour in complex systems. Development of a general theory or the establishment of a mathematical framework to understand emergent phenomena in complex systems is a fundamental challenge in this interdisciplinary field of science. This thesis addresses some of these important aspects of complex systems.

For instance, in the first problem, we have studied El Niño phenomenon which globally affects the climate and economic conditions. To understand this phenomenon, we have considered a system of two coupled delayed action oscillators to model ENSO phenomenon in two sub-regions and studied the dynamics of the sea surface temperature (SST) anomalies. We have explored the dynamics of ENSO phenomenon in the space of three parameters: self-delay, delay, and inter-region coupling strengths. The emergence or suppression of oscillations in our models is a dynamical feature of utmost relevance, as it signals the presence or absence of ENSO-like oscillations. Different parameters yield a rich variety of dynamical patterns in our model, ranging from steady states and homogeneous oscillations to irregular oscillations. We have also displayed how non-uniformity in delays, and the difference in the strengths of the self-delay coupling of the sub-regions, affect the rise of oscillations. We have also explored the robustness of the different dynamical states under noisy evolution, in order to gauge which set of attractors are typically expected to arise when the system evolves under the influence of external perturbations. We then investigated the basins of attraction of the different dynamical attractors arising in our model. Typically, the number of distinct attractors and their basins of attraction depend upon the values of parameters. Mapping of the basins of attractions from our

numerical results suggests that instead of the single value criterion (as 0.5°C which is given by NOAA agencies), an interval should be used as criterion to estimate the El Niño or La Nina progress, based on the combinations of SST anomalies that lie in the relevant basin of attraction. Thus our dynamical model may help in providing a potential framework to understand patterns in the SST anomalies in different coupled sub-regions. In the future, we can extend our work to develop mathematical models which have a rich variety of phase space structures and include all possible terms that are responsible for realistic ENSO phenomenon. We would like to analyze real data of the sea surface temperature anomalies of various equatorial regions to understand the El Niño effect. From the observation of the trends in temperature anomalies over the past years we can develop ideas that could help in the very important problem of forecasting El Niño/La Niña years.

In the second problem we have studied star networks of diffusively, conjugately and mean-field coupled Rössler and Lorenz systems. Now in the star network, all end-nodes are identical in terms of the coupling environment and dynamical equations, because they are all connected only to the central hub node. Remarkably we observe, we observe that the symmetry of the end-nodes is broken and coexisting groups with different synchronization features and attractor geometries emerge. We find that as coupling strength increases, the end-nodes go from a de-synchronized state to a completely synchronized state, via a large coupling parameter regime yielding chimera states. Further, based on our simulations, the robustness of these chimera states in analog circuit experiments under diffusive coupling and mean-field coupling was also demonstrated. Therefore, our numerical and experimental investigations indicate that chimera states in star network of Rössler and Lorenz systems is very prevalent. In the future, one can explore similar star networks of chaotic oscillators under nonlinear coupling, as well as threshold-activated coupling. Such a study would enable us to assess the prevalence of chimera states in star networks of chaotic systems, under different types of coupling functions. The general motivation here would be to find the coupling functions that allow the star network to show chimera states over the largest parameter ranges. Further, we would like to simulate network systems that can be verified readily in electronic analog circuit experiments or other laboratory set-ups.

Many natural phenomena as well as human-engineered devices, modelled by nonlinear systems can give rise to a rich gamut of patterns ranging from fixed point to cycle and chaos. These days the search for mechanisms that enable a chaotic complex system to maintain a fixed desired activity has witnessed broad research attention. The third research problem presented in this thesis is motivated in this direction. Here we

established a mechanism to control intrinsically chaotic meta-population to the steady states and periodic behaviour. For that we have explored Random Scale-Free networks of populations, modelled by chaotic Ricker maps, connected by transport that is triggered when population density in a patch is more than a critical threshold level. Our central result was that threshold-activated dispersal leads to stable fixed populations, for a wide range of threshold levels. Further, suppression of chaos is facilitated when the threshold-activated migration is more rapid than the intrinsic population dynamics of a patch. Additionally, networks with a large number of nodes open to the environment, readily yield stable steady states. Lastly, we demonstrated that in networks with very few open nodes, the degree and betweeness centrality of the node open to the environment has a pronounced influence on control. All qualitative trends were corroborated by quantitative measures, reflecting the efficiency of control, and the width of the steady state window. In the future, one can implement this control strategy on a variety of complex networks, in order to verify the generality of this control idea. Further we would like to find other methods to control emergent dynamical behaviour, hence contributing towards the understanding of control of complex systems to target states.

As we know that emergent collective spatiotemporal patterns in dynamical networks are determined by the interplay of the dynamics of the nodes and nature of the interactions (modelled by network topologies and coupling forms). Intuitively, if we consider a heterogeneous network of identical dynamics under a specific coupling scheme then the collective spatiotemporal patterns will depend only on the nodal properties. Now the important question here is the following: which nodal property plays the most significant role in determining the robustness of the synchronized state of the network in response to large perturbations targetted on the node. In order to investigate this problem we have explored the response of Random Scale-Free Networks of multi-stable Duffing oscillators to large localized perturbations. Specifically, we investigated the basin-stability of the state where all systems at the nodes were in the same basin of attraction, for the case of co-existing limit cycles as well as co-existing chaotic attractors. To gauge the global stability of the synchronized state we introduced a variant of the concept of multi-node basin stability. Our study involved perturbations on the nodes under three different schemes: (i) perturbations on to phase-space points of another co-existing attractor, (ii) perturbations on to a small phase-space volume in the basin of attraction of another co-existing attractor, and (iii) perturbations on to randomly chosen phase-space points in a large phase-space volume. We observed the following well-defined common trends for all three perturbation schemes:
(i) Perturbed nodes with highest betweeness centrality, closeness centrality and degree

significantly reduces the capacity of scale free networks to return to the original synchronized state.

(ii) Random Scale-Free networks with $m = 2$ is more robust than Random Scale-Free networks with $m = 1$ under targetted attacks on highest betweeness centrality nodes. This implies that RSF networks with higher connectedness are more robust than those with lower connectedness.

(iii) Targetted attacks on clusters of nodes in ring network can destroy the collective dynamics much more efficiently than random attacks.

In the future, one can study a wide range of dynamical systems with co-existing attractors of varying geometries, in order to make a more general statement on the robustness of scale-free networks of multi-stable systems in the presence of large localized perturbations.

In summary, in this thesis we have explored the emergent spatiotemporal patterns in a broad range of complex systems modelling nonlinear phenomena ranging from climate to population dynamics, as well as engineered dynamical systems. We have considered network topologies ranging from ring and star networks to random scale-free networks, and we have investigated diffusive, conjugate, mean-field and threshold-activated coupling forms. Our salient results are the following:

(i) Mapping of the basins of attraction in coupled delayed action oscillator models modelling the El Niño phenomena. This might be of potential use in the forecasting of the El Niño and La Nina years.

(ii) Demonstrated the prevalence of chimera states in Star networks of chaotic oscillators. These results show that Star networks provide a promising class of coupled systems, in natural or human-engineered contexts, where chimeras are prevalent.

(iii) Proposed mechanisms for controlling networks of intrinsically chaotic meta-populations, to steady states and periodic behaviour. These ideas (or extensions there of) may be useful in controlling other complex dynamical networks, for instance neuronal networks.

(iv) Investigated the influence of the properties of perturbed nodes on the global stability of networks of multi-stable chaotic atttractors. These results can help assess the robustness and resilience of complex networks to targetted localized attacks.

So in conclusion, the work in this thesis can potentially contribute to the understanding of complex systems in general, as well as help us gain insights on pattern formation in specific systems ranging from model ecological and climate networks to engineered electronic circuits.

# Bibliography

[1] Steven H Strogatz. Exploring complex networks. *nature*, 410(6825):268, 2001.

[2] JA Scott Kelso. *Dynamic patterns: The self-organization of brain and behavior*. MIT press, 1997.

[3] Stuart A Kauffman. The origins of order: Self-organization and selection in evolution. In *Spin glasses and biology*, pages 61–100. World Scientific, 1992.

[4] Réka Albert and Albert-László Barabási. Statistical mechanics of complex networks. *Reviews of modern physics*, 74(1):47, 2002.

[5] Nicholas F Britton. *Essential mathematical biology*. Springer Science & Business Media, 2012.

[6] AH Nayfeh and DT Mook. Nonlinear oscillations, wiley, new york, 1979. *MATH Google Scholar*.

[7] Otto E Rössler. An equation for continuous chaos. *Physics Letters A*, 57(5):397–398, 1976.

[8] Otto E Rössler. Chaotic behavior in simple reaction systems. *Zeitschrift für Naturforschung A*, 31(3-4):259–264, 1976.

[9] Edward N Lorenz. Deterministic nonperiodic flow. *Journal of the atmospheric sciences*, 20(2):130–141, 1963.

[10] Albert-László Barabási and Réka Albert. Emergence of scaling in random networks. *science*, 286(5439):509–512, 1999.

[11] David G Andrews. *An introduction to atmospheric physics*. Cambridge University Press, 2010.

[12] GR North, J Pyle, and F Zhang. Encyclopedia of atmospheric sciences, 2003.

[13] James R Holton and Gregory J Hakim. *An introduction to dynamic meteorology*, volume 88. Academic press, 2012.

[14] Chunzai Wang, Clara Deser, Jin-Yi Yu, Pedro DiNezio, and Amy Clement. El-niño and southern oscillation (enso): a review. *Coral reefs of the Eastern Pacific*, 8:3–19, 2012.

[15] Jakob Bjerknes. Atmospheric teleconnections from the equatorial pacific. *Monthly Weather Review*, 97(3):163–172, 1969.

[16] Stephen E Zebiak and Mark A Cane. A model el niñ–southern oscillation. *Monthly Weather Review*, 115(10):2262–2278, 1987.

[17] Fei-Fei Jin. An equatorial ocean recharge paradigm for enso. part i: Conceptual model. *Journal of the Atmospheric Sciences*, 54(7):811–829, 1997.

[18] Fei-Fei Jin. An equatorial ocean recharge paradigm for enso. part ii: A stripped-down coupled model. *Journal of the Atmospheric Sciences*, 54(7):830–847, 1997.

[19] Robert H Weisberg and Chunzai Wang. A western pacific oscillator paradigm for the el niño-southern oscillation. *Geophysical research letters*, 24(7):779–782, 1997.

[20] Chunzai Wang, Robert H Weisberg, and Jyotika I Virmani. Western pacific interannual variability associated with the el niño-southern oscillation. *Journal of Geophysical Research: Oceans*, 104(C3):5131–5149, 1999.

[21] Joël Picaut, François Masia, and Y Du Penhoat. An advective-reflective conceptual model for the oscillatory nature of the enso. *Science*, 277(5326):663–666, 1997.

[22] Ben P Kirtman and Paul S Schopf. Decadal variability in enso predictability and prediction. *Journal of Climate*, 11(11):2804–2822, 1998.

[23] Michael Ghil, Ilya Zaliapin, and Sylvester Thompson. A delay differential model of enso variability: parametric instability and the distribution of extremes. *Nonlin. Processes Geophysics*, 15(3):417–433, 2008.

[24] Eli Tziperman, Lewi Stone, Mark A Cane, Hans Jarosh, et al. El nino chaos: Overlapping of resonances between the seasonal cycle and the pacific ocean-atmosphere oscillator. *Science-AAAS-Weekly Paper Edition-including Guide to Scientific Information*, 264(5155):72–73, 1994.

[25] Max J Suarez and Paul S Schopf. A delayed action oscillator for enso. *Journal of the atmospheric Sciences*, 45(21):3283–3287, 1988.

[26] David S Battisti and Anthony C Hirst. Interannual variability in a tropical atmosphere–ocean model: Influence of the basic state, ocean geometry and non-linearity. *Journal of the Atmospheric Sciences*, 46(12):1687–1712, 1989.

[27] Ian Boutle, Richard HS Taylor, and Rudolf A Römer. El niño and the delayed action oscillator. *American Journal of Physics*, 75(1):15–24, 2007.

[28] Soon-Il An. A review of interdecadal changes in the nonlinearity of the el nino-southern oscillation. *Theoretical and applied climatology*, 97(1-2):29–40, 2009.

[29] Chunzai Wang. A unified oscillator model for the el niño–southern oscillation. *Journal of Climate*, 14(1):98–115, 2001.

[30] Fei-Fei Jin, L Lin, A Timmermann, and J Zhao. Ensemble-mean dynamics of the enso recharge oscillator under state-dependent stochastic forcing. *Geophysical research letters*, 34(3), 2007.

[31] M Bianucci. Analytical probability density function for the statistics of the enso phenomenon: Asymmetry and power law tail. *Geophysical Research Letters*, 43(1):386–394, 2016.

[32] `https://www.esrl.noaa.gov/psd/gcos_wgsp/Timeseries/Nino3/`.

[33] `https://www.esrl.noaa.gov/psd/gcos_wgsp/Timeseries/Nino4/`.

[34] Yoshiki Kuramoto and Dorjsuren Battogtokh. Coexistence of coherence and incoherence in nonlocally coupled phase oscillators. *arXiv preprint cond-mat/0210694*, 2002.

[35] Shin-ichiro Shima and Yoshiki Kuramoto. Rotating spiral waves with phase-randomized core in nonlocally coupled oscillators. *Physical Review E*, 69(3):036213, 2004.

[36] Daniel M Abrams and Steven H Strogatz. Chimera states for coupled oscillators. *Physical review letters*, 93(17):174102, 2004.

[37] Aaron M Hagerstrom, Thomas E Murphy, Rajarshi Roy, Philipp Hövel, Iryna Omelchenko, and Eckehard Schöll. Experimental observation of chimeras in coupled-map lattices. *Nature Physics*, 8(9):658–661, 2012.

[38] Mark R Tinsley, Simbarashe Nkomo, and Kenneth Showalter. Chimera and phase-cluster states in populations of coupled chemical oscillators. *Nature Physics*, 8(9):662–665, 2012.

[39] Erik Andreas Martens, Shashi Thutupalli, Antoine Fourrière, and Oskar Hallatschek. Chimera states in mechanical oscillator networks. *Proceedings of the National Academy of Sciences*, 110(26):10563–10567, 2013.

[40] Laurent Larger, Bogdan Penkovsky, and Yuri Maistrenko. Virtual chimera states for delayed-feedback systems. *Physical review letters*, 111(5):054103, 2013.

[41] Amit Sharma, Manish Dev Shrimali, Awadhesh Prasad, Ram Ramaswamy, and Ulrike Feudel. Phase-flip transition in relay-coupled nonlinear oscillators. *Physical Review E*, 84(1):016226, 2011.

[42] Rajat Karnatak, Ram Ramaswamy, and Ulrike Feudel. Conjugate coupling in ecosystems: Cross-predation stabilizes food webs. *Chaos, Solitons & Fractals*, 68:48–57, 2014.

[43] Arturo Buscarino, Mattia Frasca, Lucia Valentina Gambuzza, and Philipp Hövel. Chimera states in time-varying complex networks. *Physical Review E*, 91(2):022817, 2015.

[44] R Gopal, VK Chandrasekar, A Venkatesan, and M Lakshmanan. Observation and characterization of chimera states in coupled dynamical systems with nonlocal coupling. *Physical Review E*, 89(5):052914, 2014.

[45] Alan Garfinkel, Mark L Spano, William L Ditto, and James N Weiss. Controlling cardiac chaos. *Science*, 257(5074):1230–1235, 1992.

[46] Kevin Hall, David J Christini, Maurice Tremblay, James J Collins, Leon Glass, and Jacques Billette. Dynamic control of cardiac alternans. *Physical Review Letters*, 78(23):4518, 1997.

[47] BA Huberman and E Lumer. Dynamics of adaptive systems. *IEEE Transactions on Circuits and Systems*, 37(4):547–550, 1990.

[48] Sudeshna Sinha, Ramakrishna Ramaswamy, and J Subba Rao. Adaptive control in nonlinear dynamics. *Physica D: Nonlinear Phenomena*, 43(1):118–128, 1990.

[49] Edward Ott, Celso Grebogi, and James A Yorke. Controlling chaos. *Physical review letters*, 64(11):1196, 1990.

[50] Leon Glass and Wanzhen Zeng. Bifurcations in flat-topped maps and the control of cardiac chaos. *International Journal of Bifurcation and Chaos*, 4(04):1061–1067, 1994.

[51] Sudeshna Sinha and Neelima Gupte. Adaptive control of spatially extended systems: targeting spatiotemporal patterns and chaos. *Physical Review E*, 58(5):R5221, 1998.

[52] Sean P Cornelius, William L Kath, and Adilson E Motter. Realistic control of network dynamics. *Nature communications*, 4:1942, 2013.

[53] Ilkka Hanski. Metapopulation dynamics. *Nature*, 396(6706):41–49, 1998.

[54] Caz M Taylor and Richard J Hall. Metapopulation models for seasonally migratory animals. *Biology letters*, page rsbl20110916, 2011.

[55] Richard Levins. Some demographic and genetic consequences of environmental heterogeneity for biological control. *American Entomologist*, 15(3):237–240, 1969.

[56] Vittoria Colizza, Romualdo Pastor-Satorras, and Alessandro Vespignani. Reaction–diffusion processes and metapopulation models in heterogeneous networks. *Nature Physics*, 3(4):276–282, 2007.

[57] Benjamin Kerr, Claudia Neuhauser, Brendan JM Bohannan, and Antony M Dean. Local migration promotes competitive restraint in a host–pathogen'tragedy of the commons'. *Nature*, 442(7098):75–78, 2006.

[58] James H Brown and Astrid Kodric-Brown. Turnover rates in insular biogeography: effect of immigration on extinction. *Ecology*, 58(2):445–449, 1977.

[59] Tobias Reichenbach, Mauro Mobilia, and Erwin Frey. Mobility promotes and jeopardizes biodiversity in rock–paper–scissors games. *Nature*, 448(7157):1046–1049, 2007.

[60] Bernard Cazelles, Samuele Bottani, and Lewi Stone. Unexpected coherence and conservation. *Proceedings of the Royal Society of London B: Biological Sciences*, 268(1485):2595–2602, 2001.

[61] Sudeshna Sinha and Debabrata Biswas. Adaptive dynamics on a chaotic lattice. *Physical review letters*, 71(13):2010, 1993.

[62] Sudeshna Sinha. Unidirectional adaptive dynamics. *Physical Review E*, 49(6):4832, 1994.

[63] Sudeshna Sinha. Adaptive dynamics on circle maps. *Physics Letters A*, 199(5-6):365–374, 1995.

[64] Sudeshna Sinha. Chaos and regularity in adaptive lattice dynamics. *International Journal of Modern Physics B*, 9(08):875–931, 1995.

[65] Per Bak, Chao Tang, and Kurt Wiesenfeld. Self-organized criticality: An explanation of the 1/f noise. *Physical review letters*, 59(4):381, 1987.

[66] Xiao Fan Wang and Jian Xu. Cascading failures in coupled map lattices. *Physical Review E*, 70(5):056113, 2004.

[67] Arghya Mondal and Sudeshna Sinha. Spatiotemporal consequences of relaxation time scales in threshold-coupled systems. *Physical Review E*, 73(2):026215, 2006.

[68] Sudeshna Sinha. Using thresholding at varying intervals to obtain different temporal patterns. *Physical Review E*, 63(3):036212, 2001.

[69] Sudeshna Sinha. Consequences of nonlocal connections in networks of chaotic maps under threshold activated coupling. *Physical Review E*, 69(6):066209, 2004.

[70] K Murali and Sudeshna Sinha. Experimental realization of chaos control by thresholding. *Physical Review E*, 68(1):016210, 2003.

[71] Marten Scheffer, Sergio Rinaldi, Alessandra Gragnani, Luuc R Mur, and Egbert H van Nes. On the dominance of filamentous cyanobacteria in shallow, turbid lakes. *Ecology*, 78(1):272–282, 1997.

[72] Gouhei Tanaka, Kai Morino, and Kazuyuki Aihara. Dynamical robustness in complex networks: the crucial role of low-degree nodes. *Scientific reports*, 2:232, 2012.

[73] Hiroaki Daido and Kenji Nakanishi. Aging transition and universal scaling in oscillator networks. *Physical review letters*, 93(10):104101, 2004.

[74] Takashi Morie, Daisuke Atuti, Kazuki Ifuku, Yoshihiko Horio, and Kazuyuki Aihara. A cmos nonlinear-map circuit array for threshold-coupled chaotic maps using pulse-modulation approach. In *Circuit Theory and Design (ECCTD), 2011 20th European Conference on*, pages 126–129. IEEE, 2011.

[75] Guoguang He, Manish Dev Shrimali, and Kazuyuki Aihara. Chaos control in a neural network with threshold activated coupling. In *Neural Networks, 2007. IJCNN 2007. International Joint Conference on*, pages 350–354. IEEE, 2007.

[76] Sutirth Dey and Amitabh Joshi. Stability via asynchrony in drosophila metapopulations with low migration rates. *Science*, 312(5772):434–436, 2006.

[77] H Hong and BJ Kim. H. hong, bj kim, my choi, and h. park, phys. rev. e 69, 067105 (2004). *Phys. Rev. E*, 69:067105, 2004.

[78] Zhisheng Duan, Guanrong Chen, and Lin Huang. Complex network synchronizability: Analysis and control. *Physical Review E*, 76(5):056103, 2007.

[79] Alex Bavelas. Communication patterns in task-oriented groups. *The Journal of the Acoustical Society of America*, 22(6):725–730, 1950.

[80] Pranay Deep Rungta, Chandrakala Meena, and Sudeshna Sinha. Identifying nodal properties that are crucial for the dynamical robustness of multi-stable networks. *arXiv preprint arXiv:1801.02409*, 2018.

[81] Chiranjit Mitra, Anshul Choudhary, Sudeshna Sinha, Jürgen Kurths, and Reik V Donner. Multiple-node basin stability in complex dynamical networks. *Physical Review E*, 95(3):032317, 2017.